

CARBON NANOTUBE TRANSISTORS, SENSORS, AND BEYOND

A Dissertation

Presented to the Faculty of the Graduate School
of Cornell University

In Partial Fulfillment of the Requirements for the Degree of
Doctor of Philosophy

by

Xinjian Zhou

January 2008

CARBON NANOTUBE TRANSISTORS, SENSORS, AND BEYOND

Xinjian Zhou, Ph. D.

Cornell University 2008

Carbon nanotubes are tiny hollow cylinders, made from a single graphene sheet, that possess many amazing properties. Another reason why nanotubes have generated intense research activities from scientists of various disciplines is they represent a new class of materials for the study of one-dimensional physics. In this thesis we investigate the electrical transport of semiconducting single-walled carbon nanotubes and their potential applications as biological sensors.

Electrons have been predicted, by theoretical physicists, to go through nanotubes without much resistance. But this has not been properly quantified experimentally, and the origin of the routinely observed large resistance in nanotubes is not clear. In this thesis we show that in moderate long high quality nanotubes the electrical transport is limited by electron-phonon scattering. Systematic studies are carried out using many devices of different diameters at various temperatures. The resistance and inverse of peak mobility are observed to decrease linearly with temperature, indicating the influence of phonons. The conductance and peak mobility scales with nanotube diameters also, in a linear fashion and quadratic fashion respectively. Based on electron-phonon scattering, a theory model is developed that can not only predict how the resistance changes with gate voltage but also explain the observed temperature and diameter dependence. This work clarifies the nature of electrical transport in nanotubes and sets a performance limit of nanotube devices in diffusive regime.

The electrical transport in nanotubes is extremely sensitive to local electrostatic environment due to their small size, large surface to volume ratio and high mobility, making nanotubes ideal key elements in biological sensors. In the second part of this thesis, we integrate nanotubes with supported lipid bilayers, mimic structures of cell membranes, and use this platform as a way to introduce biomolecules into the vicinity of nanotubes for sensing purpose. The quality of supported lipid bilayers near nanotubes is confirmed by probing the diffusion of lipid molecules. Nanotubes do not slow down lipid diffusions, but act as barriers for proteins bound to membrane embedded receptors. The ability of nanotubes to control membrane protein diffusions can be used to study the complex correlation between protein functions and their diffusion properties. Future efforts can be put into modulating the magnitude of nanotube barriers with electrical potentials for deterministic controls. We also demonstrate that the formation of lipid bilayers and the protein bindings on the membranes can be detected by nanotubes as their conductance are changed by those events. The sensitivity of this system can be improved to near single molecule level.

BIOGRAPHICAL SKETCH

Xinjian Zhou was born 1978 in Baoding, China. He was selected to the Chinese National Experimental Science Class in 1994 to receive intensive science education in the Affiliated High School of Peking University in Beijing. In 1997, he attended Peking University working toward a B.S. degree in physics. An undergraduate research scholar program, the Chun-Tsung scholarship, led Xinjian into the wonderful experimental research world for the first time. His diverse work ranged from developing automated laser mode measurement system to improving metal-semiconductor contacts. A summer research experience in 2000 in the group of Prof. S.T. Lee at City University of Hong Kong exposed him to a world class lab and frontier research. He continued his pursuit in physics in the United States since 2001 when he began his graduate school in the Physics Department of Cornell University. In the summer of 2002, he joined the group of Paul McEuen and has been working in nanoscience and nanotechnology ever since. After his defense in August 2007, he will continue his research as a postdoc scientist at Sandia National Laboratories in Livermore, CA.

ACKNOWLEDGEMENTS

It has been a long journey to finish my graduate school. I could have never been able to be where I am and who I am without the help of so many people.

First of all, our beloved thesis advisor, Paul McEuen, taught me so much in science and every aspect of life. My knowledge and understanding in physics was superficial when I joined your group. You showed us how to be observant and grasp the essence of any phenomenon with a simple yet clear physics picture. I am also grateful that you put extra efforts into developing our communication skills, ranging from presentations to writings. Imagine how horrible this thesis would have been without your comments and revisions. You shaped my personality as well. I learned how to deal with conflicts and difficulties in life. I can put my mind into a tranquil state, and I believe that was achieved under your subtle influence. I am so lucky to have spent my graduate student life under the guidance of an intelligent, open-minded, forgiving and loving advisor.

Thanks for all the help and company I received in the McEuen group. I want to thank our older group members for teaching me all the experimental techniques and making the lab running efficiently: Sami for showing me cleanroom processings step by step, Ji-Yong for teaching me low temperature measurements and advanced usage of AFM, Jun for your helpful discussions in physics, Ken for your broad knowledge in optics and chemistry, Ethan for telling me several nanotube growth tricks, Yuval and Alex for the setup of so many equipments for the lab, Markus for babysitting us over the years, Vera for your new MeaSureit program. Jiwoong, Shahal and Zhaohui, my discussions with you clarified my future direction. I am so glad to have consulted your expert opinions. The younger generations: Patrycja, Yaqiong, Scott, Luke, Lisa, Arend, Nathan, Sam and Jonathan, I enjoyed every minute working with you. Your diverse

and wonderful personalities made me home; and your extraordinary research gave me continuous inspirations.

Most of the projects I performed were collaborative in nature. I want to thank Prof. Carl Batt and Sonny Mark for leading me into the biology world. The DNA project with you generated the best research pictures of my graduate school. The lipid project cannot even get started without the inputs from Prof. Harold Craighead and Jose Moran-Mirabal. I felt shameless to ask for new samples every week. Your experience and knowledge in this field were indispensable to the success of this work. I also want to thank Prof. Manfred Lindau for lending me some equipments. Jie Yao, you are an underground hero. Your discussions and lectures made me close to biology.

Many thanks to the CNF staff. Thank you for teaching me the processings and keeping the facility a wonderful place. I am grateful to NBTC, who provided funding for all my research. The CNF and NBTC symposiums were always exciting.

I received a lot of helps from people outside Cornell University, and I am grateful to many people in the nanotube and nanobio community. Particularly I thank Prof. Jiu Liu and Shaoming Huang for the generous disclosure of your growth technique. Prof. Ji Ung Lee, it was a pleasure getting to know you and I enjoyed our work together in GE for the summer of 2006.

I own big favors to many people who had written all kinds of reference letters for me. Thank you for your kind words. Prof. McEuen, Craighead and Lee, your letters got me my postdoc position. Prof. Marc Bockrath and Pat Collier, thank you for supporting me in a fellowship application. Prof. Charles Lieber, Bob Austin and Yi Cui wrote letters for another important application of mine, I cannot express my thanks enough.

My life in Ithaca was made fun by many Chinese friends. I want to thank Xiaodong, Hui, Chong, Ling, Yi, Jie, Feinan, Shi, Tian, Xing and Guoqiang for being

the best roommates and long time friends. I want to thank the Chinese community in the Clark Hall basement: Lucy, Miao, Jing, Zhipan, Sufei and Yongtao, for the nice interactions between us. The people in the group of Prof. Burhman, Andrew, Nate, Phil, Ozhan, Pat, Gregg and John, have magical ways to always cheer up my wife and me.

Last, I want to thank my family. Although my parents are oceans apart from me, I know you love me and pray for me everyday. The distance in between only strengthens our connections. I am grateful to my elder brother, Xinhui, and sister-in-law, Zhihui. Thank you for taking good care of our parents. Without you, I may not have chosen to go this far. And Juting, thank you for spending the past seven years together with me, sharing the bitterness and happiness of life. Your smile is always in my mind; and making you happy is my sole motivation to achieve anything.

TABLE OF CONTENTS

Biographical sketch	iii
Acknowledgements	iv
List of figures	ix
List of tables	xii
1 Introcutio n to carbon nanotubes	1
1.1 Structure of nanotubes and characterization methods	1
1.2 Impressive properties of nanotubes and potential applications.....	7
1.3 Problems	12
1.4 Scope of this thesis	13
2 Electronic band structure of carbon nanotubes	14
2.1 Atoms, molecules and crystals	14
2.2 Tight-binding calculations of graphene band structure	15
2.3 Making nanotubes from graphene	25
2.4 Band structure of carbon nanotubes	27
2.5 Simplified band structure	32
2.6 Effects of tube curvature and non-zero overlap integral	36
3 Electron-phonon scattering in semiconducting nanotubes	40
3.1 Experimental data.....	41
3.2 Semiclassical transport, Boltzmann equation and the relaxation time approximation.....	48
3.3 Electron-Phonon scattering in nanotubes	51
3.4 A model of electron-phonon scattering limited conduction in nanotubes.....	54
3.5 Comparing data with theory	58
4 Introduction to cell membranes	60
4.1 Lipids and membrane proteins form cell membranes	61
4.2 Artificial lipid bilayers	74
5 Supported lipid bilayer/carbon nanotube hybrid	84
5.1 Prelude.....	85
5.2 Forming SLBs on nanotube chips	90
5.3 Probing SLBs near nanotubes	99
5.4 Nanotubes as barriers to protein diffusion.....	102
5.5 Electrical detection of protein binding	108

6 Conclusions	113
6.1 Summary	113
6.2 Future directions.....	114
A Nanotube growth	123
B Validation of the theory model in Chapter 3	131
C Funtionalization of nanotubes with DNA	139
D Electrode kinetics in solution	149
E Dimensionality of nanotubes and our universe	157
References	160

LIST OF FIGURES

1.1	Models of carbon allotropies.....	2
1.2	Images of nanotubes.....	2
1.3	Atomically resolved image of SWNTs.....	5
1.4	Three examples of cover figures of major scientific journals featuring nanotubes.....	8
1.5	Nanotubes as AFM scanning tips.....	11
2.1	Electron atomic and molecular orbitals.....	17
2.2	Lattice of graphene.....	18
2.3	Plots of the graphene band structure.....	22
2.4	The first Brillouin zone of graphene.....	24
2.5	Reorganization of the first Brillouin zone.....	25
2.6	Making nanotubes from graphene.....	26
2.7	The electron wave vector along the circumference of a nanotube is quantized.....	28
2.8	Extracting band structure of nanotubes from that of graphene.....	29
2.9	The subbands of a (5,5) armchair tube.....	30
2.10	The subbands of two zigzag tubes.....	32
2.11	Extracting electron energy from its wavevector around K point.....	34
2.12	Comparison of nanotube band structures calculated from the simplified dispersion relation and from the more rigorous one.....	35
2.13	Calculated bandgaps of nanotubes with different diameter and chirality when the curvature effect is taken in account.....	36
2.14	The influence of the overlap integral α on the graphene band structure.....	38
2.15	The influence of the overlap integral α on nanotube band structures.....	39
3.1	AFM image and schematic of nanotube devices.....	41
3.2	The conductance of a device at different temperatures.....	43
3.3	The conductance and mobility as functions of gate voltage for two different devices.....	44
3.4	Resistivity and peak mobility of many devices compiled.....	45
3.5	Scanned gate microscopy images of two devices.....	47
3.6	The band structure and DOS of a semiconducting nanotube.....	53
3.7	Theoretical plot of SWNT FET conductance and mobility as functions of gate voltage.....	56
4.1	Schematic of a patch of cell membrane.....	61
4.2	Structure of SDS molecule.....	62
4.3	Structure of DOPC molecule.....	63
4.4	Schematic of a micelle structure.....	64
4.5	Schematic of a bilayer vesicle structure.....	64
4.6	Membrane permeability as a function of partition coefficient times diffusion coefficient.....	68

4.7	Different types of membrane proteins.....	69
4.8	Two examples of transmembrane proteins.....	69
4.9	Schematic of a cell fusion experiment.....	71
4.10	Schematic of synapse processes that require lipid bilayer fusions.....	73
4.11	One example of suspended lipid bilayers.....	75
4.12	Side view of a patch of support lipid bilayer.....	77
4.13	Forming SLBs via vesicle fusion and rupture.....	77
4.14	Patterned SLBs using photoresist barriers.....	79
4.15	Driving charged lipid molecules in SLBs with electrical field.....	81
4.16	Schematic of polymer supported lipid bilayers.....	82
5.1	The performance of a nanotube FET in 0.1M NaCl solution.....	85
5.2	Schematic of a cell.....	89
5.3	Representation of the supported lipid bilayer/carbon nanotube hybrids.....	92
5.4	SLBs formed on dirty and clean surfaces.....	92
5.5	Estimation of lipid diffusion coefficient using FRAP.....	95
5.6	FCS measurement of lipid diffusion coefficient.....	98
5.7	Test of lipid diffusion near SWNTs.....	100
5.8	The fluorescence intensity distribution around SWNTs and AFM images of the same regions.....	101
5.9	Driving ganglioside-bound toxins near SWNTs with water flow.....	104
5.10	A more complicated model of cell membrane.....	107
5.11	Detection of biotin-streptavidin binding with SWNT FETs.....	110
5.12	Detection of DOPC SLB formation with SWNT FETs.....	111
6.1	Schematic of a proposed structure to use nanotube as cross-membrane potential sensor.....	118
6.2	A proposed experimental geometry to put suspended nanotubes into cells.....	121
A.1	Two long (~100 μm) nanotubes grown with the Duke recipe in our group...	126
A.2	Long and highly aligned nanotubes grown on quartz substrates.....	126
A.3	A dense mesh of nanotubes grown in a region defined by parylene.....	128
A.4	Nanotube mesh grown without water vapor in the CVD chamber.....	129
A.5	Aligned nanotube forest grown with water vapor in the CVD chamber.....	129
B.1	Calculated resistivity as a function of temperature for three nanotubes with different chiralities.....	134
B.2	Theory predicted conductance through 1 and 3 subbands.....	137
C.1	Functionalization of nanotubes with PASE.....	141
C.2	AFM images taken before and after attaching glucose oxidase onto nanotubes.....	141
C.3	Schematic of PCR cycles.....	144
C.4	AFM images of DNAs attached onto nanotubes.....	146
C.5	Topography (left) and phase (right) image of a nanotube/DNA complex.....	147

D.1	Helmholtz model of double layers.....	151
D.2	The potential distribution outside an electrode according to the Debye-Huckel theory	153
D.3	The capacitance per unit area according to different models.	154

LIST OF TABLES

5.1	Summary of normalized permeabilities of nanotube barriers.....	106
-----	--	-----

CHAPTER 1

INTRODUCTION TO CARBON NANOTUBES

Carbon is a really versatile element, for reasons rooted from its four valence electrons and the right atomic size. It can form numerous compounds, many of which are the basis of life on this planet. Even pure carbon can have quite a few allotropes. This is because the four valence electrons can make different types of bonds with other carbon atoms. Diamond and graphite (upper left and right in Fig. 1.1) have distinct optical, electrical and monetary properties, all just because the carbon atoms arrange themselves in different ways. It was not until about 20 years ago before people gained the ability to probe structure of nanometer scales and more interesting forms of carbon were discovered. The zero dimensional C₆₀ buckyball (lower left in Fig. 1.1) was discovered in spectroscopy data in 1985 (Kroto et al. 1985), followed by one dimensional nanotube (lower right in Fig. 1.1) in 1991 (Iijima 1991). These newly-found carbon structures couple quantum effects, lower dimensionality and the unique properties of graphene (single layer of graphite) (Novoselov et al. 2004; Geim and Novoselov 2007) all together, and they have generated intense research in many disciplines because they bridge between Physics, Chemistry, Material Science and more. This thesis is devoted to the study of nanotubes. In this chapter, a broad introduction is given on the interesting properties of nanotubes and the current status of this field.

1.1 Structure of nanotubes and characterization methods

The structure of nanotubes originates from that of graphite. In graphite, carbon atoms sit in hexagonal patterns and form flat two dimensional sheets. Single-walled nanotubes (SWNTs) can be viewed as seamless cylinders rolled up from a piece of

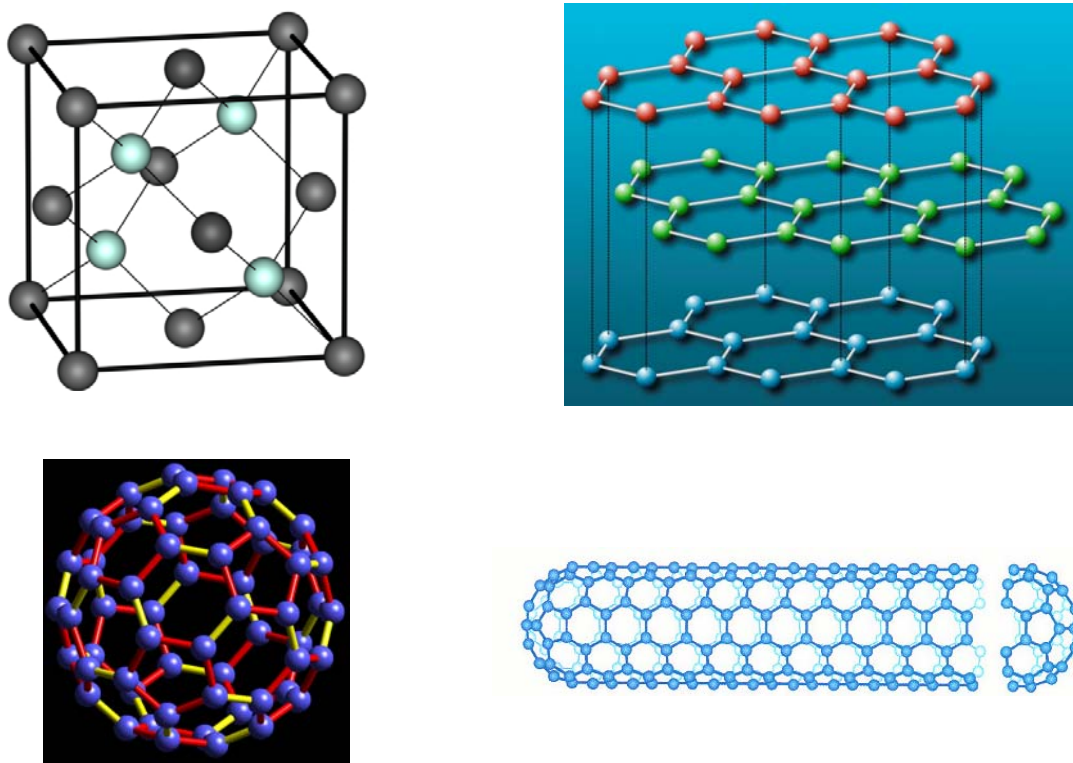


Figure 1.1: Models of carbon allotropies. Clockwise from top left: diamond, graphite (scifun.ed.ac.uk), nanotube, C60 buckyball (staff.science.uva.nl).

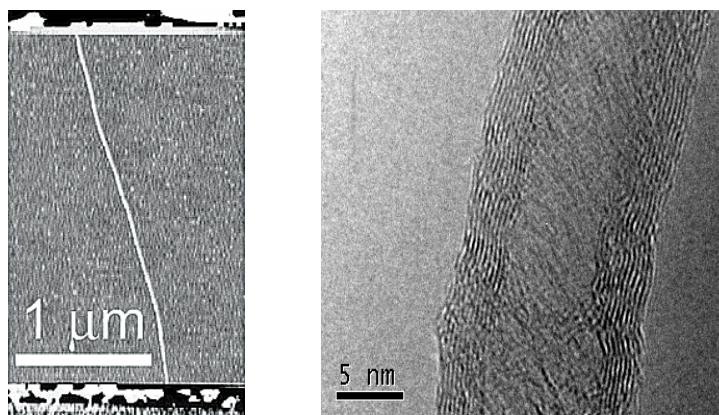


Figure 1.2: Images of nanotubes. **Left**, an atomic force microscope image of a single-walled nanotube. **Right**, a TEM image of a multi-walled nanotube.

graphene. Another type of nanotube is called multi-walled. They are concentric cylinders of multiple layers of graphene.

A transmission electron microscope (TEM) image of a multi-walled nanotube (MWNT) is shown on the right side of Fig. 1.2. Multi-walled nanotubes are typically larger than SWNTs. The observed properties are interplays of multiple layers and harder to understand. MWNTs are typically more defective. Therefore, our lab focuses on the study of SWNTs. All the experiments in this thesis are carried out with SWNTs or nanotubes with a couple of walls.

Although the typical diameter of SWNTs is a couple of nanometers, there are plenty of ways to characterize them with modern tools such as the atomic force microscope (AFM), scanning electron microscope (SEM), TEM and scanning tunneling microscope (STM). Various optical spectroscopy techniques can be used as powerful tools to extract information as well.

There are a few ways to grow SWNTs, either as a chemical reaction (chemical vapor deposition) or a physical process (arc discharge and laser ablation). The growth process is hard to control due to one fact: there are an infinite number ways to form a SWNT. As a quantum system can be fully described by a set of quantum numbers, an individual nanotube can be uniquely identified with three quantities: nanotube diameter, chirality and number of walls. The meaning of these words will be explained in the rest of this section, along with methods to measure them. However, an underlying assumption of the above statement is that nanotubes are perfect. In reality defects should also be taken into consideration and will be discussed too.

Diameter

A typical AFM image of SWNTs is shown on the left side of Fig. 1.2. One should not be fooled by the width of nanotubes in AFM or SEM images. The convolution of

nanotubes and the probing AFM tip or electron beams makes the lateral dimension much larger than the nanotube diameter. AFM probes tube diameters by measuring how far the AFM tip lifts up from the substrate surface when it is on top of nanotubes. It is crucial to do it at small scanning range ($\sim\mu\text{m}$). Otherwise the diameter value will be underestimated. TEM can measure tube diameters too, but it is limited to suspended nanotubes.

Raman spectroscopy is another tool to measure small SWNTs. The radial breathing mode (RBM) phonons, where all carbon atoms oscillate radially with the same phase, generate a strong peak in Raman spectroscopy at around 200 cm^{-1} . The peak position is inversely proportional to tube diameters: $\omega = 248\text{ cm}^{-1}/d\text{ [nm]}$. The RBM peak of large diameter tubes falls below the cut off frequency of typical instruments. The magnitude of Raman peak can be enhanced significantly when the excitation is in resonance with the nanotubes sample. As will be shown in Chapter 2, the density of states in nanotubes has many peaks called Van Hove singularities. When the energy of Raman excitation light matches the energy difference between certain peaks, the absorptions is enhanced, and so is the Raman peak.

Chirality

Chirality describes how the atoms in nanotubes arrange them along the circumference (detailed discussion in Section 2.3). Chirality is more difficult to probe because it comes from atomic scale details. STM has been shown to be able to resolve the arrangement of carbon in SWNTs (Odom et al. 1998; Wildoer et al. 1998). But this is time-consuming to do and requires conductive substrates.

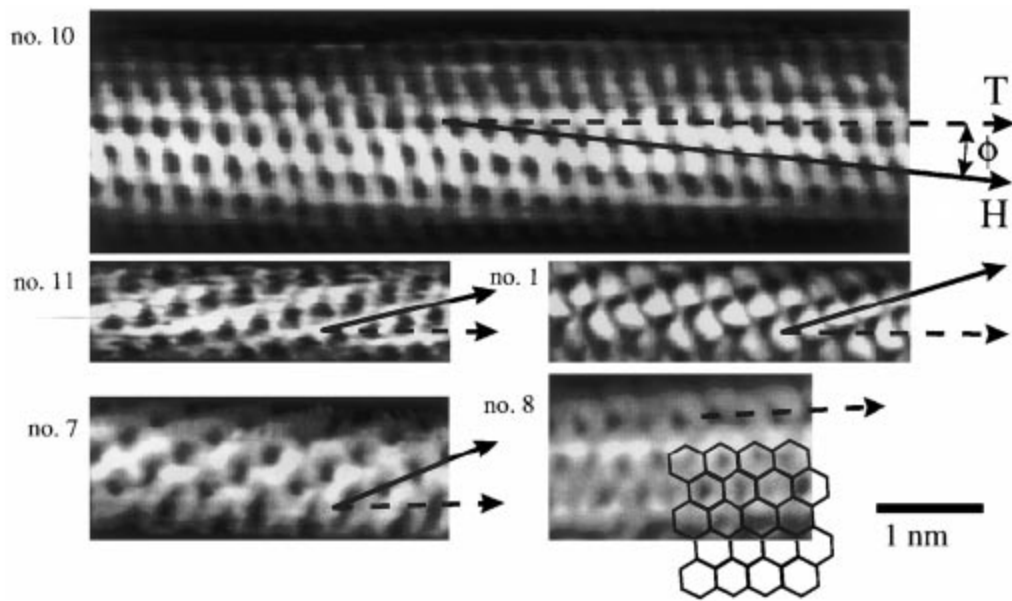


Figure 1.3: Atomically resolved image of SWNTs (Wildoer et al. 1998).

Another possibility is to use Raman spectroscopy (Dresselhaus et al. 2002). When the diameter of a nanotube is small, a precise measurement of diameter can reveal its chirality since there is one-to-one correspondence between these two quantities. The RBM peak positions in Raman, as well as the photon energy when resonance Raman happens, can be used as the most accurate way to measure tube diameter, and thus chirality. Other features in Raman, D-band and G-band, are chirality dependent and can be used as corroboration of chirality assignment (Dresselhaus et al. 2002). Fluorescence microscopy has also been used to assign absorption/emission peaks to species of semiconducting SWNTs (Bachilo et al. 2002), but this assignment is challenged by others due to the influence of strong exciton effects in SWNTs (Wang et al. 2005). All these characterizations are not very easy to carry out and the results are often inconclusive; fortunately many properties of SWNTs depend primarily only on diameter.

Number of walls

It is important to distinguish SWNTs from MWNTs. This can be done most easily with TEM. When nanotubes are integrated into devices like field effect transistors (FETs), however, they are typically sitting on insulating substrates, making TEM unfeasible. Since nanotubes are contacted by two electrodes in this case, the best way to see number of walls is to apply a high bias and see the value of saturation currents. When the current is around $25 \mu\text{A}$, this is only one wall (Zhen et al. 2000). This is a result of how electron transports are limited by electron-optical phonon scattering at high electrical field. The $25 \mu\text{A}$ value comes from the optical phonon energy ($\sim 160 \text{ meV}$) in nanotubes and the universal conductance quantum of one-dimensional channels (e^2/h).

Defects

Defects in SWNTs can be visualized with STM due to its high resolving power (Ouyang et al. 2002). However it is easier to measure defects using Raman spectroscopy (Doorn et al. 2005). There are two ways to do so. First, the D-band, typical around 1340 cm^{-1} in Raman spectroscopy, appears when there are 5 carbon rings, one kind of defect, present (Saito et al. 1998). Second, when a 5-carbon ring defect occurs in a SWNT, the diameters on two sides of this defect are not exactly the same. A shift in the RBM peak position should happen if the measurement is precise enough. Most important, this defect may lead to a change in the electronic band structure on the SWNT on two sides of the defect to strongly modify the magnitude of the RBM peak, as has been observed by a group at Los Alamos National Lab (Doorn et al. 2005).

When nanotubes are integrated into FETs, one way to probe defects is to see the Coulomb oscillation at low temperature to acquire the size of the quantum dot and compare that to the length of the nanotube between source-drain electrodes (Woodside and McEuen 2002). Another method requires the use of AFM. A voltage applied to a conductive AFM tip can be used to locally modulate the Fermi level in a nanotube, and

the response in the nanotube conductance is directly related to its defects (Bachtold et al. 2000) at the location of the AFM tip. This method is used in Chapter 3 to address a puzzle on nanotube mobilities. The observed defects with these two methods could come from irregularities in the substrates, where the nanotubes are sitting on, other than from the tubes themselves.

As mentioned before, SWNTs can be fabricated with different techniques. It has been shown that chemical vapor deposition (CVD) gives best quality tubes. The Los Alamos group (Doorn et al. 2005) saw only one major defect in twenty 500 μ m long SWNTs when Raman was taken along the tubes. As a comparison, STM study of laser oven grown nanotubes showed much higher frequency of finding such defects (Ouyang et al. 2001; Kim et al. 2003). In this thesis, all SWNTs are grown using CVD technique due to this reason. A discussion on growth techniques is included in Appendix I.

1.2 Impressive properties of nanotubes and potential applications

SWNTs have many other magnificent properties that have lured researchers of many disciplines into intensive studies. Figure 1.4 gives three cover images of major scientific journals, all of which feature nanotubes. The impressive properties in three aspects, mechanical, electrical and biological, along with potential applications will be presented in this section. Besides them, the small size of nanotubes also leads to many unique advantages that will also be discussed.

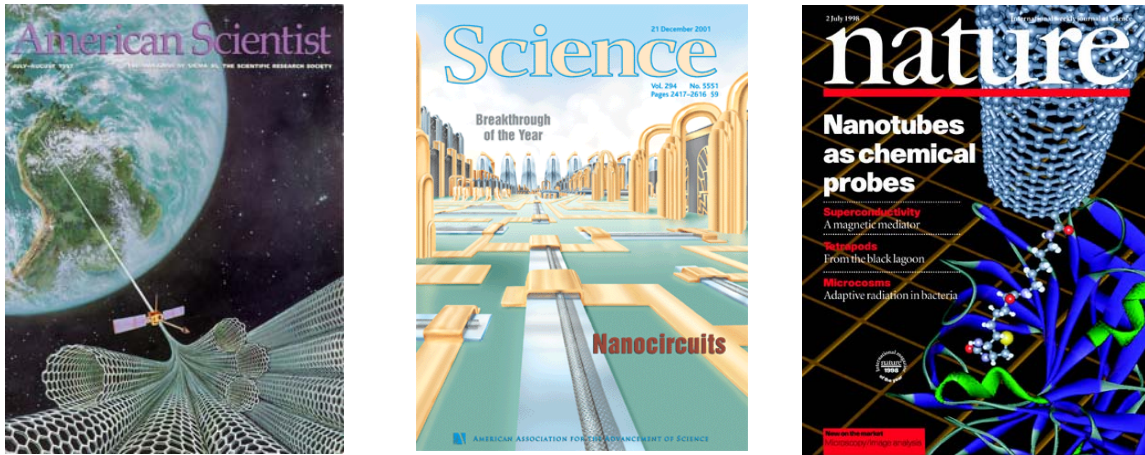


Figure 1.4: Three examples of cover figures of major scientific journals featuring nanotubes.

Mechanical

SWNTs are strong and stiff. The Young's modulus of nanotubes, $\sim 1\text{TPa}$, is five times higher than that of steel (Treacy et al. 1996). Their theoretically predicted tensile strength, the maximum tensile stress one material can sustain before failure, is 130GPa (Yakobson 1998). A group measured this parameter of MWNTs and the largest observed value is about 63GPa (Yu et al. 2000). As a comparison, the tensile strength of steel is less than 1GPa . At the same time, SWNTs are extremely light. There was even a proposal to build a space elevator using SWNT ribbons (Edwards 2000) as shown in the left image in Fig. 1.4. There are huge fundamental and practical challenges standing in the way of this project. However, one day it is possible to replace the cables on the Golden Gate Bridge with nanotube cables.

These mechanical properties, coupled with electrical conductivity, also inspired people to integrate SWNTs into nanoelectromechanical systems. For example, an electrically actuated tunable oscillator using SWNTs has been demonstrated (Sazonova et al. 2004). A company is working toward commercializing large density and high speed

random access memories based on suspended nanotubes that can be modulated by external voltages to switch between two states (Nantero.com).

Electrical

SWNTs are interesting electrical materials. Their amazing properties come from two origins: material and size. SWNTs are made of graphene. Graphene has high intrinsic electron mobility (Geim and Novoselov 2007) due to its lack of lattice defects as compared to most other semiconductor materials and its unique linear dispersion relation that will be presented in Chapter 2. The diameters of SWNTs are so small that the electron wave vectors along the circumferences are quantized. This produces a series of subbands in a nanotube. It also makes SWNTs either metallic or semiconducting depending on their chirality (detailed discussion in Chapter 2).

SWNTs have remarkable electrical performances. High quality SWNTs can have mobility larger than $10,000 \text{ cm}^2\text{V}^{-1}\text{S}^{-1}$ and mean free path longer than $1 \mu\text{m}$. Besides extraordinary conductance, these tiny SWNTs, when made into FETs, can have minimum capacitance coupling with gates. These two factors lead to small RC time constant. People have demonstrated SWNT FETs operating at up to 50GHz (Rosenblatt et al. 2005). One day when people had mastered the assembly technique to put desired SWNTs species ideally at the places they should be as the middle image in Fig. 1.4 shows, we could have computer chips running at fast speed while consuming less power.

The unique band structure and one dimensionality also make carbon nanotubes a unique optoelectronic material. The electron density of states in nanotubes has a series of singularities, associated with the onsets of subbands. Effectively nanotubes can be viewed as semiconductors with multiple bandgaps and can efficiently absorb lights of a wide spectrum (Stewart and Leonard 2004; Ji Ung 2007). Contrary to chemical dopings in traditional semiconductor devices, the doping level of nanotubes can be modulated

electrostatically with high spatial resolution to generate electrons and holes at different regions. Electroluminescence in nanotubes can be realized with untraditional methods (Misewich et al. 2003). Research efforts in these areas are booming.

Chemical/Biological

SWNTs are chemically inert, especially when no defects are present. This makes them chemically stable and biologically compatible. Studies have shown that SWNT FETs can operate in aqueous solutions (Kruger et al. 2001; Rosenblatt et al. 2002). Again because of their molecular-scale size and extreme sensitivity to environments, SWNTs are ideal materials to make detectors that are capable to reach single-molecule level sensitivity (Besteman et al. 2003; Bradley et al. 2005). A nanotube/lipid bilayer hybrid structure will be presented in Chapter 4 and 5.

Potential applications are not limited to sensors. On top of being chemically stable, SWNTs have large surface to volume ratio and are becoming an interesting material as electrodes in electrochemistry researches. SWNTs can be used as electrodes (Heller et al. 2006) or nucleate sites for nanoparticle growth (Quinn et al. 2005). The high surface area SWNTs are being researched as hydrogen storage candidates (Dillon et al. 1997). On the biology side, SWNTs have been used as drug delivery vehicles to bring chemicals into cells (Liu et al. 2007). However there are issues concerning the toxicity of SWNTs, but it is more than likely that these concerns will turn out unnecessary as a study recently showed that injected SWNTs can be excreted out the bodies of mice within a couple months (Liu et al. 2007), during which time no toxic effects were observed.

Small

Another big advantage of SWNTs is their small diameter. For example, the lateral resolution of AFM is limited by the size of scanning tip. Ever since the discovery of

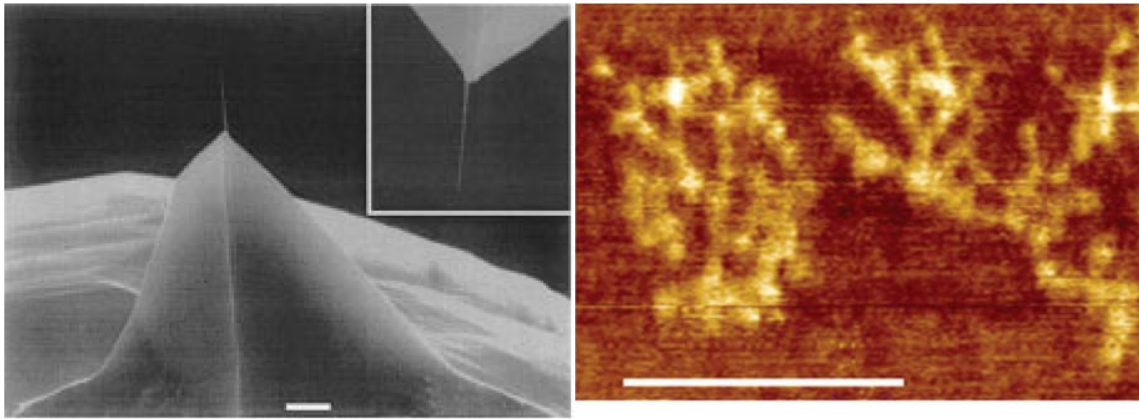


Figure 1.5: **Left**, SEM image of a MWNT attached to a conventional AFM cantilever tip (Wong et al. 1998). Scale bar is 1 μm . **Right**, AFM image of dendrimer-like DNAs taken with SWNT tip (Li et al. 2004). Scale bar is 100 nm.

SWNTs, people have been trying to attach them onto normal AFM tips and use them to interact with sample in order to improve resolving capability. Examples are shown in Fig. 1.5.

One can even chemically modify the end of nanotube tips with functional group to do chemical force microscope (Wong et al. 1998). The small size of SWNTs makes it easier to study chemical bindings between only one pair of receptor/target.

Another application utilizing the small size of SWNTs is electron emitters. Because of the tiny cross sections of SWNTs, the electrical field around the tip can reach very high value when a potential is applied between SWNTs and the ground. This high field facilitates electrons to tunnel out. This kind of emitters can be used to extract electrons to generate light, either visible (TV) or X-ray (portable and high resolution X-ray machine) (Liu et al. 2006).

These examples are only a small subset of potential applications due to the small sizes of SWNTs.

1.3 Problems

Even with the hot pursuit of thousands of researchers around the globe, currently SWNTs are not in any high-tech products. The major problems right now are SWNT growth and manipulation.

As will be explained in Chapter 2 and 3, there are infinite number species of SWNTs. Some of them are dramatically different than others. Up to today, no technique can grow single species of SWNTs on demand, namely, with controlled chirality and diameter. Progress has been made in separating different SWNT species in solutions (Arnold et al. 2006) although the processing may induce defects on nanotubes. Sometimes long nanotubes in large quantities are valuable to industrial applications. Recently more efficient growth (Hata et al. 2004) brought us hope along that direction.

Another more difficult problem is assembly. It is not easy to manipulate billions of individual nanotubes, especially when one wants them to behave against thermodynamics. For example, how could one put billions of nanotubes to the exact targeted locations as illustrated in the middle image in Fig. 1.4. Direct growth from individual spot is very hard because the growth is not deterministic in terms of yield, orientation, length, chirality and diameter. Other approaches use solution assembly by either functionalizing the substrate selectively (Keren et al. 2003) or by electrical manipulation using dielectrophoresis (Vijayaraghavan et al. 2007). The ultimate goal is to grow SWNT computer chips out of a beaker by directing molecular scale self-assembly.

There is still a long way to achieve applications that fully utilize the wonderful properties of SWNTs. From an optimistic point of view, that means there are huge opportunities before us.

1.4 Scope of this thesis

This chapter gives a brief, but hopefully broad, introduction on many aspects of SWNTs. The main content of this thesis focuses on two separate issues. The first half, Chapter 2 and 3, discusses electron transport in SWNTs. Chapter 2 calculates the band structure of graphene and nanotubes. Chapter 3 presents experimental data and a theory model on electron transport in the regime where there are frequent electron scattering from lattice vibrations. It helps us understand the intrinsic electrical properties of SWNTs as one-dimensional conductors. This work clarified several misconceptions in this field, provided a simple theory to explain the observed conductance and mobility data, and discovered scaling laws in the electrical properties of SWNTs.

The second half, Chapter 4 and 5, probes the possibilities of integrating SWNTs with cell membranes and monitoring biological activities using this structure. Chapter 4 gives an introduction to many physical properties of cell membranes. It also discusses artificial membrane mimics and why they are useful in studying cell membranes. Chapter 5 focuses on one project that utilized the small size of SWNTs, their high sensitivity to local electrostatic environment and their compatibility with aqueous solutions. SWNTs were put underneath a patch of lipid bilayer. The quality and continuity of the bilayer over the SWNTs were probed and proved to be good. SWNTs interact with membrane-bound proteins and slow down their diffusion. It was also demonstrated that SWNT FETs are able to sense protein binding events on the membrane surfaces.

CHAPTER 2

ELECTRONIC BAND STRUCTURE OF CARBON NANOTUBES

In this chapter, the electronic band structure of graphene will be calculated with tight-binding methods (or Linear Combination of Atomic Orbitals (LCAO) as called in many chemistry books) (Ashcroft and Mermin 1976). The dispersion relation of nanotubes will be derived based on this result. The unique dispersion relation generates profound influence on the nanotube electrical and transport properties, which will be discussed in Chapter 3.

Tight binding calculation of nanotube band structure can be found in many sources (e.g. graphene by P. Wallace (Wallace 1947), nanotube by R. Saito (Saito et al. 1992) and E. Minot (Minot, 2004)). The purposes of this chapter will be to summarize and simplify these results, as well as comment on some frequently-asked questions.

2.1 Atoms, molecules and crystals

The first question that many students ask when they are exposed to solid state physics for the first time may well be: what is the origin of energy bands in crystals? It is quite obvious that a free electron has a continuous energy spectrum while electrons in isolated atoms are confined to quantized energy levels. Electrons in crystals are in an intermediate state between free and confined electrons. They are delocalized to reach out to the whole crystal, similar to free electrons, but they feel the periodic potentials of the ions at the same time. This dualism gives rise to energy bands. The crystals referred in this chapter are covalently-bonded solids (Ashcroft and Mermin 1976), as in the cases of graphene and nanotubes.

The delocalization of electrons in crystalline solids is a direct consequence of the nature of covalent bonds, which are characterized by sharing electron pairs between atoms. This sharing can happen because the distance between two bonding atoms are comparable to the range of certain atomic orbitals. When two atoms form a molecule via covalent bonding, the higher energy valence electrons can explore the whole molecule because they spend time in all parts of each atom. In a covalent crystal, when a valence electron of atom A moves to its nearest neighbor atom B, it can come back to atom A or move further to other neighbors of atom B. This is how valence electrons can reach the whole crystal, or in other words, become delocalized.

Similar to free electrons, delocalized electrons spread over real space and can have different modes, or wave vectors. The allowed states are set by boundary conditions. As the length scale of a crystal becomes very large, the energy difference between large numbers of states vanishes. Therefore, as contrary to atoms having discrete energy levels, solids have energy bands. They can be viewed, to the zero order approximation, as atomic energy levels broadened by delocalization.

Although delocalized, the electrons in solids are not free. The configurations of atoms in crystals determine their band structures. The unique properties of various crystals are due to the fact that the electron energy does not grow quadratically with wave vector, as in the case of free electrons. This gives different solids their special flavors.

2.2 Tight-binding calculations of graphene band structure

In this section, the band structure of graphene will be calculated with tight-binding method. The calculation, as well as the discussion in the previous section, is valid only in the regime where the overlap of atomic orbitals (wave functions) is significant but not too large. This condition ensures atomic orbital description stays relevant.

Due to the periodicity in crystals and their large size compared to atomic scales, the electron wave functions satisfy Bloch theorem, and can be generally written in the form of Eq. 2.1. The function ϕ is called Wannier function.

$$\psi(\mathbf{r}) = \sum_{\mathbf{R}} e^{i\mathbf{k}\cdot\mathbf{R}} \phi(\mathbf{r} - \mathbf{R}) \quad (2.1)$$

In other words, a Bloch function is nothing but a summation of wave functions, which are the same at each unit cell, multiplied by interference phase factors.

The essence of tight-binding methods is that the Wannier function can be approximated by a linear combination of atomic orbitals. This applies only when the overlap is not too large to distort the Wannier function to an extent that it does not resemble atomic orbitals any more. Mathematically, the essence of tight binding method is written in Eq. 2.2:

$$\phi(\mathbf{r}) = \sum_n b_n \varphi_n(\mathbf{r}), \quad (2.2)$$

where $\varphi_n(\mathbf{r})$ are the atomic wave functions.

Figure 2.1 shows the typical atomic orbitals of electrons with different angular momentum (1s, 2p, 3d, 4f). When two identical atoms form a molecule via overlapping one of their p orbitals, e.g. p_z orbital, the resulting wave function is called Pi orbital, denoted by Π_{p-p} and shown in Fig. 2.1. It almost looks like the simple addition of two p_z orbitals sitting next to each other. This is the essential bonding that leads to the Π_{p-p} coupling in graphene and carbon nanotubes. Except in the latter cases, billions of carbon atoms form a gigantic Π_{p-p} bond and electrons are free to move through the whole crystal.

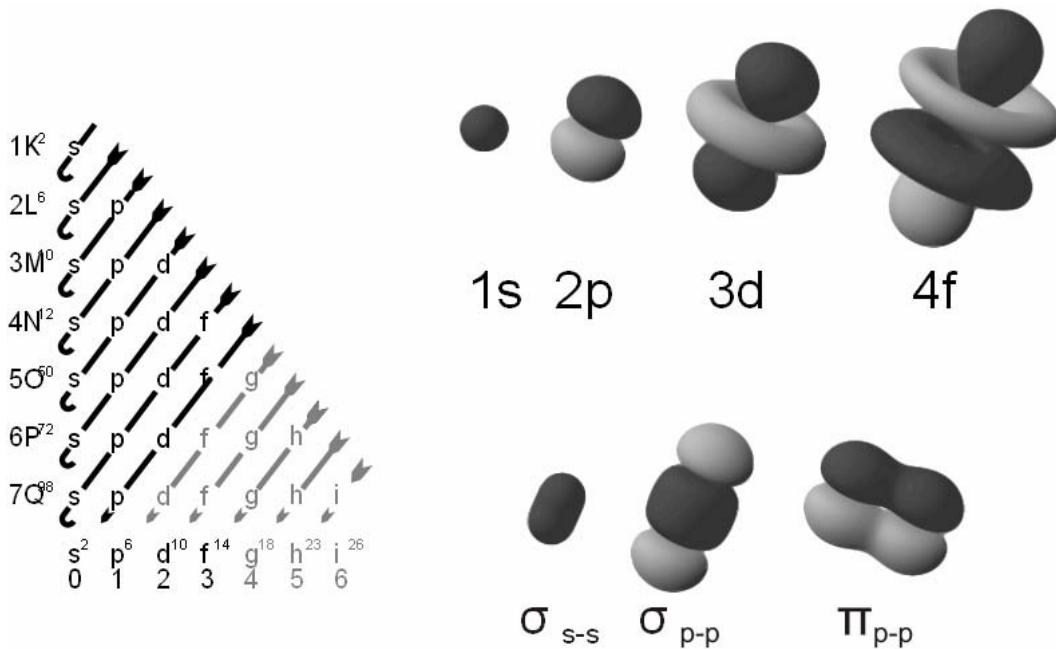


Figure 2.1: Electron atomic and molecular orbitals (Wikipedia). **Left**, the electron orbital filling scheme. Carbon atoms have 4 valence electrons, one of which is in 2s state and the other three are in 2p states. **Right**, the shapes of s,p,d,f orbitals. A π bond, formed by two parallel p orbitals, is shown at the bottom right corner.

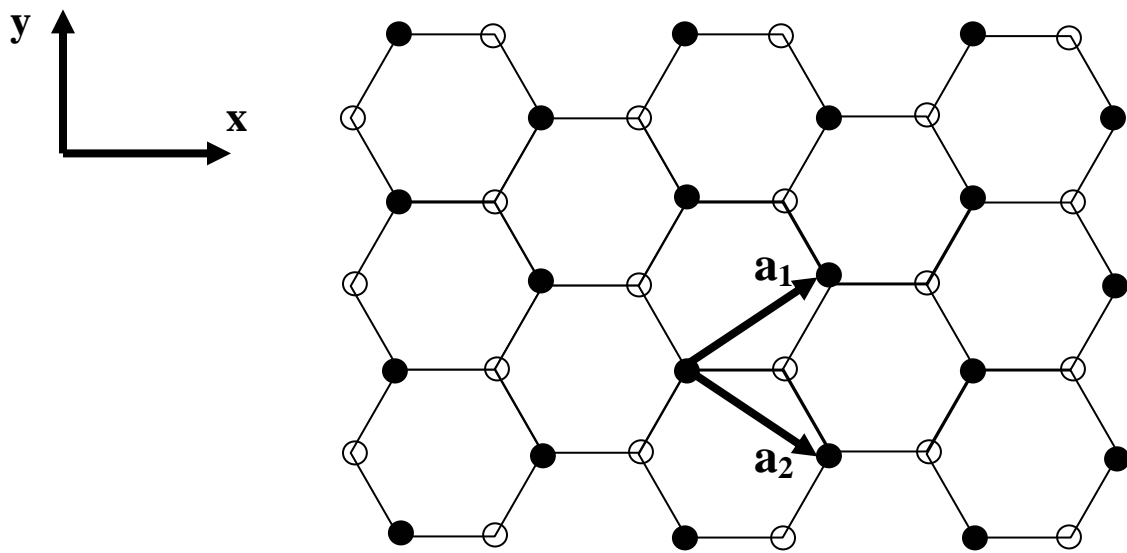


Figure 2.2: Lattice of graphene. The length of the carbon-carbon bonds is 1.42\AA . A pair of adjacent carbon atoms, denoted with solid dot and open dot respectively, forms a unit cell.

Figure 2.2 shows the hexagon lattice of graphene. However this is not a Bravais lattice because there are no two primitive vectors that can construct position vectors \mathbf{R} to reach every carbon atom in the lattice. Another way to look at it is that the view from atoms denoted with solid dots is different than that from atoms denoted with open dots. The views are mirror images of each other.

The correct Bravais lattice to describe graphene is a triangular lattice with two-atom unit cells. The primitive vectors of this triangular lattice are defined as

$$\begin{aligned} \mathbf{a}_1 &= \frac{\sqrt{3}}{2} a \hat{\mathbf{x}} + \frac{1}{2} a \hat{\mathbf{y}} \\ \mathbf{a}_2 &= \frac{\sqrt{3}}{2} a \hat{\mathbf{x}} - \frac{1}{2} a \hat{\mathbf{y}} \end{aligned} \quad , \quad (2.3)$$

where $a = \sqrt{3}a_{cc} = 2.46\text{\AA}$. a_{cc} is the length of carbon-carbon bonds in graphene, and equals roughly 1.42\AA .

The tight binding calculation is a little complicated due to the dual-atom basis. The atomic orbitals of the two carbon atoms (one solid dot and one adjacent open dot in Fig. 2.2), φ_1 and φ_2 , have to be taken into consideration. The total function is a linear combination of φ_1 and φ_2 :

$$\phi(\mathbf{r}) = b_1\varphi_1(\mathbf{r}) + b_2\varphi_2(\mathbf{r}) = \sum_n b_n \varphi_n(\mathbf{r}) \quad (2.4)$$

In some sense this is a simple calculation because only one atomic orbital p_z , as the one shown in Fig 2.1, is used. The chemical bonds between carbon atoms, the ones that dominantly determine the lattice constant a , involves three orbitals: s , p_x and p_y . These three orbitals are mixed up to form three equivalent bonds through so-called sp_2 hybridization. The electrons in these sp_2 bonds are tightly confined near nuclei and can be neglected in this calculation.

The Hamiltonian is

$$H = \frac{\mathbf{p}^2}{2m} + \sum_{\mathbf{R}} V_{1,2}(\mathbf{r} - \mathbf{R}). \quad (2.5)$$

The potential term is the summation all of potentials due to every atom in the lattice.

Since φ_1 and φ_2 are atomic orbitals, they satisfy

$$\left(\frac{\mathbf{p}^2}{2m} + V_{1,2}(\mathbf{r}) \right) \varphi_{1,2} = \varepsilon_{1,2} \varphi_{1,2}. \quad (2.6)$$

ε_1 and ε_2 are apparently equal because the two atoms in one unit cell are equivalent.

When the Hamiltonian in Eq. 2.5 is applied to φ_1 ,

$$H\varphi_1 = \varepsilon_1\varphi_1 + \left(\sum_{\mathbf{R}} V_{1,2}(\mathbf{r} - \mathbf{R}) - V_1(\mathbf{r}) \right) \varphi_1 \quad (2.7)$$

Now the potential terms sum all atoms except the one at $\mathbf{R} = 0$. It can be denoted as ΔV_1 , for simplicity, and $\varepsilon_{1,2}$ can be set at zero. Then Eq. 2.7 is simplified as

$$H\varphi_{1,2} = \Delta V_{1,2}\varphi_{1,2}. \quad (2.8)$$

To get the energy eigenvalues of the Schrödinger equation

$$H\psi_{\mathbf{k}} = E(\mathbf{k})\psi_{\mathbf{k}}, \quad (2.9)$$

$\psi_{\mathbf{k}}$ can be projected onto φ_1 and φ_2 .

$$E(\mathbf{k})\langle \varphi_n | \psi_{\mathbf{k}} \rangle = \langle \varphi_n | \Delta V_n | \psi_{\mathbf{k}} \rangle. \quad (2.10)$$

When $\langle \varphi_n | \psi_{\mathbf{k}} \rangle$ is calculated, only the overlaps between the nearest neighbors are considered as non-zero. In other words, the wave function is assumed to extend to one atom away, but not two. The same rule holds for $\langle \varphi_n | \Delta V_n | \psi_{\mathbf{k}} \rangle$ term, only the on-site and nearest neighbors integral are included. From Fig. 2.2, it can be seen that each carbon atom has three nearest neighbors. Define α as the overlap integral and γ as the transfer integral,

$$\alpha = \int \varphi_1^* \varphi_2 \quad (2.11)$$

$$\gamma = \int \varphi_1^* \Delta V_1 \varphi_2 = \int \varphi_2^* \Delta V_2 \varphi_1, \quad (2.12)$$

Equation 2.10 can be simplified as

$$E(\mathbf{k})(b_1 + b_2\alpha\xi(\mathbf{k})) = b_2\gamma\xi(\mathbf{k}) \quad (2.13)$$

$$E(\mathbf{k})(b_2 + b_1\alpha\xi(\mathbf{k})^*) = b_1\gamma\xi(\mathbf{k})^*, \quad (2.14)$$

where $\xi(\mathbf{k})$ is an interference factor

$$\xi(\mathbf{k}) = 1 + \exp(-i\mathbf{k} \cdot \mathbf{a}_1) + \exp(-i\mathbf{k} \cdot \mathbf{a}_2). \quad (2.15)$$

It's determined by the geometry of the lattice, and is a function of electron wave vectors. Please note the relative phase is given by the locations of the neighboring unit cells, not the locations of neighboring carbon atoms. This can be seen from Eq. 2.1. Each carbon atom has three nearest neighboring atoms as shown in Fig. 2.2. One is sitting in the same unit cell and the other two are sitting in two out of the six neighboring unit cells at $-\mathbf{a}_1$ and $-\mathbf{a}_2$.

$E(\mathbf{k})$ can be extracted by solving Eqs. 2.13 and 2.14:

$$\begin{pmatrix} E(\mathbf{k}) & \xi(\mathbf{k})(\alpha E(\mathbf{k}) - \gamma) \\ \xi(\mathbf{k})^*(\alpha E(\mathbf{k}) - \gamma) & E(\mathbf{k}) \end{pmatrix} \begin{pmatrix} b_1 \\ b_2 \end{pmatrix} = 0. \quad (2.16)$$

The solutions are

$$E(\mathbf{k}) = \frac{\pm \gamma |\xi(\mathbf{k})|}{1 \pm \alpha |\xi(\mathbf{k})|}. \quad (2.17)$$

In most literatures, α is considered much smaller than unity (the validity of this approximation will be discussed in Section 2.6). Therefore Eq. 2.17 is simplified as

$$E(\mathbf{k}) = \pm \gamma |\xi(\mathbf{k})| = \pm \gamma \sqrt{1 + 4 \cos\left(\frac{\sqrt{3}ak_y}{2}\right) \cos\left(\frac{ak_x}{2}\right) + 4 \cos^2\left(\frac{ak_x}{2}\right)} \quad (2.18)$$

Please note a is the lattice constant, i.e. $a = \sqrt{3}a_{cc}$. The x,y coordinates are defined in Fig 2.2.

The band structure in Eq. 2.18 is given by two parts. $\xi(\mathbf{k})$ is determined by the symmetry of the lattice while γ is determined by the strength of the overlapping between adjacent atomic orbitals and the lattice potential. Since the adjacent atoms have the same

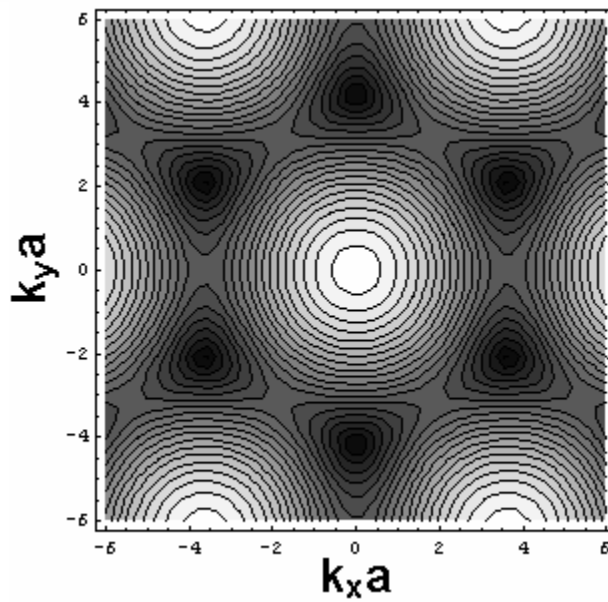
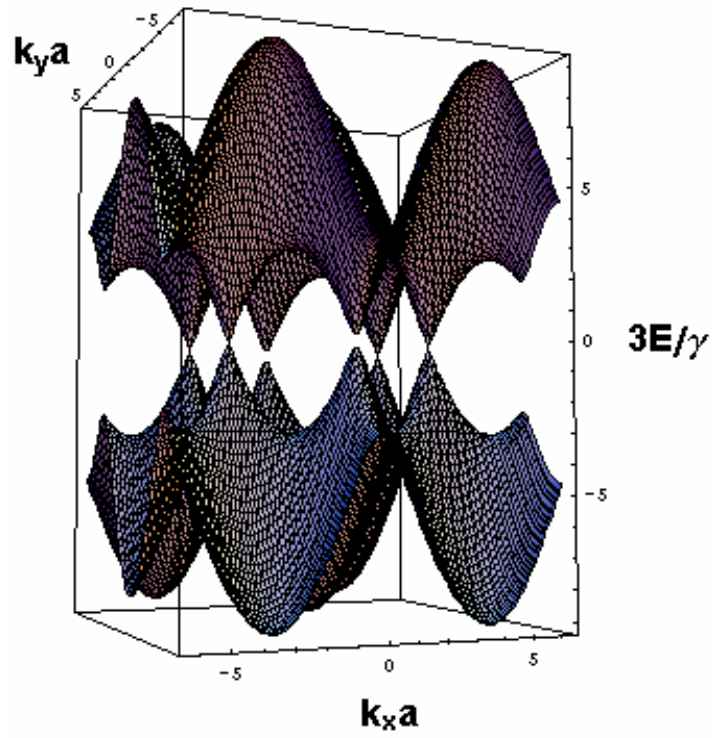


Figure 2.3: Plots of the graphene band structure. **Top**, 3D plot of both binding and anti-binding bands. **Bottom**, contour plot of one band.

electron affinity, graphene is a perfect example of covalent lattice. γ would be small if electrons resided most of the time on one type of atoms in the lattice. The extreme case would be ionic crystal. It will be proven later that larger γ means electrons can travel faster in the solid.

Figure 2.3 shows the band structure of graphene. From the 3D plot on the left, it is obvious that there are two bands, one with lower energy and one with higher energy. These are so-called bonding and anti-bonding orbitals. The origin of the names is clear once we plug the eigenvalues back to Eq. 2.16. With the low energy eigenvalue, $E(\mathbf{k}) = -|\gamma| \cdot |\xi(\mathbf{k})| / (1 + \alpha|\xi(\mathbf{k})|)$ (γ is negative!), $b_1 = b_2$. The wave functions at two carbon atoms in a unit cell are in phase. This makes the overall energy lower. That is why this band is related to bonding orbitals. With the other eigenvalue, $b_1 = -b_2$. There is a phase difference of 180 degree and the energy is higher.

The 3D plot in Fig. 2.3 also shows that the two bands, bonding and anti-bonding, touch each other at 6 points. This illustrates that graphene is a zero-bandgap semiconductor since there is no bandgap. The dispersion relations near the touching points are conical. This statement and its implications will be discussed later.

The first Brillouin zone is show in the left image of Fig. 2.4. The reciprocal vectors are

$$\begin{aligned} \mathbf{b}_1 &= \frac{4\pi}{\sqrt{3}a} \left(\frac{1}{2}, \frac{\sqrt{3}}{2} \right) \\ \mathbf{b}_2 &= \frac{4\pi}{\sqrt{3}a} \left(\frac{1}{2}, -\frac{\sqrt{3}}{2} \right). \end{aligned} \quad (2.19)$$

It is easy to understand the 6 fold symmetry. The two bands touch at the corner of the first Brillouin zone, which are called K points by convention. But it is important to note that only two of out the six K points belong to first Brillouin zone. One way to look at it is that each K point is shared by three Brillouin zones. The first Brillouin zone only contains 1/3 of each cone at the six K points.

Indeed, the two K points highlighted with black dots in Fig. 2.4 can be mapped by reciprocal lattice vectors to the one denoted with a grey dot. The other three K points can be related in the same fashion and form another group. However any two K points from different groups can not be connected by a reciprocal lattice vector. So there are two, and only two, non-equivalent K points in the first Brillouin zone. This is usually called K K' degeneracy.

The first Brillouin zone can be rearranged as shown in Fig. 2.5. Unit 1 and 2 can be moved to Unit 1' and 2' by reciprocal vector $\mathbf{b}_1 + \mathbf{b}_2$ and \mathbf{b}_1 . Unit 1', 2' and 3 form a triangular area defined by dashed lines. Now the whole cone near K point is sitting inside the first Brillouin zone. The other half of the hexagon can be rearranged into another triangle near K' point. In the next section, the band structure of carbon nanotubes will be derived based on that of graphene. It is helpful to use the form of the first Brillouin zone shown in Fig. 2.5.

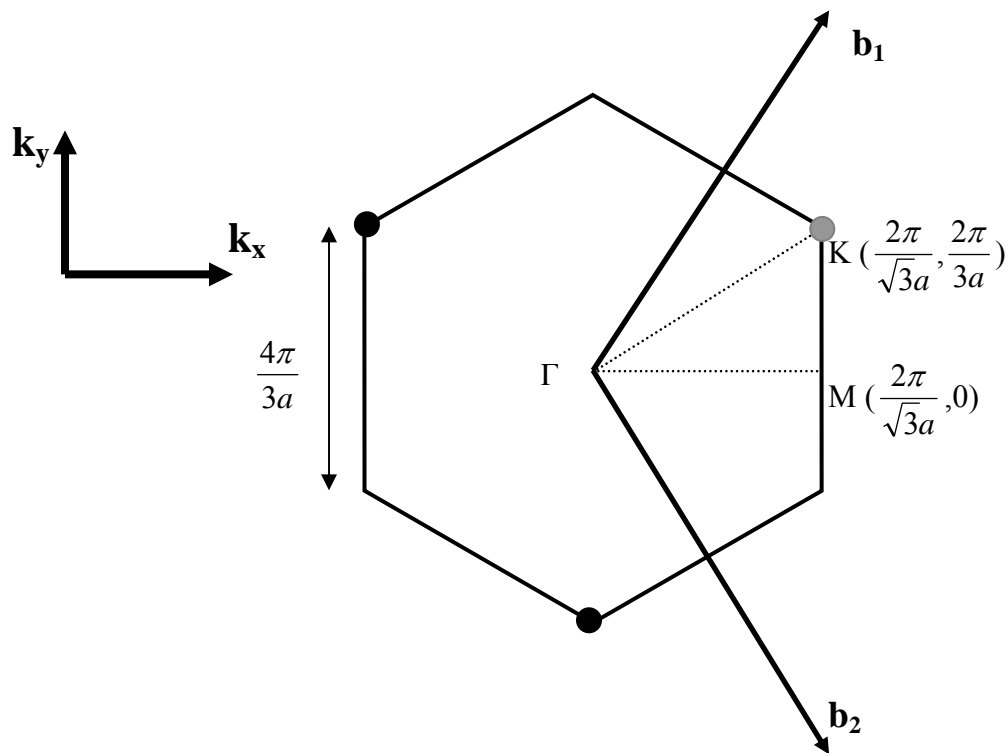


Figure 2.4: The first Brillouin zone of graphene.

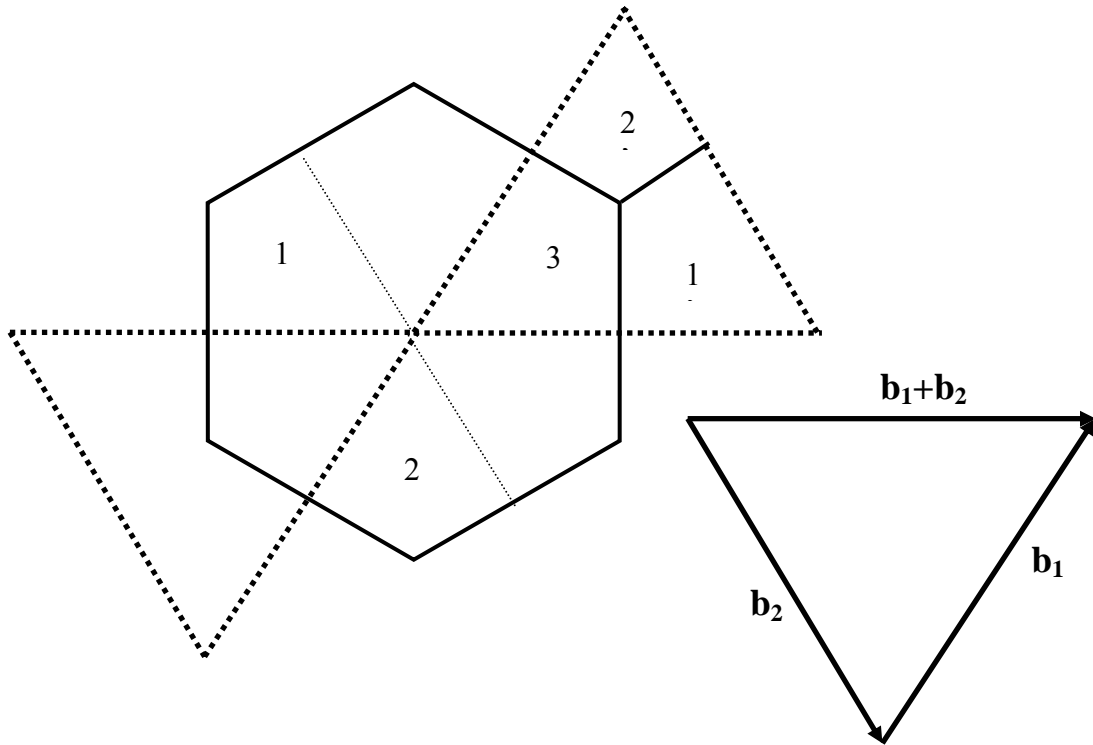


Figure 2.5: Reorganization of the first Brillouin zone to put the K and K' points in centers. The two triangles defined by dashes lines are the first Brillouin zone in a different presentation.

2.3 Making nanotubes from graphene

Nanotubes can be viewed as seamless cylinders rolled up from a piece of graphene. Since a 2D piece of graphene can be rolled up along different directions, the carbon atoms in the resulting nanotubes will be arranged with different patterns. As will be shown later, the way in which the nanotube is wrapped profoundly impacts the electronic properties of nanotubes.

Each tube can be uniquely labeled by a set of two integer numbers (n,m) that are determined by the chiral vector \mathbf{C}_h along the circumference: if the tube is made by joining atoms at \mathbf{O} and \mathbf{A} in Fig. 2.6, then $\mathbf{C}_h = \mathbf{OA} = n\mathbf{a}_1 + m\mathbf{a}_2$. The vector shown corresponds to $\mathbf{C}_h = 7\mathbf{a}_1 + 2\mathbf{a}_2$, and this tube is called a $(7, 2)$ tube. Due to the six-fold symmetry of a

triangular lattice, n and m are defined to be positive and satisfy $m < n$. The translational vector \mathbf{T} , which is perpendicular to the chiral vector \mathbf{C}_h , is apparently along the tube axis.

Another way to label nanotubes is by their diameter d and chiral angle θ , which is the angle between the chiral vector of a nanotube and that of a zigzag tube (Fig. 2.6). It can be proven easily, through simple geometry, that these two labeling methods are equivalent. The conversion rules are written in Eq. 2.20:

$$\begin{aligned} \cos \theta &= \frac{2n + m}{2\sqrt{n^2 + nm + m^2}} \\ d &= \frac{a}{\pi} \sqrt{n^2 + nm + m^2} \end{aligned} \quad (2.20)$$

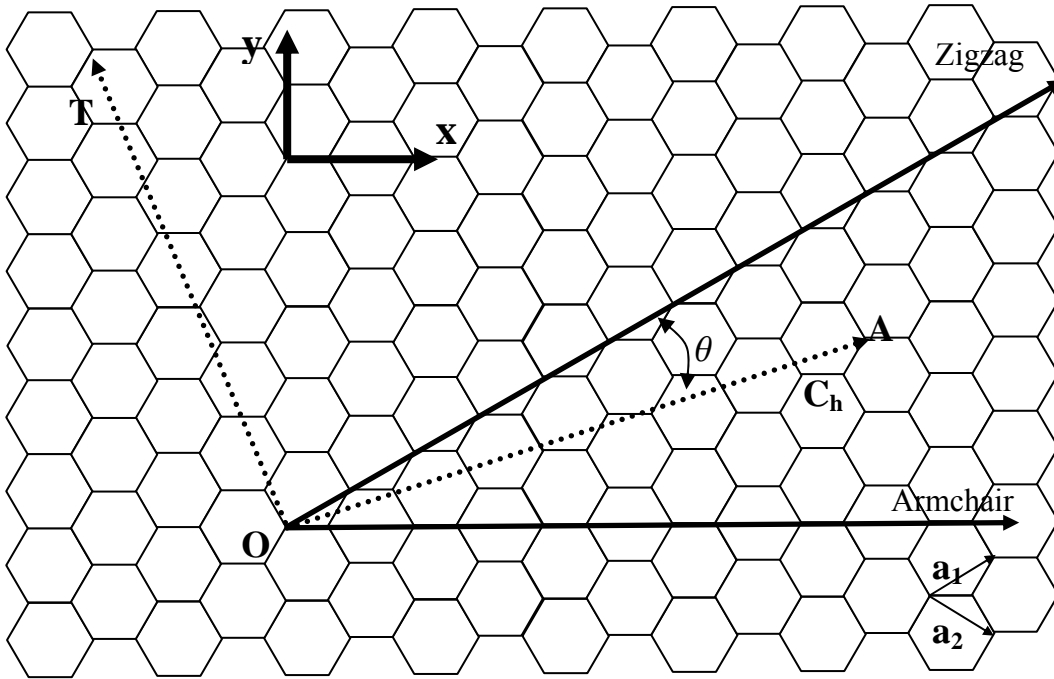


Figure 2.6: Making nanotubes from graphene. The circumference vector \mathbf{C}_h , which connects two points that will be ‘fused’ into one when the graphene is rolled into a seamless nanotube, is showed as OA. The tube axis will be along OT. The circumference vectors of two special types of tubes are shown: armchair and zigzag.

The two dark lines in Fig 2.6 are the chiral vector of two special tubes. Zigzag tubes have chiral vector parallel to \mathbf{a}_1 so that m always equals zero. The name is given because the carbon atoms along circumference go up and down in a zig-zag pattern. The chiral vector of armchair tubes is along $\mathbf{a}_1 + \mathbf{a}_2$, which makes $n = m$. The atoms along their circumferences go up, down, down and up.

With the (d, θ) notation, zigzag tube and armchair tubes have special chiral angles. For zigzag, θ equals 0. And θ is 30° for armchair tubes. Due to the six fold symmetry of the graphene lattice, chiral angles of all other tubes are between these two values. The diameter of nanotube cannot be infinitely small because the bending energy associated with large curvature makes this structure unfavorable against graphene. The smallest nanotube ever observed has diameter of 0.4 nm, and is the inner layer of a large multi-walled nanotubes (Qin et al. 2000). This smallest tube roughly corresponds to a nanotube with $n + m$ around six. The diameter, 0.4nm, is smaller than that of the smallest fullerene C_{60} , 0.7nm.

2.4 Band structure of carbon nanotubes

Next, the band structure of carbon nanotubes will be deduced from that of graphene. The difference is that electrons in nanotubes are confined along the circumference. Because the diameter of SWNT is on the order of 1 nm, the wave vector along the circumference k_\perp is quantized according to Eq. 2.21:

$$k_\perp = \frac{2}{d}q = k_q q \quad q = \pm 1, \dots, \pm N, \quad (2.21)$$

where N is the number of hexagons in the unit cell define by chiral vector \mathbf{C}_h and translational vector \mathbf{T} , and $k_q = 2/d$ is the step size in k_\perp . Since the length of nanotubes is macroscopic, typically from one μm to hundreds of μm , the wave vector along the tube axis k_\parallel is considered continuous.

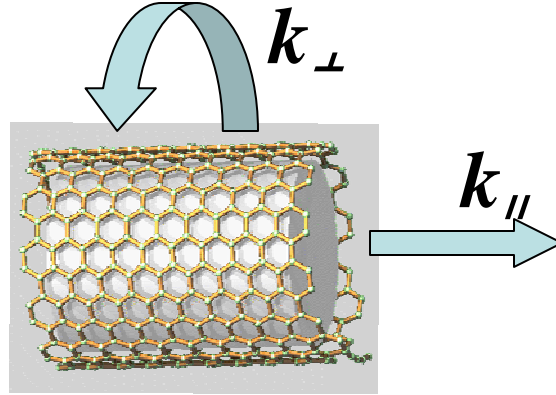


Figure 2.7: The electron wave vector along the circumference of a nanotube is quantized.

Due to the quantization of k_{\perp} , not all the points in the graphene bands derived in Section 2.2 are accessible to nanotubes. Instead, the energy bands of a nanotube are limited to a series of 2D subbands with constant k_{\perp} values. The dashed line in Fig. 2.8 is along the k_{\parallel} direction and the angle between it and $\Gamma\mathbf{K}$ is the chiral angle θ . The solid lines, which are perpendicular to the dashed line, have constant k_{\perp} values. The energy of these 2D subbands is governed by the alignment of k_{\perp} with respect to the K point. The subband with k_{\perp} closest to the K point defines the lower energy subband. Because the graphene band structure does not have a bandgap at K point, if one of these k_{\perp} goes through K points, this nanotube will be metallic, i.e. gapless. Otherwise the dispersion relation of this nanotube has a bandgap and the tube is semiconducting.

It is simple to prove that 1/3 of all nanotubes are metallic. This can be viewed as an entry-level geometry problem. If a line is drawn from K point to intersect the dashed line in Fig. 2.8 at right angle, the distance between Γ point and the intersection point is $4\pi/(3a \times \cos\theta)$. The question boils down to whether the ratio between this length and k_q is an integer. With Eq. 2.20, it is easy to get

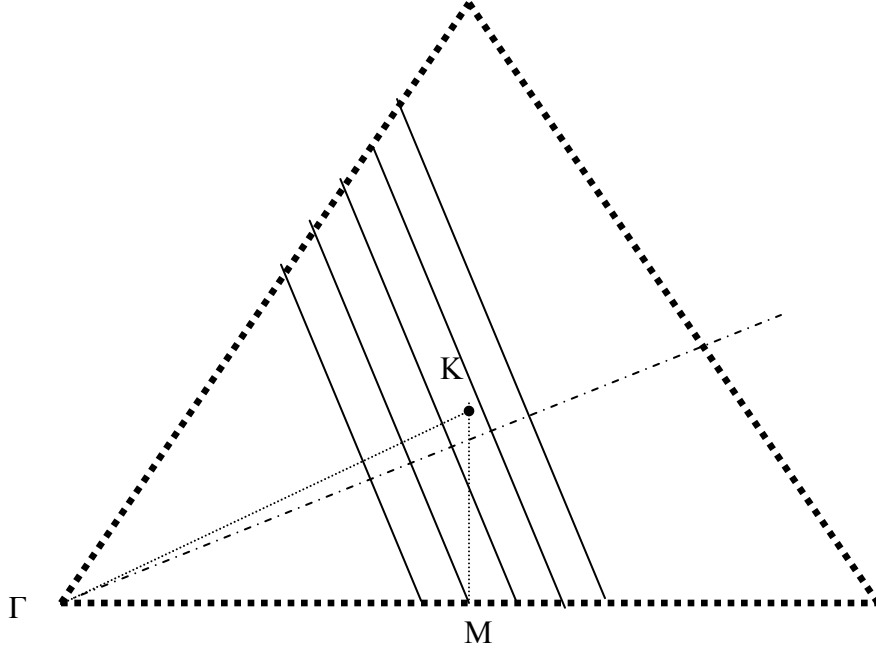


Figure 2.8: Extracting band structure of nanotubes from that of graphene.

$$\frac{4\pi}{3a \times \cos \theta} / \frac{2}{d} = \frac{2n+m}{3} = n - \frac{n-m}{3}. \quad (2.22)$$

If $(n-m)/3$ is an integer, then the subband with $k_{\perp} = 2(2n+m)/3d$ will go through K point and give a gapless dispersion relation. If $(n-m)/3$ is not an integer, the tubes are semiconducting. That means 1/3 of nanotubes are metallic and 2/3 are semiconducting. They can be further categorized into two types: $n-m = 3j+1$ and $n-m = 3j-1$ with j being integers. Ethan Minot's thesis (Minot 2004) discusses how these two types of tubes are influenced differently by perturbations like stain or magnetic field along the tube axis.

The degeneracy between K and K', mentioned in Section 2.2, leads to a two-fold degeneracy in subbands. Due to the symmetry, subbands with $k_{\perp} = |k_0|$ and $k_{\perp} = -|k_0|$ have exactly the same dispersion relation except that one is close to K point and the other close to K' points. Pictorially, the degenerate states correspond to electrons traveling down the tube clock wise or counter clock wise with the same energy.

We can also use mathematical formula to repeat the above discussion to understand the origins of subbands in nanotubes and to determine whether they are metallic or semiconducting. It can be shown that reciprocal vector along the circumferential direction of a (n,m) tube is

$$\mathbf{K}_1 = [(2n + m)\mathbf{b}_1 + (2m + n)\mathbf{b}_2] / 2(m^2 + nm + n^2) \quad (2.23)$$

and $|\mathbf{K}_1| = 2/d$. The wave vector along the circumference is a multiple of \mathbf{K}_1 .

As examples, consider the simple case of armchair tubes and zigzag tubes. For a (n,n) armchair tube,

$$\mathbf{K}_1 = \frac{\mathbf{b}_1 + \mathbf{b}_2}{2n} = \frac{2\pi}{\sqrt{3}an} \hat{\mathbf{x}} \quad (2.24)$$

The allowed k_\perp values are

$$\mathbf{K}_\perp = \frac{2\pi q}{\sqrt{3}an} \hat{\mathbf{x}}, \quad (2.25)$$

where q is an integer between $-n$ to n . Plug it into Eq. 2.18, the energy bands are

$$E_{k_\perp, k_\parallel} = \pm \gamma \sqrt{1 + 4 \cos\left(\frac{q\pi}{n}\right) \cos\left(\frac{k_\parallel a}{2}\right) + 4 \cos^2\left(\frac{k_\parallel a}{2}\right)} \quad (2.26)$$

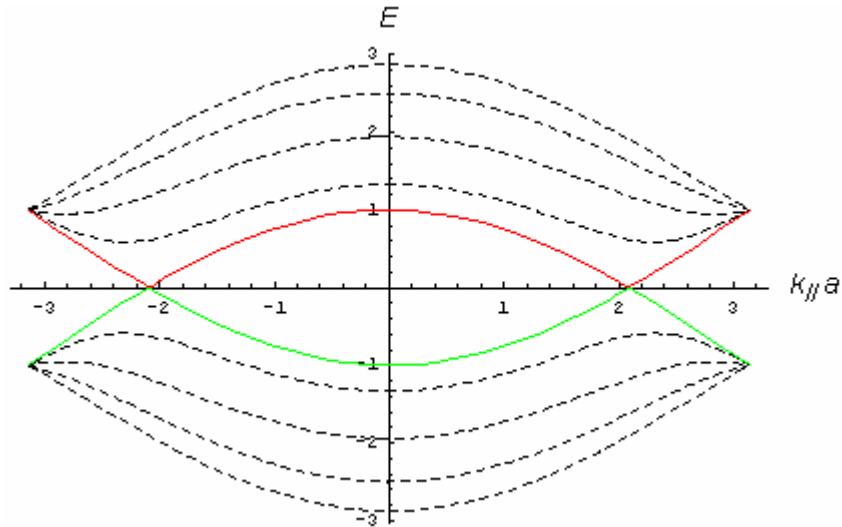


Figure 2.9: The subbands of a (5,5) armchair tube.

Figure 2.9 plots the subbands of a (5,5) armchair nanotubes using Eq. 2.26. The first subband, which has $q = 5$, is plotted in colors: conduction band in green and valence band in red. It is metallic because these two band meet at $k_{//} = 2\pi/3a$. The dispersion at the crossover point of the first subbands is close to linear. The higher bands are plotted in dotted lines.

For a (n,0) zigzag tube,

$$\mathbf{K}_1 = \frac{\mathbf{b}_1 + \frac{1}{2}\mathbf{b}_2}{n} = \frac{2\pi}{an} \left(\frac{\sqrt{3}}{2} + \frac{1}{2} \right) \quad (2.27)$$

It is along the ΓK direction. Since there is a 6-fold symmetry, it is easier to rotate everything by 60 degree to make \mathbf{k}_1 along \mathbf{k}_y direction. After rotation,

$$\mathbf{K}_1 = \frac{2\pi}{an} \hat{\mathbf{y}} \quad (2.28)$$

The energy bands are

$$E_{k_{\perp}, k_{//}} = \pm \gamma \sqrt{1 + 4 \cos\left(\frac{\sqrt{3}k_{//}a}{2}\right) \cos\left(\frac{q\pi}{n}\right) + 4 \cos^2\left(\frac{q\pi}{n}\right)} \quad (2.29)$$

The subbands of a (10,0) nanotubes are plotted on the left side of Fig. 2.10. Only the valence bands are shown since the valence and conduction bands are symmetric with respect to $E = 0$. This tube is a semiconducting one since there is a bandgap.

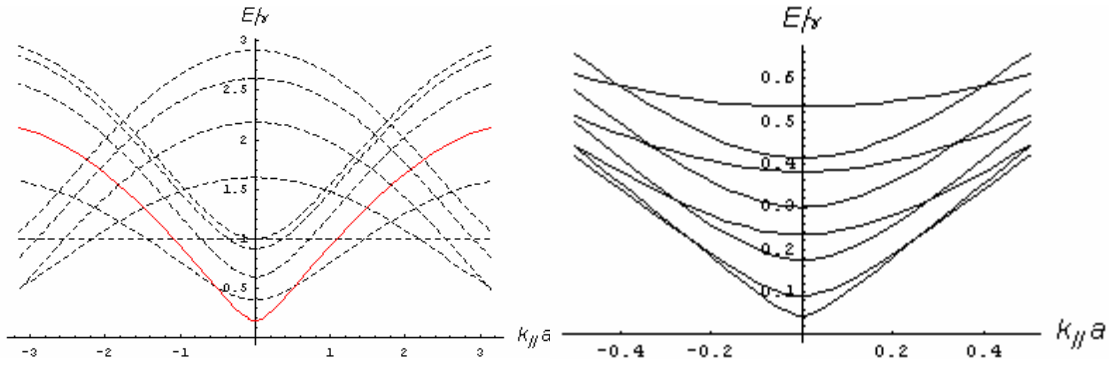


Figure 2.10: The subbands of a (10, 0) zigzag tube (**left**) and the first few subbands of a (40,0) zigzag tube (**right**).

In conclusion, nanotubes have a series of subbands. The energy difference between subbands is inversely proportional to tube diameter, and reaches more than 0.2 eV for small tubes as shown in Fig 2.10. 1/3 of all nanotubes do not have bandgap while the other 2/3 do. The dispersion relation can be extracted from Eq. 2.18.

2.5 Simplified band structure

In the previous section, the dispersion relation of nanotube is shown to be a sensitive function of (n,m). In many cases, however, it is easier to use a simplified expression of the energy dispersion relation for semiconducting nanotubes:

$$E = \pm \sqrt{\left(\frac{E_g}{2}\right)^2 + (\hbar v_F k_{\parallel})^2}, \quad (2.30)$$

where E_g is defined as bandgap and v_F is electron Fermi velocity. It looks like a relativistic dispersion with E_g playing the role as rest mass and v_F as the speed of light, and is nowhere near Eq. 2.18. The purposes of this section are to discuss how good this

approximation is and how the parameters like E_g and v_F are related to transfer integral γ and tube diameter d . Again these can be carried out in two ways.

If one wants to prove it mathematically, it is easier to use zigzag tube as an example. In the dispersion relation in Eq. 2.29, the energy of the valence band can reach zero if $q/n = 2/3$. However for a semiconducting tube n is not a multiple of 3, this condition cannot be satisfied. But we can pick q_0 to be the nearest integer to $2n/3$ and do Taylor expansion near $k_{//} = 0$ to the first order, then Eq. 2.29 can be written as

$$E_{k_{\perp}, k_{//}} = \pm \sqrt{\left[\gamma \left(1 + 2 \cos \left(\frac{q_0 \pi}{n} \right) \right) \right]^2 + \left(\frac{\sqrt{3}}{2} a \gamma k_{//} \right)^2} \quad (2.31)$$

Compare it with Eq. 2.30, we can see that

$$v_F = \frac{\sqrt{3} a \gamma}{2 \hbar} = \frac{3 a_{c-c} \gamma}{2 \hbar} \quad (2.32)$$

As mentioned in Section 2.2, electrons in crystals with larger transfer integral γ can travel easier and faster. Eq. 2.32 is a mathematical description of this observation. The transfer integral γ in graphene is about 2.7 eV and makes the Fermi velocity v_F in nanotubes to be around 8.7×10^5 m/s.

The first term in Eq. 2.31 is basically the bandgap. It is a function of how far apart the subband deviates from K point. When n goes larger, the value $q_0 - 2n/3$ grows smaller. That tells us the bandgap will be inversely proportional to tube diameter.

Another way to think about this issue is purely geometrical. If we assume the dispersion relation near K point to be exactly conical (as mentioned in Section 2.2, this is a good approximation at low energy), the energy of an electron is linearly proportional to the difference between its wave vector and $\Gamma\mathbf{K}$.

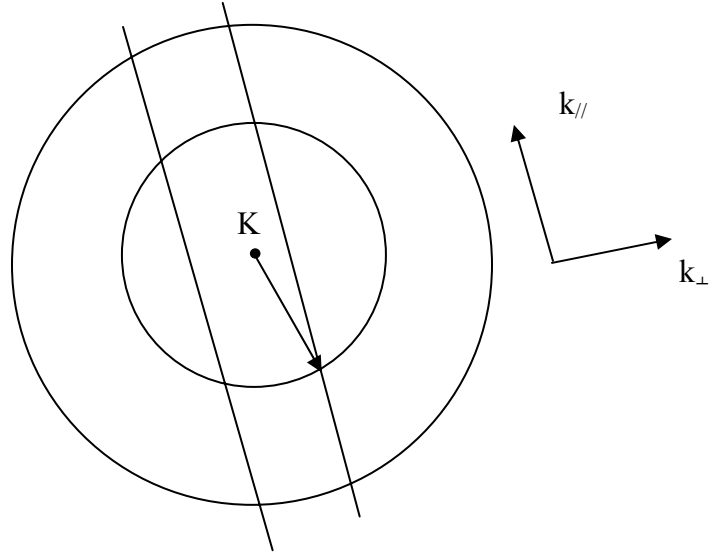


Figure 2.11: When the dispersion near K point is conical, the energy of an electron is proportional to the vector shown in this figure, which is the difference between the electron wavevector and $\Gamma\mathbf{K}$.

The dispersion relation under this approximation is

$$E_k = \pm \hbar v_F |k| = \pm \hbar v_F \sqrt{(\Gamma\mathbf{K} - k_\perp)^2 + k_\parallel^2}. \quad (2.33)$$

k_\perp equals $2q/d$. From Eq. 2.22, $\Gamma\mathbf{K} = 2(2n+m)/3d$. Then we have

$$E_k = \pm \hbar v_F |k| = \pm \sqrt{\left[\left(\frac{n-m}{3} + p \right) \frac{2\hbar v_F}{d} \right]^2 + (\hbar v_F k_\parallel)^2}, \quad (2.34)$$

where p is an integer. It is easy to see the bandgap equals

$$E_g = \frac{4\hbar v_F}{3d} \quad (2.35)$$

The bandgap is inversely proportional to diameter. When we use 2.7 eV as transfer integral, E_g is about 0.70 eV/ d[nm].

Next the validity of this simplified dispersion relation will be studied. Figure 2.12 shows the first subbands, calculated using different equations, of two zigzag tubes with different diameters. The left side figure is for a (10, 0) tube with diameter around 0.78 nm

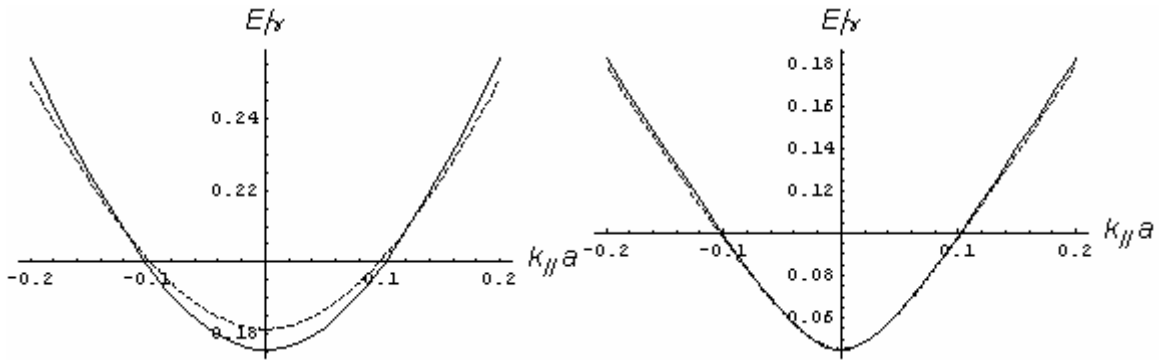


Figure 2.12: Comparison of nanotube band structures calculated from the simplified dispersion relation (dotted lines) and from the more rigorous one (solid lines). The left figure is for a (10,0) tube and the right one is for a (40,0) tube. The deviation decreases with increasing tube diameter.

and the right one is for (40,0) tube with $d = 3.1\text{nm}$. Dispersions according to Eq. 2.29 and Eq. 2.30 are plotted in solid lines and dotted lines. Clearly, this approximation works better for larger diameter tubes. This is because only the dispersion very close to K point is conical and tubes with large diameter can have wave vectors closer to K point.

Equation 2.34 implies the subband bottoms are located at $E = E_g/2, 2 \times E_g/2, 4 \times E_g/2, 5 \times E_g/2, \dots, (3j+1) \times E_g/2, (3j+2) \times E_g/2$ with j being integers. Not surprising, this rule works better on large diameter tubes. As Fig. 2.10 shows, this pattern exists in the first 5 subbands of a (40,0) tube, but does not apply to a (10,0) tube.

Another failure of Eq. 2.30 is it predicts there is no crossing between subbands. In Fig. 2.10, the subbands do cross. In conclusion, this approximation works better for large diameter tubes and in low energy regime. The advantages of this version are its simplicity and independence (ignorance) of chirality.

2.6 Effects of tube curvature and non-zero overlap integral

The calculations so far are relative simple and ignore a few significant details by taking several approximations. Two examples, tube curvature effect and non-zero overlap integral, will be pointed out and their consequences will be discussed in this section.

Tube curvature

When the nanotube band structure is derived from that of graphene, nanotubes are basically treated as narrow pieces of flat graphene in which electrons satisfy periodic boundary condition. In reality, however, nanotubes have curvatures and should be considered as curved pieces of graphene. This modifies some conclusions of Section 2.4; the degrees of deviations depend on tube diameters.

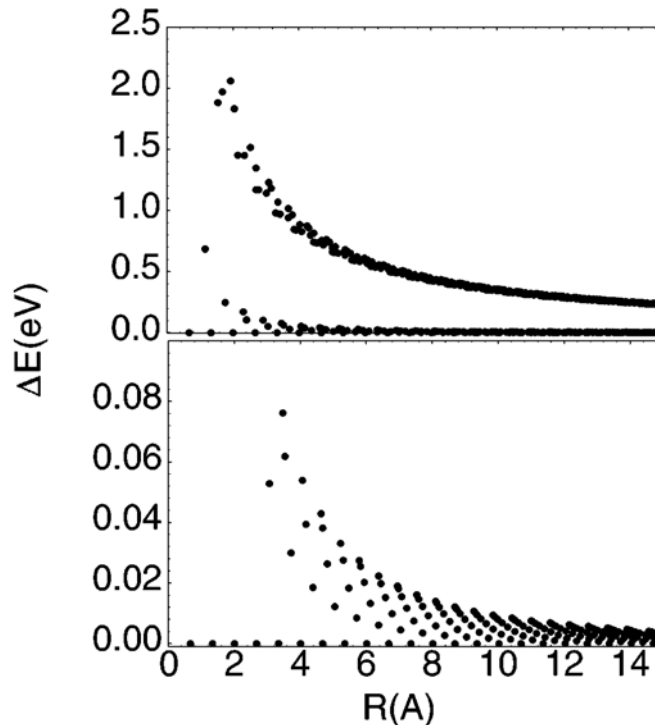


Figure 2.13: Calculated bandgaps of nanotubes with different diameter and chirality when curvature effect is taken in account (Kane and Mele 1997), shown on large energy scale (**top**) and on small energy scale (**bottom**).

The Kane group at University of Pennsylvania studied this issue in details (Kane and Mele 1997). Apparently curvature makes the lengths of C-C bonds vary in nanotubes, and the π orbitals of adjacent carbon atoms are no longer necessarily parallel. Both factors influence the transfer integral γ and make it depend on local curvature. When this is included into calculations, the bandgaps for nanotubes of different diameter and chirality are plotted in Fig. 2.13.

When nanotubes are large in diameter, as Fig. 2.13 shows, they are divided in two groups: with bandgaps and without. This agrees with the results of Section 2.4. When nanotube diameters are small, however, another group appears. It turns out curvature induces second order bandgaps in almost all nanotubes except armchair tubes, which appear to be gapless in Fig.2.13. Most of the “metallic” tubes in Section 2.4 also have bandgaps in this picture. This is why it is rare to find a nanotube FET that shows very little changes in conductance when the gate voltage is swept. Since small nanotubes have large curvature, the second order bandgap is only significant in small tubes. This curvature induced bandgap scales as $1/R^2$, as compared to the first order bandgap that scales as $1/R$ (Eq. 2.35). Curvature effects have to be considered for small diameter tubes.

When there are strains in a nanotube, they modify the lengths of C-C bonds and orientations of π orbitals too. The detailed discussed on how nanotube band structure is affected by strain can be found in Mint’s thesis (Minot 2004) .

Non-zero overlap integral

When the band structure of graphenes is derived in Section 2.2, a major approximation is taken. Namely, in Eq. 2.17 the overlap integral α is taken to be zero because it is smaller than unity. Figure 2.14 compares the dispersion along the ΓK direction with two different values of α : 0 eV (solid line) and 0.14 eV (dotted line). It shows that although the maximum energy difference can reach as high as $|\gamma|$, the two

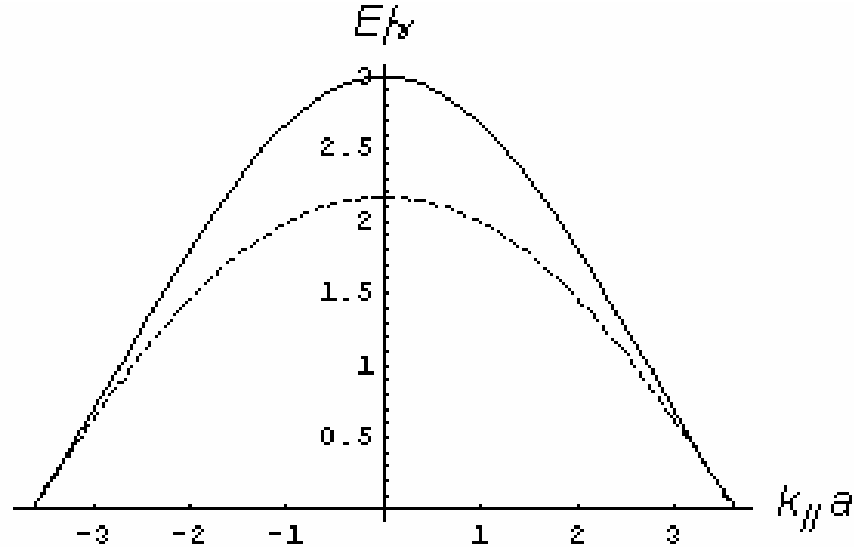


Figure 2.14: The influence of the overlap integral α on the graphene band structure. The results based on zero α (solid line) and non-zero α (dotted line) agree near K point, but separate from each other at large energy scale.

curves converge near K point. For low energy excitations, α can be chosen to be 0. However, due to the large separation between the subbands of small diameter nanotubes, the approximation, choosing α to be 0, may become invalid.

Figure 2.15 plots the first three subbands of a (10,0) nanotube. The solid lines are for standard approximation, $\alpha = 0$ eV. α is 0.14 eV in the dotted lines. The energy differences at the bottom of the second and third subband are around $0.018|\gamma|$ and $0.046|\gamma|$, or around 50meV and 120 meV. These are large values. The optical properties of nanotube are a hot research area now. Most of the researches are done with small diameter tubes because their bandgap is not too small, in the range of near infrared. The influence of non-zero α should be considered. They are on the same energy scales as excitons (Wang et al. 2005). Non-zero α has other implementations than modifying the

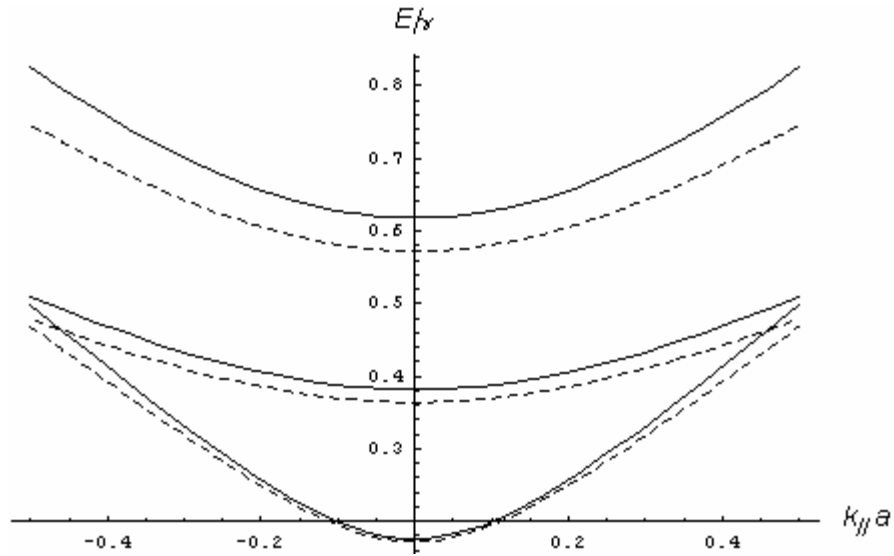


Figure 2.15: The influence of the overlap integral α on nanotube band structures. The first three subbands for a (10,0) tube are plotted based on zero α (solid lines) and based on non-zero α (dotted lines). The difference becomes significant beyond the second subband.

band structure (Goupalov 2005). But so far no experimental study has addressed this effect.

In summary, this chapter derives the dispersion relations of graphene and carbon nanotubes with tight-binding method. In nanotubes, the curvature of the bands at low energy and the bandgap, as well as the separation between the subbands, depend on tube diameters. A simplified version of nanotube dispersion relation that does not require the knowledge of the tube chirality is presented. The implications of a few approximations taken in this simple calculation are discussed in the last section. These results will be used in Chapter 3 to explain the observed electrical transport properties.

CHAPTER 3

ELECTRON-PHONON SCATTERING IN SEMICONDUCTING NANOTUBES

The electrical transport properties of SWNTs intrigued people ever since the discovery of SWNTs. Field-effect transistors (FETs) were first made from SWNTs several years ago (Tans et al. 1998) and have been subsequently investigated intensely for device (Bachtold et al. 2001; Liang et al. 2001; Javey et al. 2002; Rosenblatt et al. 2002) and sensing (Besteman et al. 2003; Star et al. 2003) applications. Both Schottky (Heinze et al. 2002) and low resistance (Javey et al. 2003; Yaish et al. 2004) contacts have been realized. It is expected that electron scatterings in nanotubes are suppressed due to various reasons in nanotubes. Therefore the mobility and conductance in nanotubes should be high. But the ultimate performance limits are not understood; for example, the reported mobility values vary by orders of magnitude in different studies (Shim et al. 2001; Rosenblatt et al. 2002; Durkop et al. 2004; Li et al. 2004).

This is partially because most groups have been interested in ballistic transport, where electrons can go through nanotubes without ever being scattered. This behavior has been observed by a few groups (Javey et al. 2003) using short nanotubes.

Diffusive transport, where electrons are scattered many times in the conduction channels either by defects or lattice vibrations, can tell many intrinsic properties of SWNTs and reveal their ultimate performance limits. In this chapter the properties of moderately long (4-15 μm) and oriented SWNT FETs with good contacts are systematically studied to probe the intrinsic transport properties. Specifically, we study the mobility and resistance values in nanotubes and their dependence on temperature and tube diameter. Both experimental data and theory calculations are presented (Zhou et al. 2005).

3.1 Experimental data

The devices used in this experiment are shown schematically in Fig. 3.1b. Using the recipe from the Liu group at Duke (Huang et al. 2003; Huang et al. 2004) SWNTs are grown on silicon wafers with 200 nm oxide. Figure 3.1a is an atomic force microscope (AFM) image of one of the devices. The tubes are long with little mechanical bending and oriented with the gas flow direction in the CVD growth furnace. The electrodes are made of either Au or Pd to make ohmic contact. In order to keep the SWNT free from rare defects, we choose the channel lengths L to be from 4 μm to 15 μm .

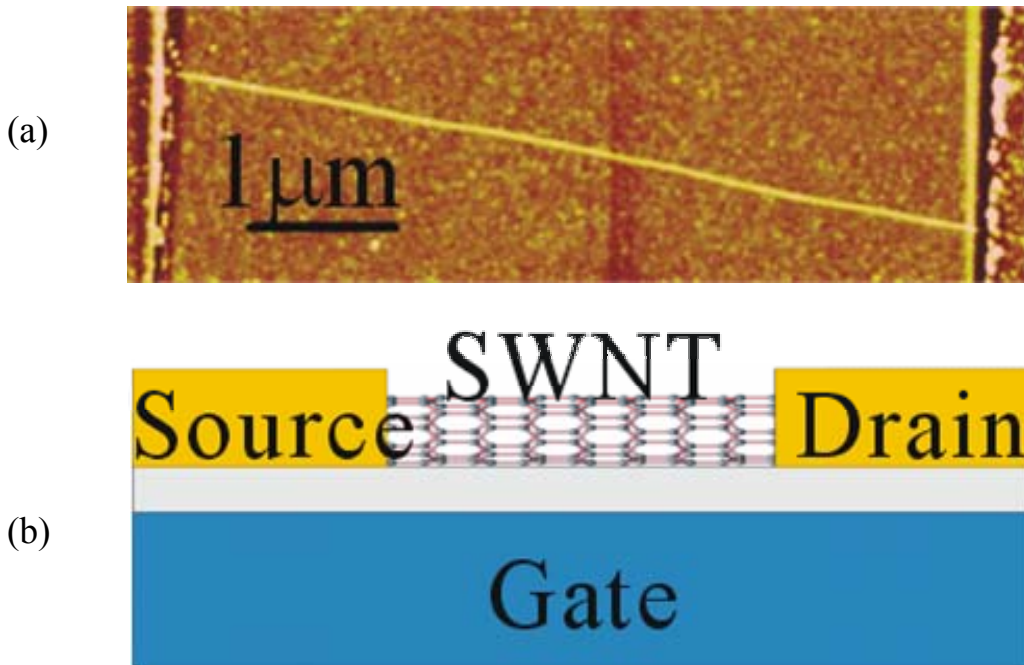


Figure 3.1: (a) AFM image of one device. (b) Schematic of device geometry. The gray layer is a 200 nm thick silicon oxide layer between the SWNT and the highly-doped silicon wafer used as backgate.

Figures 3.2 and 3.3 show the low-bias conductance in the p-type region for three SWNT FETs with different diameters as a function of backgate voltage¹. The main panel of Fig. 3.2 shows the temperature dependence of the conductance of one device with $d = 4$ nm and $L = 4$ μ m. The transition from off to on is more rapid and the maximum conductance increases with decreasing temperature. The resistance of the on-state, which is defined as when V_g is 10 V away from threshold voltage, decreases linearly with decreasing temperature down to 50 K, as shown in the upper inset. If we extrapolate the resistance linearly to zero temperature, the value of the intercept is 28 k Ω .

Figure 3.3 shows data from two other semiconducting SWNT FETs of different diameters. The maximum on-state conductance increases with d ; larger tubes have larger on-state conductance, and their conductance increases more dramatically upon cooling. This is shown in Fig. 3.4a, where data from a number of devices of different diameters are compiled. To minimize the influence of contact resistance, the temperature-dependent change is measured. The resistance of the same device is measured twice at room temperature and at around 50 K. The difference between these two values is normalized by tube length, and the inverse of this quantity is found to approximately scale linearly with tube diameter d .

¹ Devices show hysteresis. Only the upward sweep is shown in the figures and used to calculate mobility. This is because, after treating devices with PMMA passivation to get rid of the hysteresis as described by a Stanford group (Kim, W., A. Javey, O. Vermesh, O. Wang, Y. M. Li and H. J. Dai (2003). Hysteresis caused by water molecules in carbon nanotube field-effect transistors. *Nano Letters* **3**(2): 193-198.), the curve agrees with the upward sweep.

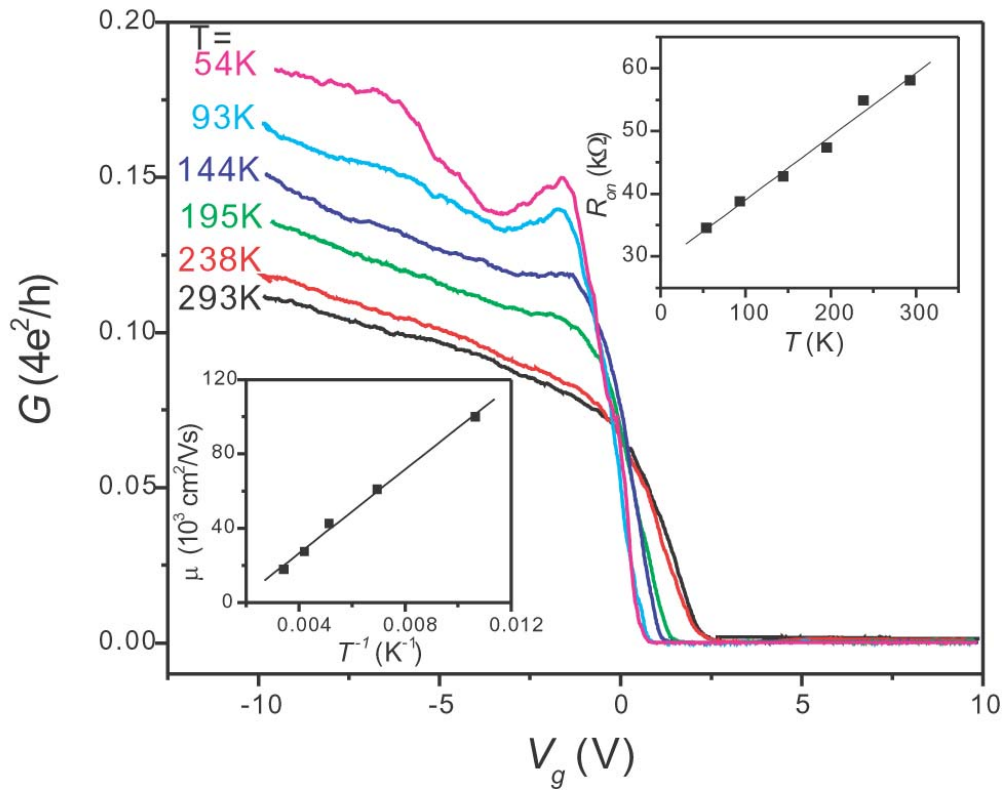


Figure 3.2: The conductance of a device with $d = 4$ nm and $L = 4$ μ m versus gate voltage at different temperatures. Upper inset: R_{on} as a function of T . Lower inset: measured mobility as a function of T^{-1} . Both are shown with linear fitting.

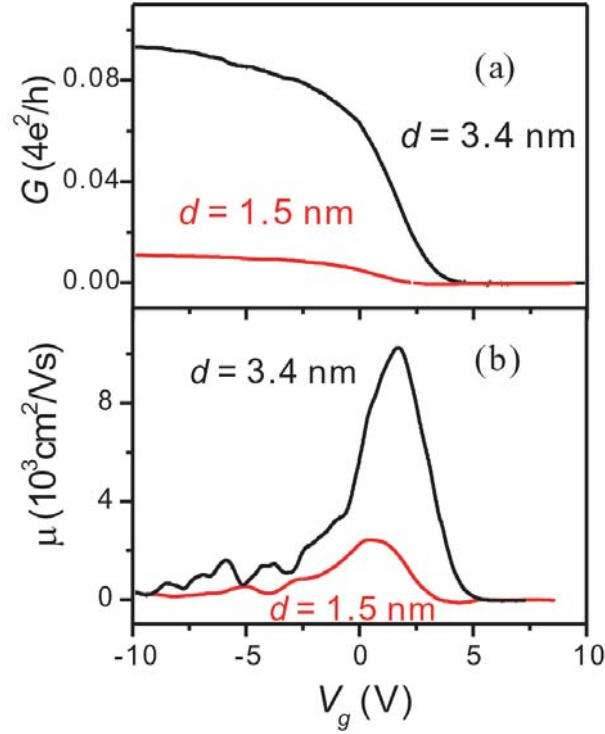


Figure 3.3: The conductance **(a)** and mobility **(b)** as functions of gate voltage for two different devices. The black curves are for a tube with $d = 3.4$ nm, $L = 5.4$ μm while the red curves are for a tube with $d = 1.5$ nm, $L = 10$ μm .

Shown in Fig. 3.3b are the field-effect mobilities for the two devices in Fig. 3.3a calculated using $\mu_{FE} = (L/C'_g)(dG/dV_g)$, where C'_g is estimated to be 2×10^{-11} F/m for $d = 4$ nm tube and it scales with diameter according to $C'_g{}^{-1} \propto \ln(1 + 2\lambda/d)$, where $\lambda = 200$ nm is the oxide thickness. The peak mobility is approximately $10,000$ $\text{cm}^2\text{V}^{-1}\text{s}^{-1}$ for the $d = 3.4$ nm, $L = 5.4$ μm tube, but about four times lower for the $d = 1.5$ nm, $L = 10$ μm tube. This is characteristic of all the devices measured; smaller-diameter tubes have lower

peak mobilities, as is shown in Fig. 3.4b. With the exception of a few devices with anomalously high mobilities (marked by circles in the plot), the data vary approximately as the square of the diameter (see inset to Fig. 3.4b).

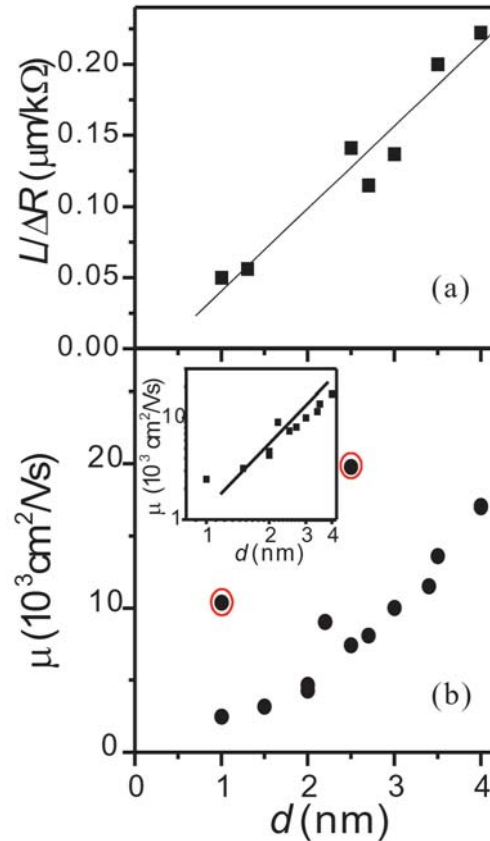


Figure 3.4: (a) Device length L divided by resistance change ΔR from room temperature to 50 K versus tube diameter with linear fitting shown. Data of similar diameter tubes are averaged. (b) Room temperature peak mobility as a function of tube diameter for many devices. Two devices showing anomalously large peak mobility are circled. Inset to (b): peak mobilities versus tube diameters on log-log scale with circled two data points omitted. The solid line is a visual reference line for square law.

To analyze these results, we first note that the device resistance is a combination of the intrinsic tube resistance R_{NT} and contact resistance R_c . To separately determine these contributions, we used an AFM tip as an electrical nanoprobe (Yaish et al. 2004). For the device in Fig. 3.2, at room temperature we find: $R_c \approx 28 \text{ k}\Omega$ and $R_{NT} \approx 30 \text{ k}\Omega$ at on-state. Note that R_c is the same as the extrapolated tube resistance at zero temperature (Fig. 3.2, upper inset). We therefore conclude that R_c is temperature-independent, and it is R_{on} , which is R_{NT} at on-state, that varies linearly with T , extrapolating to zero at $T = 0$. At room temperature, R_{on}/L is about $8 \text{ k}\Omega/\mu\text{m}$ for this semiconducting tube. This value is comparable to but somewhat higher than the resistivity of good metallic tubes (Mann et al. 2003; Park et al. 2004) and is similar to reported values for semiconducting tubes (Durkop et al. 2004; Li et al. 2004). This effect was also observed recently by a Columbia group (Purewal et al. 2007). At the lowest temperature shown ($T = 50\text{K}$), the device resistance is small ($R_{on} < 10 \text{ k}\Omega$), but still finite, corresponding to a minimum resistivity $R_{on}/L \sim 2.5 \text{ k}\Omega/\mu\text{m}$. At lower temperatures, the device resistance begins to increase, presumably due to the effects of localization and/or Coulomb blockade (Datta 1997; Kane et al. 1998).

The lower inset to Fig. 3.2 shows the peak mobility of the device at different temperatures after the constant contact resistance is taken into account. It varies approximately as T^{-1} , reaching $> 100,000 \text{ cm}^2\text{V}^{-1}\text{s}^{-1}$ at 50 K.

To summarize the experimental findings: R_{on} and μ^{-1} both increase linearly with T . Both depend strongly on diameter, but in different ways: $1/R_{on} \sim d$ and $\mu \sim d^2$. The resistivity and peak mobility of a 4 nm nanotube is about $8 \text{ k}\Omega/\mu\text{m}$ and $15,000 \text{ cm}^2\text{V}^{-1}\text{s}^{-1}$ at room temperature. In the next section, we present calculations of electron-phonon scatterings and compare with these results.

The only exception to the conclusions is that a few of the devices showed anomalously large peak mobilities, as indicated by the circled data points in Fig. 3.4b. To understand the origin of this behavior, we used scanned gate microscopy (Bachtold et al.

2000) to explore the uniformity of the conduction near the threshold region. In brief, a biased AFM tip is used as a local gate and the conductance of the device is recorded as a function of the AFM tip position. The results are shown in Fig. 3.5. For most devices, the response to the tip was relatively uniform (Fig. 3.5a), indicating that no single spot dominated transport. For the devices with anomalously high mobilities, we found that the gate response was primarily localized to a few dominant spots. In this case, using the equation $\mu_{FE} = (L/C'_g)(dG/dV_g)$, where L is the entire length of the tube, dramatically overstates the true mobility. This effect may also explain some of the extremely high values for the mobility reported in the literature (Durkop et al. 2004).

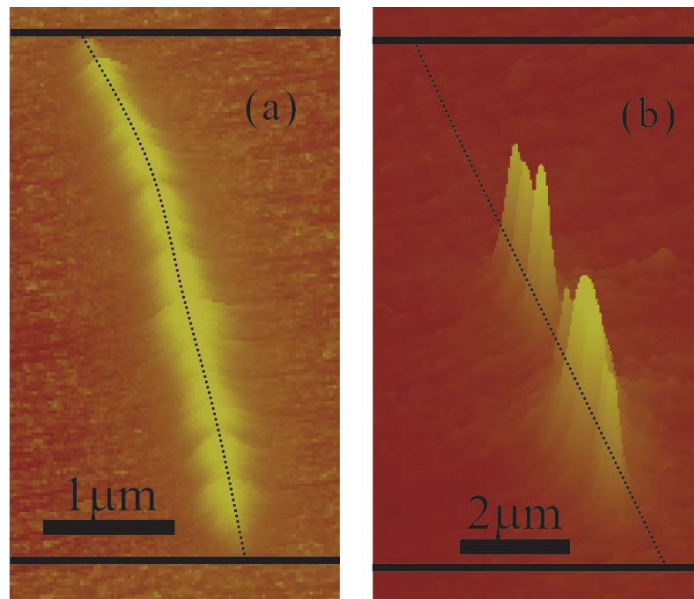


Figure 3.5: Scanned gate microscopy images of the device studied in Fig. 3.2 with normal peak mobility **(a)** and the circled $d = 2.5$ nm device with anomalously high peak mobility in Fig. 3.4b **(b)**. The solid lines indicate the position of electrodes and dashed lines indicate the position of SWNT. The device in **(b)** is dominated by a few short segments of tube near the threshold region. Therefore the mobility is overstated when the whole tube length is used to calculate the mobility.

3.2 Semiclassical transport, Boltzmann equation and the relaxation time approximation

In Chapter 2 the Schrödinger equation (Eq. 2.9) was solved to get the electron eigenstates and eigenvalues in nanotubes. When there are perturbations, *e.g.* electrical or magnetic fields, additional to the periodic crystal potential, however they must be included in the Schrödinger equation. But a shortcut is typically taken: keep the eigenstates of electrons and treat them as semiclassical particles. For example, in this picture electrons will still be driven by external electrical fields, but their properties, *e.g.* effective mass and dispersion, are determined by the band structure derived from the original Schrödinger equation. They are called Bloch electrons. The most important laws under this semiclassical treatment are listed in Eq. 3.1

$$\begin{aligned}\dot{\mathbf{r}} &= \mathbf{v}(\mathbf{k}) = \frac{1}{\hbar} \frac{\partial E(\mathbf{k})}{\partial \mathbf{k}} \quad (3.1) \\ \hbar \dot{\mathbf{k}} &= \mathbf{F}\end{aligned}$$

One implication of Eq. 3.1 is that Bloch electrons have different masses than electron rest mass. The so-called effective mass of an electron can be calculated from the band structure as shown in Eq. 3.2:

$$\frac{1}{m^*} = \frac{1}{\hbar} \frac{\partial^2 E(\mathbf{k})}{\partial \mathbf{k}^2} \quad (3.2)$$

Because the wave functions of Bloch electrons are eigenstates of the lattice potential, they should travel through the lattice without any resistance. However, this almost never happens because no crystal can be perfect. The imperfections come from two main categories: defects, *i.e.* static imperfections, and phonons, *i.e.* the thermal motion of atoms in a crystal. Both of them destroy the periodicity of the crystal potential and make the wavefunctions of Bloch electrons of a perfect crystal no longer the eigenstates. In semiclassical picture, electrons, still in the eigenstates of perfect crystals, collide with defects and phonons and get scattered. This is how resistance arises in a crystal.

In semiclassical treatments, electrons are assumed to travel according to Eq. 3.1 between collisions. The influence of collision events is centralized into the calculation of a local electron distribution function $g(\mathbf{k}, \mathbf{r}, t)$, which describes the number of electrons sitting at states $E(\mathbf{k})$ at time t and location \mathbf{r} . It is similar to the Fermi-Dirac distribution in a thermally equilibrated system,

$$f(\mathbf{k}) = \frac{1}{e^{(E(\mathbf{k}) - \mu)/k_B T} + 1}. \quad (3.3)$$

Transport currents and scattering will change the electron distributions, making it necessary to replace $f(\mathbf{k})$ with $g(\mathbf{k}, \mathbf{r}, t)$.

The way to calculate the distribution function is by the celebrated Boltzmann equation

$$\frac{\partial g}{\partial t} + \mathbf{v} \cdot \frac{\partial}{\partial \mathbf{r}} g + \mathbf{F} \cdot \frac{1}{\hbar} \frac{\partial}{\partial \mathbf{k}} g = \left(\frac{\partial g}{\partial t} \right)_{collision}. \quad (3.4)$$

The derivation of this equation can be found in solid state physics textbooks (Ashcroft and Mermin 1976). It describes how the local distribution function g evolves, in real space and momentum space, due to applied forces and collisions, whose effects are summed up by the term on the right hand side. To calculate this term, we need detailed physical origins of the collisions as well as the distribution function itself. The simplest approach is called the relaxation time approximation:

$$\left(\frac{\partial g}{\partial t} \right)_{collision} = \frac{g(\mathbf{k}) - g^0(\mathbf{k})}{\tau(\mathbf{k})}, \quad (3.5)$$

where $g^0(\mathbf{k})$ is the local equilibrium distribution function and $\tau(\mathbf{k})$ is called the relaxation time.

Equation 3.5 is a major simplification in the sense that the relaxation time $\tau(\mathbf{k})$ does not depend on $g(\mathbf{k})$. The way to understand Eq. 3.5 is it shows that collisions make the distribution function relax back to its steady state. And the time scale of that relaxation is $\tau(\mathbf{k})$.

We will try to derive conductivity under an electrical field \mathbf{E} using the above formalism. Since the external field is going to change g , we can expand g with respect to the electrical field. For simplicity, we ignore higher order terms and only keep the first two terms:

$$g = g_0 + g_1, \quad (3.6)$$

where g_0 is independent of \mathbf{E} and g_1 grows linearly with \mathbf{E} . The first two terms of Boltzmann equation (Eq. 3.4) disappear in a uniform conductor at steady state. With the relaxation time approximation, it becomes

$$-\frac{e}{\hbar} \mathbf{E} \cdot \frac{\partial}{\partial \mathbf{k}} g = -\frac{g - g_0}{\tau}. \quad (3.7)$$

Expanding g in the form of Eq. 3.6 gives

$$-\frac{e}{\hbar} \mathbf{E} \cdot \frac{\partial}{\partial \mathbf{k}} g_0 - \frac{e}{\hbar} \mathbf{E} \cdot \frac{\partial}{\partial \mathbf{k}} g_1 = -\frac{g_1}{\tau} \quad (3.8)$$

Compare the terms with the same order of \mathbf{E} on both sides and keep only the first order terms:

$$g_1 = \frac{e\tau}{\hbar} \mathbf{E} \cdot \frac{\partial}{\partial \mathbf{k}} g_0 = \frac{e\tau}{\hbar} \mathbf{E} \cdot \frac{\partial E(\mathbf{k})}{\partial \mathbf{k}} \left(\frac{\partial g_0}{\partial E} \right) = e\tau(k) \mathbf{E} \cdot \mathbf{v}(\mathbf{k}) \left(\frac{\partial g_0}{\partial E} \right). \quad (3.9)$$

We have derived the distribution function to the first order approximation in a general form. It depends on the band structure as well as an important parameter, the relaxation time $\tau(k)$. In principle, every transport phenomenon can be calculated from Eq. 3.9. $\tau(k)$ will be derived in the next section. Since it depends on atomic details of the lattice and the collision mechanism, the calculation will be nanotube-specific.

3.3 Electron-Phonon scattering in nanotubes

In quantum mechanics, the transition rate from one eigenstate to another due to perturbations is calculated using the Fermi's golden rule

$$\Gamma_{i \rightarrow f} = \frac{2\pi}{\hbar} |\langle f | H' | i \rangle|^2 \delta(E_i - E_f - \hbar\omega), \quad (3.10)$$

where H' is the matrix element that describes the interaction causing the transition, which is the electron phonon interaction in this section, and ω is the angular frequency of the perturbation if it is oscillating in time.

Generally, collisions can come from two sources: lattice vibrations and defects. We will focus on how electrons are scattered by phonons. A phonon, or one mode of lattice vibration, moves atoms out of their equilibrium positions. The crystal potential associated with the positions of the atoms will oscillate too. We need to find out how this acts as a perturbation for the electrons in the crystal.

Define the potential induced by an atom at position \mathbf{R}_n as $V(\mathbf{r} - \mathbf{R}_n)$. When the atom moves by a displacement $\boldsymbol{\mu}_n$, the potential becomes $V[\mathbf{r} - (\mathbf{R}_n + \boldsymbol{\mu}_n)]$. The potential change at location \mathbf{r} is

$$\delta V_n = V[\mathbf{r} - (\mathbf{R}_n + \boldsymbol{\mu}_n)] - V(\mathbf{r} - \mathbf{R}_n) \approx -\boldsymbol{\mu}_n \cdot \nabla V(\mathbf{r} - \mathbf{R}_n) \quad (3.11)$$

To the first order, it is linearly proportional to the displacement $\boldsymbol{\mu}_n$. This is why under deformation potential theory (Bardeen and Shockley 1950), the matrix element is assumed to be

$$H' = D\boldsymbol{\mu}_n(\mathbf{r}), \quad (3.12)$$

where D , the proportional coefficient between H' and the displacement, is called the deformation potential. The calculation of D is beyond the scope of this thesis. It is assumed to be constant for all tubes (Suzuura and Ando 2002; Pennington and Goldsman 2003). The validity of this assumption is discussed in Appendix B. The matrix element is then

$$H' = \langle k' | D\boldsymbol{\mu}_n(\mathbf{r}) | k \rangle. \quad (3.13)$$

A group at University of Maryland (Pennington and Goldsman 2003) did a detailed calculation of Eq. 3.13. A lengthy derivation gives the following result

$$\Gamma(k_{\perp}) = \frac{\hbar D^2 q_z^2}{2\rho E(q_z)} \times \left(N[E(q_z)] + \frac{1}{2}(\pm)\frac{1}{2} \right) DOS, \quad (3.14)$$

where q_z and $E(q_z)$ are the phonon wavevector and energy, $N[E(q_z)]$ is the phonon occupation number governed by Bose-Einstein distribution, DOS is the density of states, and ρ is the mass density along the tube axis.

When temperature is high, $N[E(q_z)] = k_B T/E(q_z)$, the transition rate is simplified to

$$\Gamma(k_{\perp}) = \frac{k_B T D^2}{2\rho \hbar v_s^2} DOS, \quad (3.15)$$

where v_s is the sound velocity² in nanotubes. For a nanotube at constant temperature, Γ scales with the DOS at the Fermi level. Figure 3.6b shows the DOS of a semiconducting nanotube. There are a series of peaks called 1D Van Hove singularities. Figure 3.6a shows the first two subbands of a semiconducting nanotube. The Van Hove singularities occur when the energy is at the onsets of these subbands. If the conduction is confined in the first subband, the DOS goes from infinite at the band bottom to a constant value at high Fermi energy as Figure 3.6b shows. This indicates the transition rate is large at small Fermi energy, and decays to a constant value at higher E_F according to Eq. 3.15.

² The sound velocity in nanotube v_s is around $\sim 10^1$ km/s, and is much smaller than the Fermi velocity in nanotubes, 8×10^2 km/s. The energy of phonons, $\hbar\omega = \hbar v_s q_z$, are typically ignored and the scatterings are considered elastic.

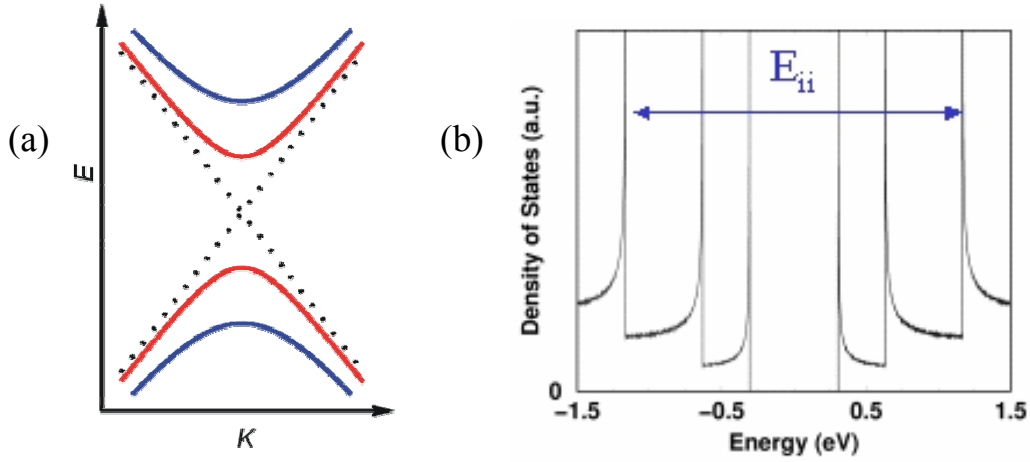


Figure 3.6: (a) The band structure of a semiconducting nanotube. The dispersions of the first two subbands are shown. (b) The DOS of a 1 nm diameter semiconducting nanotube. E_{ii} is the energy difference between the i th conduction and valence subbands at band bottoms.

Note the DOS at high Fermi energy converges to a constant value, $1/hv_F$, the same as the DOS in a metal tube. The minimum transition rate of nanotubes of different diameters is determined by the pre-factors in Eq. 3.15. Apparently, the mass density goes linearly with tube diameter, it is easy to conclude that

$$\Gamma_{\min} \sim \frac{T}{d} \quad (3.16)$$

So far, the task of this section has been accomplished. The transition rate T , the inverse of the relaxation time τ , has been calculated. Its dependence on temperature and tube diameter is shown in Eq. 3.16.

3.4 A model of electron-phonon scattering limited conduction in nanotubes

The validity of the derivations in the previous two sections will be discussed in Appendix B. But it is instructive to put everything of Section 3.2 and 3.3 together to see what these simple calculations can predict.

Continuing from Section 3.2, to the first order, the distribution functions is

$$g = g_0 + g_1. \quad (3.17)$$

The current is then

$$I = e \int 2 \times 2 \times g \times v(k) dk / 2\pi = 4e \int g_0 v(k) dk / 2\pi + 4e \int g_1 v(k) dk / 2\pi. \quad (3.18)$$

The factor 2×2 comes from spin and K, K' degeneracy. The first term is zero because it corresponds to the equilibrium currents that flow oppositely with the same magnitude.

With Eq. 3.9, the second term can be written as

$$I = 4e \int e \tau \mathbf{E} v(k) \frac{1}{\hbar} \frac{\partial E}{\partial k} \frac{dk}{2\pi} \left(\frac{\partial g_0}{\partial E} \right) = \frac{4e^2}{h} \int \tau \mathbf{E} v(k) \left(\frac{\partial g_0}{\partial E} \right) dE. \quad (3.19)$$

When the low temperature limit is taken where $\partial g / \partial E$ is not zero only at the Fermi level, the current simply becomes

$$I = \frac{4e^2}{h} \tau \mathbf{E} v(k) \Big|_{k=k_F}. \quad (3.20)$$

That indicates the conductance is

$$G = \frac{4e^2}{h} \frac{\tau(k_F) v(k_F)}{L} = \frac{4e^2}{h} \frac{l_{mfp}}{L}, \quad (3.21)$$

where L is the nanotube length and $l_{mfp} = \tau(k_F) v(k_F)$ is the so-called mean free path. l_{mfp} describes how far an electron can travel before experiencing a collision. The constant e^2/h is the universal conductance quantum. It equals the conductance of a ballistic 1D channel for a single spin mode. The factor 4 comes from the spin and KK' degeneracies. Since Eq. 3.21 is derived from a diffusive conduction model, which is valid only when l_{mfp} is smaller than the geometric length. That means G should always be no more than $4e^2/h$ for a single subband. There are typically contact resistances present in series of the intrinsic

resistance of the conduction channel. The observed G will always be smaller than $4e^2/h$ in that case.

Eq. 3.21 shows the value of G grows linearly with the mean free path. l_{mfp} can be calculated from the knowledge we already have. $v(k_F)$ is determined by the band structure. With the simplified version of dispersion relation in Eq. 2.30,

$$v(k_F) = v_0 \frac{\hbar v_0 k_F}{\sqrt{\left(\frac{Eg}{2}\right)^2 + (\hbar v_0 k_F)^2}}. \quad (3.22)$$

Here v_0 is the Fermi velocity of a metallic tube, or the slope of the Dirac cones of a graphene sheet. From Section 3.3, it is known that $\Gamma(k)$ goes linearly with the density of states at the Fermi level. In a 1D system,

$$DOS = \frac{dN}{dE} = \frac{dN}{dk} \frac{dk}{dE} = \frac{L}{2\pi} \frac{dk}{dE} \sim v^{-1}. \quad (3.23)$$

So the relaxation time τ , the inverse of transition rate $\Gamma(k)$, is linearly proportional to $v(k_F)$. If we define τ_0 as the relaxation time when Fermi level reaches the linear dispersion regime, then

$$\tau(k_F) = \frac{v_F}{v_0} \tau_0. \quad (3.24)$$

When Eqs. 3.22 and 3.24 are plugged into Eq. 3.21, the conductance becomes

$$G = \frac{4e^2}{h} \frac{\tau_0 v_0}{L} \frac{(\hbar v_0 k_F)^2}{\left(\frac{Eg}{2}\right)^2 + (\hbar v_0 k_F)^2} = \frac{4e^2}{h} \frac{l_0}{L} \frac{1}{1 + \left(\frac{2}{3dk_F}\right)^2}. \quad (3.25)$$

It only depends on the position of the Fermi level. k_F is determined by the number of electrons in the tube. In our experiment, this is controlled through a gate placed next to the tube with a dielectric layer in between (Fig. 3.1b). Define C'_g as the gate capacitance per unit length and assume the threshold voltage, where the Fermi level is at the bottom of the first subband, is zero, then

$$k_F = \frac{2\pi}{L} \frac{1}{8} \frac{C'_g L V_g}{e} = \frac{\pi C'_g V_g}{4e}. \quad (3.26)$$

The factor 1/8 comes from spin, K, K' and $\pm k$ degeneracy. This leads to a gate voltage-dependent conductance

$$G = \frac{4e^2}{h} \frac{l_0}{L} \frac{1}{1 + \left(\frac{8e}{3\pi d C'_g V_g} \right)^2} = \frac{4e^2}{h} \frac{l_0}{L} \frac{1}{1 + (a/V_g)^2}. \quad (3.27)$$

The parameter a , defined as $a = 8e/3\pi d C'_g$, is determined by the nanotube diameter d and C'_g , determined the geometry of the FET device as shown in Fig. 3.1b. Figure 3.7 shows conductance as a function of gate voltage according to Eq. 3.25. The G initially goes quadratically at small gate voltage and reaches saturation at large V_g .

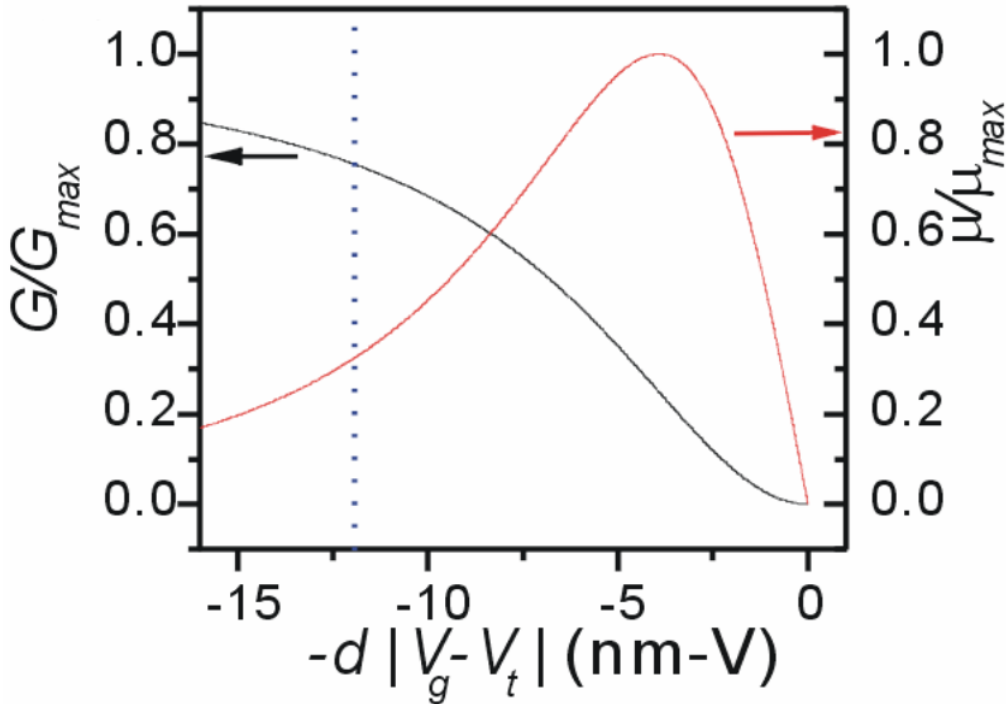


Figure 3.7: Theoretical plot of SWNT FET conductance and mobility as functions of gate voltage according to Eqs. 3.27 and 3.30. The dotted line indicates where the Fermi level reaches the second subband at zero temperature.

Besides conductance, people typically characterize a conductor with a few other quantities. One of them is electron (or hole) mobility μ , which relates the electron drift v_d velocity to the applied electrical field: $\mu = v_d / E$. This quantity is, typically, a function of the Fermi energy in microscopic semiconductors. In microscopic two dimensional and one-dimensional semiconductors the Fermi level can be drastically changed by external gates. A quantity called field effect mobility can be defined as

$$\mu_{FE} = \frac{L}{C_g} \frac{dG}{dV_g}. \quad (3.28)$$

From Eq. 3.27, the field effect mobility of a nanotube is

$$\mu_{FE} = \frac{L}{C_g} \frac{dG}{dV_g} = \frac{3\pi e d l_0}{h} \frac{Vg/a}{\left(1 + (Vg/a)^2\right)^2}. \quad (3.29)$$

The factor, $3\pi e d l_0/h$, can be related to the effective mass at the bottom of the first subband as derived in Section 3.2: $m^* = h/3\pi d v_0$. Then the formula can be rewritten as

$$\mu_{FE} = \frac{e\tau_0}{m^*} \frac{Vg/a}{\left(1 + (Vg/a)^2\right)^2}. \quad (3.30)$$

It is clear that μ_{FE} is a sensitive function of gate voltage V_g . When gate voltage is barely above the threshold, the relaxation time of electrons (or holes) and their velocity increase dramatically. At very high gate voltage, the Fermi level is in the linear dispersion regime where the conductance is not changing anymore even though more electrons are being added into nanotubes. This causes the field effect mobility to decay to zero. There is a maximum point in between. Its position can be extracted from Eq. 3.30 with some simple algebra. When $V_g = a/\sqrt{3}$, the maximum mobility is

$$\mu_{peak} = \frac{3\sqrt{3}}{16} \frac{e\tau_0}{m^*} \approx 0.32 \frac{e\tau_0}{m^*}. \quad (3.31)$$

Section 3.3 also tells us that in the diffusive regime, the relaxation time and the mean free path, depends on temperature as well as diameter. From Eq. 3.16 we can write

$$\tau_0^{-1} = \alpha \frac{T}{d}, \quad (3.32)$$

where α is a proportional factor. When Eqs. 3.27, 3.31 and 3.32 are combined, the maximum conductance and peak mobility for a nanotube with diameter d at temperature T is

$$\mu_{peak} = 0.48 \frac{ev_0}{h\alpha} \frac{d^2}{T}; \quad G_{max} = \frac{4e^2v_0}{h\alpha L} \frac{d}{T}. \quad (3.33)$$

In conclusion, in the previous three sections, a model based on the relaxation time approximation is derived for electron-phonon scattering in nanotubes in the diffusive regime. It gives predictions on how conductance and mobility change in nanotube with respect to the Fermi level/gate voltage. These results will be compared with experimental data in Section 3.5.

3.5 Comparing data with theory

The experimental observations in Section 3.1 agree with the theory predictions of Section 3.4, at least qualitatively. On single device level, the measured conductance as a function of gate voltage in Fig. 3.2 looks quite similar to the theoretical plot in Fig 3.7. On the ensemble level, Fig. 3.4 shows that both resistivity and mobility of nanotubes depend strongly on diameter, but in different ways: $1/R_{on} \sim d$ and $\mu \sim d^2$. This agrees with Eq. 3.33. The observed linear temperature dependence of resistivity and μ^{-1} is also predicted by the same equation.

To be more quantitative, from the data in Fig. 3.2 we can extract values for the coefficient α from either the maximum conductance or the peak mobility: $\alpha = 9.2 \text{ mK}^{-1}\text{s}^{-1}$ and $\alpha = 12 \text{ mK}^{-1}\text{s}^{-1}$. A group at University of Maryland (Pennington and Goldsman 2003) obtained a value of $\alpha \approx 6.5 \text{ mK}^{-1}\text{s}^{-1}$ for the total scattering rate in their theory calculations. More recently, using Monte Carlo simulation, an IBM group (Perebeinos et al. 2005) obtained nearly identical function forms to Eq. 3.33 but with a smaller value $\alpha \approx 1.6 \text{ mK}^{-1}$

Å^{-1} . In general, theory calculations predict better conductance and mobility in nanotubes than what are observed in this experiment and in a recent experiment from a Columbia group (Purewal et al. 2007). The origin of this discrepancy may come from the lack of knowledge of the deformation potential D value. In a recent study, a theory paper (Pennington et al. 2007) fitted the data in Fig. 3.2-3.4 and found out the best value for D is 14 eV, which is close to the value in graphene (16 eV).

In conclusion, SWNT FETs were studied in the diffusive regime in this chapter. The on-state conductance increases linearly with the tube diameter d , and the peak mobility grows as d^2 . Both quantities grow linearly with T^{-1} . These observations are in good agreement with the predictions for scattering by low-energy phonons coupled with the 1D “relativistic” band structure. These results set the ultimate performance limits of SWNT transistors operating in the diffusive regime.

CHAPTER 4

INTRODUCTION TO CELL MEMBRANES

From this point on, this thesis will focus on biology inspired researches. Biology may well be the most rewarding research area of this century. Unlike physics, where people can understand most phenomena based on a few fundamental principles and logical reasoning, biology, at least as of today, seems more complicated and is without a grand theory. This is because in biology everything is correlated to a certain level and ‘a single particle’ view is not feasible. Life is more complex than anything human beings have ever designed, such as computers, rockets and photolithography steppers.

Modern biology was studied mostly from the chemistry perspective in the beginning. But physics is needed to understand many phenomena in life. For example, normally the most essential knowledge about a molecule is its chemical formula. But because many biomolecules are large in size, their conformations, which are strongly tied together with their functionalities, are governed by physics laws. Another example is physics laws also describe how biomolecules move around. Physicists also provide new tools/instruments to expand biologists’ experimental capabilities, such as better visualization of molecule structures or sorting cells/molecules. That is why biophysics has emerged as an active research area.

Chapter 5 will describe our research on integrating nanotubes with cell membranes. Since cell membranes have many unique properties that are not well known to the physics community, this chapter is dedicated to a brief introduction on membranes. The physical and chemical properties of the basic components of cell membranes, lipids and membrane proteins, will be discussed. The motivation and advantages of forming artificial membranes will also be provided together with some experimental techniques.

4.1 Lipids and membrane proteins form cell membranes

Figure 4.1 illustrates a patch of cell membrane based on the Mosaic model. Cell membranes are mostly made of two major components: lipids and membrane proteins. In the Mosaic model, the lipid bilayer makes up the backbone of the membrane, where proteins are sparsely distributed and free to diffuse. Not surprisingly, this early-established simple model did not capture many essential properties of cell membranes. The weight percentage of membrane proteins in cell membranes, it turns out, is significant and the protein mobilities are controlled by the cells in a way yet to be understood. However since this thesis deal with simple model membrane systems, most discussions will be on the level of this Mosaic model. A few of the most important properties of lipids and membrane proteins will be introduced in this section.

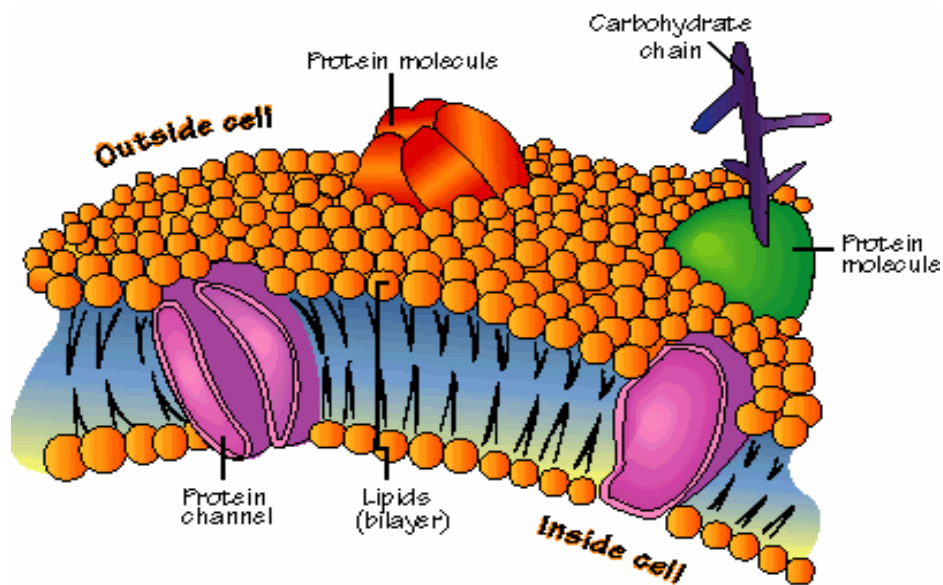


Figure 4.1: Schematic of a patch of cell membrane (library.thinkquest.org).

Lipids, one type of amphiphilic molecules

Most salts (ionic crystals) can dissolve in water. But for other small molecules that are made of a few atoms, some of them can dissolve in water while others cannot. Water is a polar solvent due to its intrinsic electrical dipoles. Just like in human society where people like to spend time with friends of similar characteristics, polar molecules are soluble in water while non-polar molecules are not. Hydrophilic and hydrophobic are used to categorize molecules into two flavors.

However, there is another category. When molecules become large, they can have segments that have intrinsic dipoles or charges while other segments that do not. Figure 4.2 shows a molecule, commonly used in detergents, called sodium dodecyl sulfate (SDS). The head group around the sulfur atom becomes ionic in water solution, and is thus hydrophilic. Each line in the zigzag part denotes an individual $-CH_2$ group. Since the bonding electrons in $-CH_2$ groups have similar affinity to both carbon atom and hydrogen atom, this part is non-polar. The zigzag part can be considered as a hydrophobic tail group. SDS belongs to a group of so-called amphiphilic molecules. The head group does not have to be ionic like in the case of SDS, an intrinsic dipole is enough to interact strongly with water. Figure 4.3 shows a lipid molecule, called 1,2-Dioleoyl-*sn*-Glycero-3-Phosphocholine (DOPC), that has a dipole in the head group. It should also be noted that DOPC has two hydrocarbon chains instead of one. DOPC will be of great interest in Chapter 5.

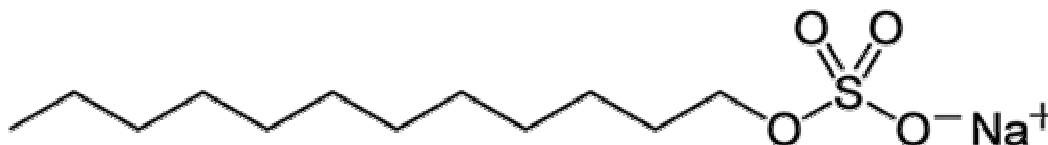


Figure 4.2: Structure of SDS molecule (Wikipedia).

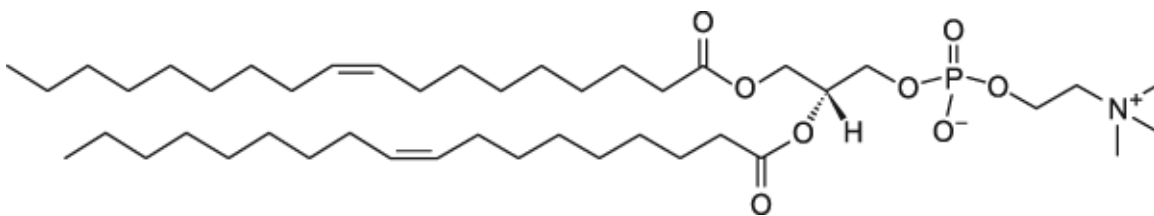


Figure 4.3: Structure of DOPC molecule (Avanti Polar Lipids).

Assembly of amphiphilic molecules

Amphiphilic molecules may dissolve both in water and non-polar solvents, e.g. oil. However their conformations could be different in different solvents. When the concentration is not too low, they can assemble into many interesting structures.

When one SDS is put into a bucket of water, the hydrophobic tail group cuts the hydrogen bond network of the water molecules. In other words, a surface energy must be paid. The interfacial free energy of saturated hydrocarbon water interface is about 50 mJm^{-2} (Israelachvili 1991). This value is smaller when unsaturated C=C bonds are present. When two SDS molecules are put into solution, they would like to have the tail groups next to each other so that the total surface area is reduced. However, entropy keeps them away. When the SDS concentration reaches above a threshold level, they can finally assemble into the micelle structure shown in Fig. 4.4. In micelles, the hydrophobic tail groups of SDS are wrapped inside the hydrophilic head groups to keep them away from the water. Thus it is in an energetically favorable configuration. Amphiphilic molecules can be used as surfactants. For example, SDS is used to wrap around nanotubes to disperse them in water solution (O'Connell et al. 2002).

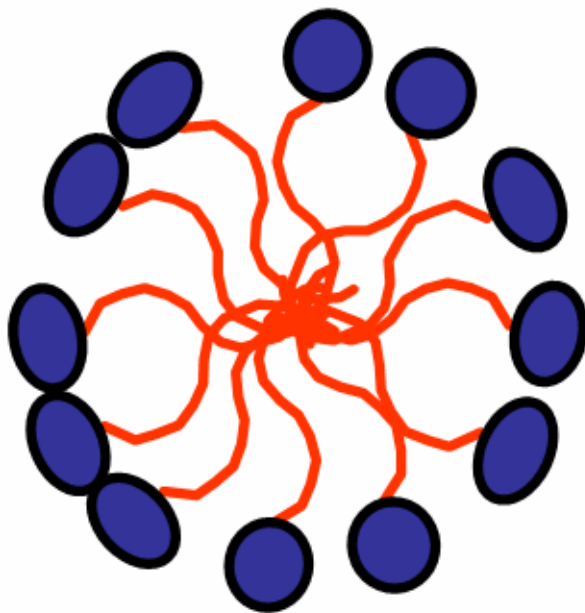


Figure 4.4: Schematic of a micelle structure (answers.com).

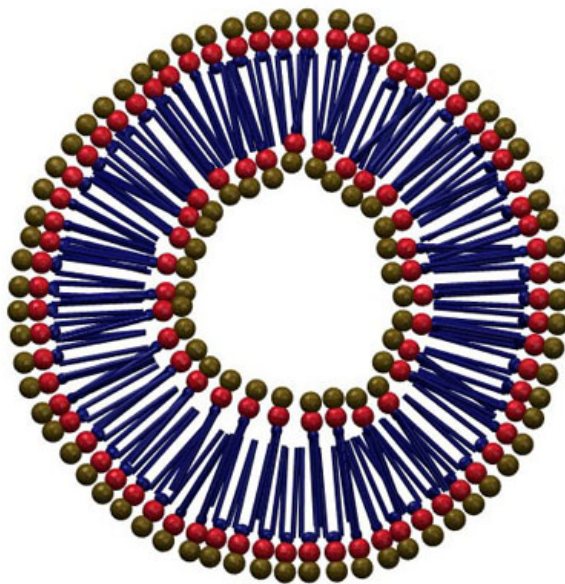


Figure 4.5: Schematic of a bilayer vesicle structure (Barrett group, McGill University).

When many DOPC molecules are dissolved in solutions, they form a different structure as shown in Fig. 4.5. The DOPCs assemble in a tail-to-tail bilayer fashion and form vesicles with a cavity inside. This lipid bilayer structure already looks like a cell membrane.

The self assembly is determined by interactions between the amphiphilic molecules and the water. Apparently there is a repulsive force between the polar head groups. The force between tail groups is attractive due to Van der Waal interaction and hydrophobic effects in water. To make a stable structure, the areas occupied by the head group and tail group will be at values where the total free energy is minimized. These two values do not have to be the same.

When all the complicated forces are put aside, phenomenologically, the shape of the self-assembled structure is governed by a dimensionless geometric factor called the packing parameter: $p = V/(a \times l_c)$, where a is the head group area, V is the volume of the hydrocarbon tail group and l_c is the critical length of the hydrocarbon chain. l_c is the maximum length the chain can extend while still being fluid, and is on the same order as, but smaller than, the fully extended length. When p is less than $1/3$ as in the case of SDS, individual amphiphilic molecule is in the shape of a cone and they will form micelles. When p is larger than $1/3$ but smaller than 1 as in the case of DOPC, the molecules are analogous to truncated cones and they form either cylindrical micelles or bilayer vesicles. When p is around 1 , the molecules are in the shape of a cylinder and they form planar bilayers (Israelachvili 1991).

This packing parameter is not strictly an intrinsic property to the amphiphilic molecules. The solvent, water in this case, plays the important role. The strength of the electrostatic repulsion between head groups is mediated by ions in the water solution. For example, SDSs form micelles in low salt buffer. But when the ionic strength is increased, the head group would like to stay closer and the effective area would decrease. That makes the packing parameter go larger than $1/3$ and they start to form cylindrical micelles.

Along the same line, introducing divalent ions like Ca^+ , which can be shared as counterions by adjacent head groups, can also reduce the repulsion between head groups and increase the packing parameter p .

Besides electrostatic effects, temperature can also change the optimal structure for a given system. This effect is more subtle and difficult to predict. In general temperature can modify the packing properties of the hydrocarbon chains. Increasing temperature can make the hydrocarbon chain more mobile and reduce l_c .

Another interesting method to change the self-assembly properties is by introducing lipid mixtures. When two lipids are mixed together, assuming they do not phase separate into different regions, each of them can still be described by its own packing parameter. When one type of molecules with $p < 1/3$ is mixed with another type with $1/2 < p < 1$ at the right condition, they may form cylindrical micelles.

Permeability of lipid bilayers

Lipid bilayers are the central theme of this chapter. Mother Nature uses lipid bilayers to form the backbone of cell membranes. Unlike rock solid walls, cell membranes need to be permeable to certain molecules because cells need to get their food from and send out their wastes to the outside world. Cells in multiple cellular organisms need to communicate with others to coordinate their behaviors. The job of cell membranes is to successfully control the traffic of various molecules and conduct signals into and out of cells.

When there is a concentration difference of a certain molecule across a bilayer, the molecules will try to permeate through the bilayer to equilibrate the concentrations on the two sides. The permeability P , defined as $P = j/\Delta c$ where Δc is the concentration difference and j is the flux density, is obviously molecule dependent. A similar

permeability will be discussed in Chapter 5 to characterize the lateral diffusion and diffusion hindrance of lipids and proteins inside lipid bilayers.

Let us first ponder on how molecules can go through a bilayer membrane. They first need to leave the aqueous solution to enter the hydrophobic zone in the middle of the bilayer. Then they need to diffuse through this zone and come out on the other side. The first quantity that influences P is how much the molecule prefers the hydrophobic oily environment compared to water. This is quantified by a parameter called the partition coefficient B . Suppose a test tube is filled with water and a hydrophobic solvent such as octanol. When a small amount of these molecules is added into the test tube, after complete mixing, the ratio between the molecular concentrations in the hydrophobic solvent and in the water equals the dimensionless partition coefficient B . Besides that, P is also proportional to how fast the molecules can move around in the hydrophobic zone. In short, P is proportional to $B \times D$ with D being the diffusion coefficient in oil for each specific molecule. This has been verified experimentally in the 1980s by the Finkelstein group (Orbach and Finkelstein 1980). Figure 4.6 is the original plot in their publication. Although the ten different molecules have quite distinct permeabilities, they all fall onto a line that shows the proportionality between P and $B \times D$. In general, small gas molecules and hydrophobic molecules have a high permeability. Even small polar molecules like water and ethanol can penetrate the membrane. But large polar molecules, such as glucose, and charged molecules of any size, such as Na^+ , cannot.

This tells us that cell membranes cannot be made of lipid bilayers only. Cells will starve to death because food cannot go through the bilayers in this passive transport mode. Luckily nature designs cell membranes with many proteins that sit in the bilayer to facilitate transport of molecules with or without the cost of energy consumption.

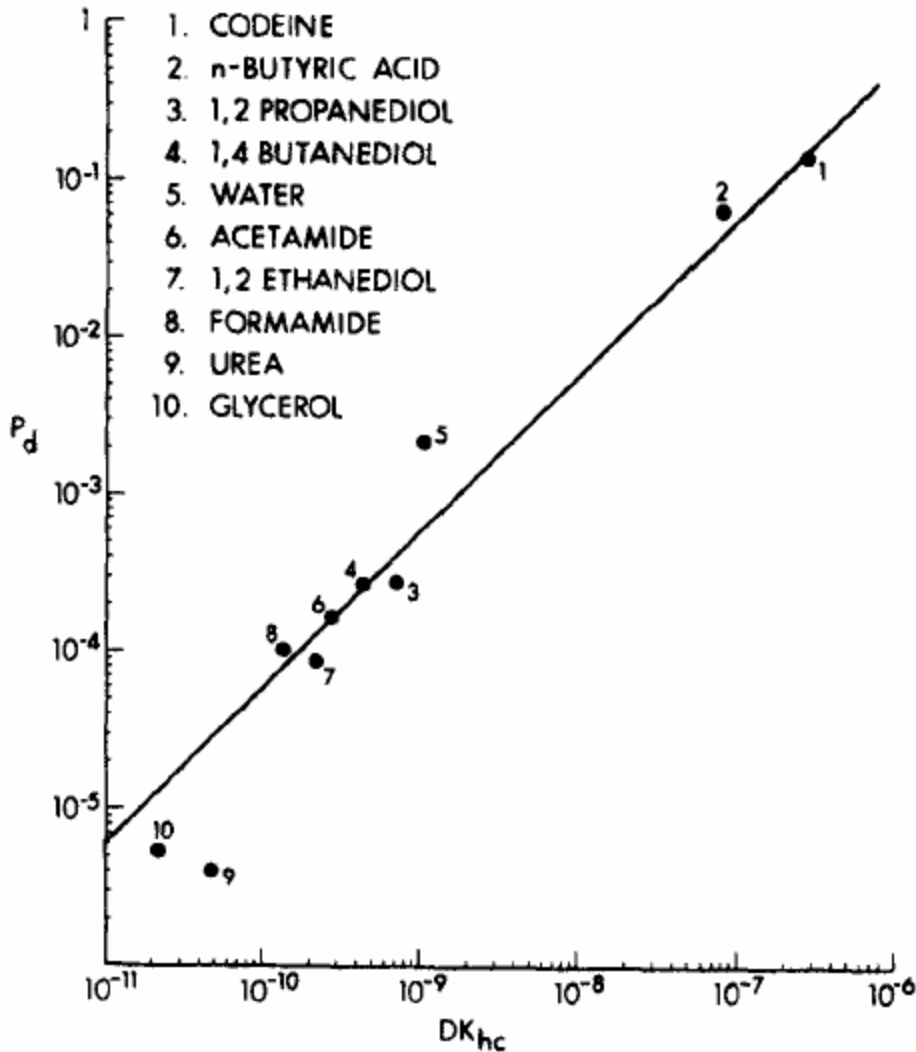


Figure 4.6: Permeability as a function of B times D (Orbach and Finkelstein 1980).

Membrane proteins

Membrane proteins can be categorized by the way they associate with lipid bilayers. A transmembrane protein, one that spans the whole lipid bilayer, has both hydrophilic region and hydrophobic region. The end result is part of the protein likes to sit inside the bilayer while others want to be immersed in aqueous solution. This type of

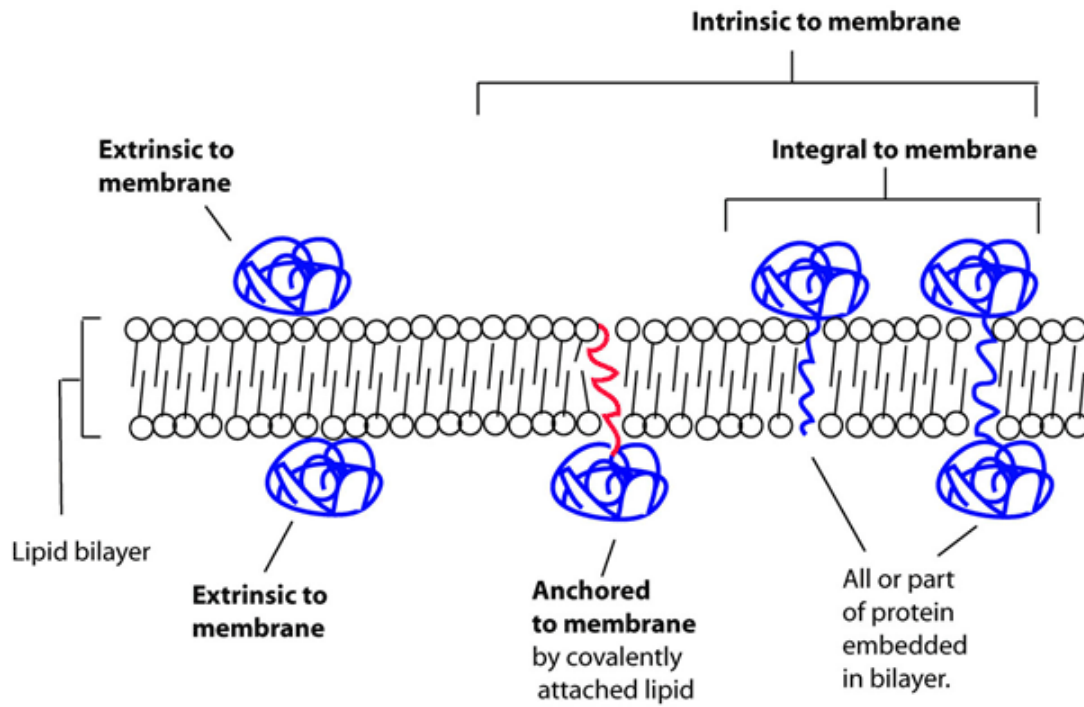


Figure 4.7: Different types of membrane proteins (www.geneontology.org).



Figure 4.8: Two examples of transmembrane proteins: potassium channel (**left**) (www.steve.gb.com) and hemolysine (**right**) (molbiol.ru).

proteins is shown on the right side of Fig. 4.7. Another type of proteins anchors to membranes by making covalent bonds with the lipids, shown in the middle of Fig. 4.7, and they are called integral proteins. The last type attaches to other molecules in the membrane by weak electrostatic, hydrophobic and other non-covalent interactions and can be release from the membrane; these are called peripheral proteins.

Obviously, only transmembrane proteins are capable of transporting molecules across the bilayers. There is a whole zoo of transmembrane proteins. One of the brightest stars is the potassium ion channel shown on the left side of Fig. 4.8. The structure of the potassium ion channel was determined with protein crystallography by Prof. MacKinnon of Rockefeller University (Doyle et al. 1998), which won him the 2003 Nobel Prize in Chemistry. Another one in current spotlight is α -hemolysine (Mathe et al. 2005), as shown on the right side of Fig 4.8, which can let single strand DNAs go through membranes. The holes in the transmembrane proteins that allow molecules to pass through are visible in this figure. The difference between the two types of proteins shown in Fig. 4.8 is that the potassium ion channel can be gated to be either open or closed while α -hemolysine has just a passive opening. Artificial nanometer scale solid state pores have recently been fabricated (Dekker 2007) to simulate α -hemolysine. They show promise for several applications including DNA sequencing.

The purpose of other types of membrane proteins will not be discussed. But an important fact about membrane proteins is that transporting molecules is not their sole job. They do not necessarily have holes as potassium ion channel and α -hemolysine. Membrane proteins can also conduct signals in other ways. For example, when a compound binds to part of a transmembrane protein on one side of the membrane, it can generate conformational changes in the transmembrane proteins to trigger a series of chemical events on the other side of the membrane. This example also indicates that the functions of these proteins are regulated by many methods, including ligand binding in this case and electrical potential in other cases.

Transmembrane proteins are hard to study because they require bilayers to keep their correct conformations, and many of them do not dissolve in water (thus are hard to crystallize). That is why their structures were determined much later compared to other proteins. This also makes people interested in forming artificial bilayers to provide playgrounds for membrane proteins, which will be discussed in Section 4.2.

Diffusion in membranes

One important property of lipids and membrane proteins in cell membranes can be seen from one experiment. Figure 4.9 is a schematic of a well known experiment in 1970 (Frye and Edidin 1970) in which human cell and mouse cell were fused together and the human/mouse proteins mixed on the surface of the new entity (Yes, crazy biologist!). It proves that membrane proteins, lipids as well, are not static. Instead, they are moving around laterally in cell membranes

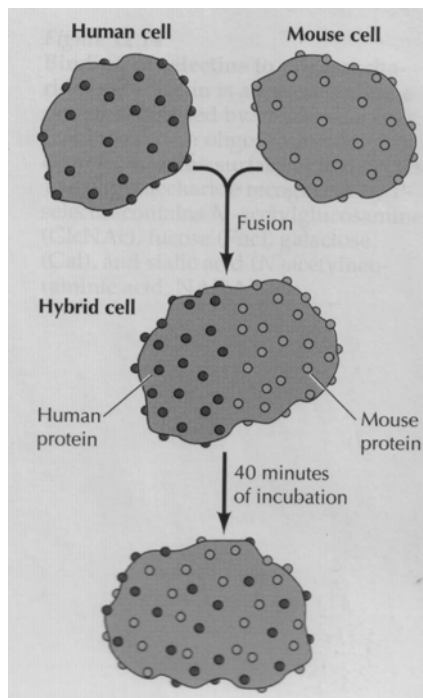


Figure 4.9: Schematic of the cell fusion experiment (Frye and Edidin 1970). The membrane proteins from the two cells mixed uniformly within an hour.

The lateral diffusion of lipids and protein in the membrane is an important process yet to be fully understood. To the first order, it can be modeled as two-dimensional random walk. The mean square displacement in a two-dimensional diffusion increases linearly with time : $\langle(x_N)^2\rangle = 4Dt$, where D is the diffusion constant.

Lipid diffusion is simpler than protein diffusion due to their small size, and it follows the random walk model most of the time. The typical lipid diffusion coefficients are around $\sim\mu\text{m}^2/\text{s}$. But there are exceptions. Each lipid species has a characteristic transition temperature. Below it interactions between the lipid tail groups are so strong that the lipids are tied together in a gel fashion. This makes the diffusion limited. When lipids with different transition temperature are mixed, they may phase separate out making so-called lipid rafts. The lipid raft model (Brown and London 1998) is proposed to describe the phenomenon where a mixture of different lipids/proteins are effectively bundled up and diffuse together.

Membrane proteins can diffuse quickly in random walk fashion in artificial lipid layers. In real cells, however, the behaviors of membrane proteins typically cannot fit with the random walk model. Their diffusion coefficients can vary drastically. Cells have the ability to confine them to certain spots on the membrane. This will be discussed further in Chapter 5.

Lipid bilayer fusions

Another noticeable process in the experiment illustrated in Fig. 4.9 is that cells can fuse. In general when two lipid bilayer vesicles are put against each other at the right condition, they can integrate into one. These fusions are typically facilitated by membrane proteins in real life.

Lipid bilayers fusion happens so often that it is used as another mechanism for molecule and signal transports across membranes, through a process called exocytosis.

One example, the complex synapse process, is shown in Fig. 4.10. For the purpose of this section, one only needs to focus on how neurotransmitters, the green triangles in Fig. 4.9, are excreted out via vesicle fusion with the cell membrane. These neurotransmitters are initially wrapped inside synaptic bilayer vesicles floating in the cytoplasm of the nerve terminal. When these vesicles fuse with the cell membrane of the neuron, neurotransmitters are exposed and released to the synaptic junction. The event is propagated to the cell on the bottom when the neurotransmitters bind to the receptors on its membrane. Exocytosis exists in cells other than neurons too, and is widely used to dump waste or signaling molecules.

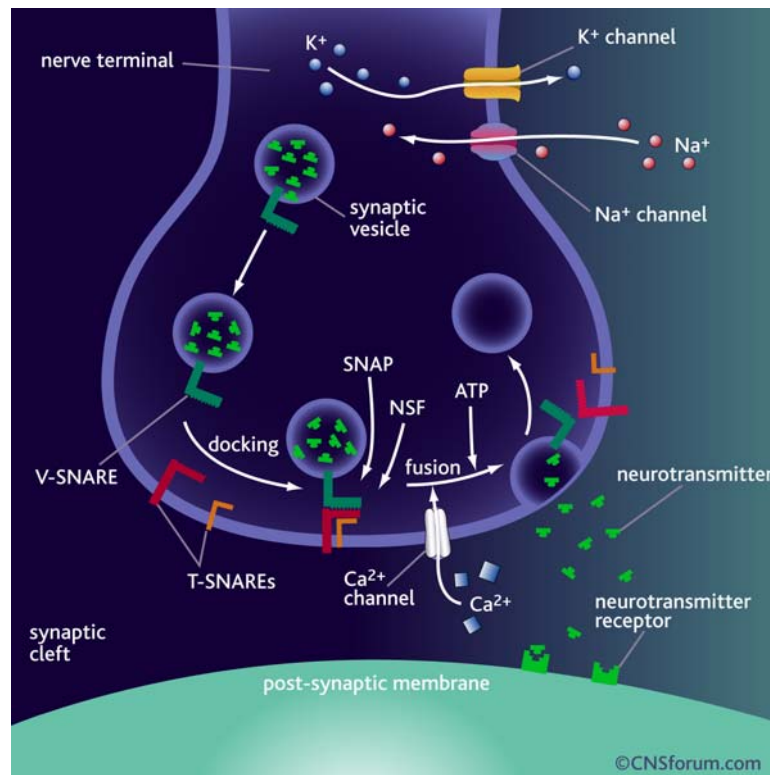


Figure 4.10: Schematic of synapse processes that require lipid bilayer fusions (CNSforum.com).

In summary, this section presents a few characteristics of cell membranes and their components. An important method to study these properties is going to be introduced in the next section.

4.2 Artificial lipid bilayers

Real cell membranes are not easy to study. For example, a popular yet notoriously hard method used to study the transport behavior of ion channels is patch clamp method (Hamill et al. 1981). It requires using a micrometer sized pipette tip to make a well-sealed contact to a small patch of fragile membrane without breaking it. It is not easy to keep cells healthy and happy, especially for physicists.

As in most biology experiments, fluorescence microscopy is used as a powerful tool to study cell membranes. But sometimes it is difficult to eliminate the background light coming from the cell bodies. For example, the imaging is very challenging when fluorescence microscopy is used to visualize the processes happening at the cell-cell junctions.

Most importantly, cell membranes are complex systems, typically composed of many types of lipids and a large number of proteins of different purposes. This makes it very difficult to study the properties of a single component.

This is why people invented a few model membrane systems using lipid bilayers. These membrane mimics have various experimental advantages while capturing the essence of cell membrane. The artificial membranes are typically stable and can be used with many sophisticated imaging and electrically techniques. It is much easier to study single protein or process one by one with model membranes since their compositions are well controlled. Artificial membranes can be integrated with other organic and inorganic structures and could produce many medical applications, besides their significance in scientific research.

Here, a few types of artificial lipid bilayers will be discussed. They each have their own merits and drawbacks.

Suspended lipid bilayer

One way to form a small area lipid bilayer is by using sable hair brush to paint lipids (Akeson et al. 1999; Bernards et al. 2006) on a small aperture that connects two chambers. After the chambers are filled with buffer solution, a fine brush is used to put a small droplet of organic solvent with lipid molecules onto the aperture. After the solvent evaporates, a suspended lipid bilayer, sometimes called black membrane, is assembled across the aperture. Figure 4.11 shows the apparatus and resulting lipid bilayer. The formation of the bilayer is monitored by measuring the junction resistance and capacitance.

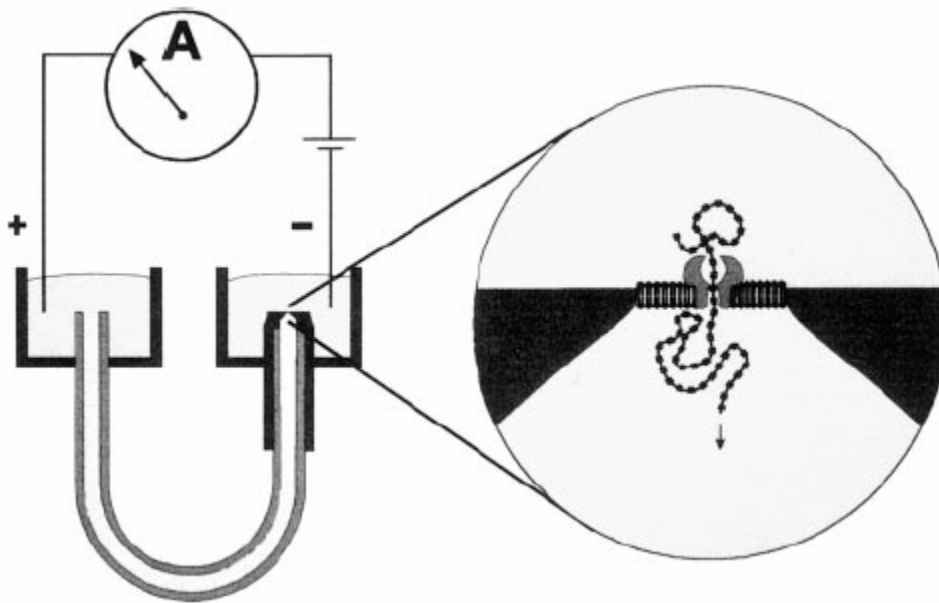


Figure 4.11: One example of suspended lipid bilayers (Akeson et al. 1999).

Another way to form a suspended lipid bilayer in this same two-chamber configuration can be done without using brushes. First, one of the two chambers is filled with oil and the other with water. When lipids are put into water, they will form a monolayer at the aperture between water and oil to reduce the surface energy. This aqueous lipid solution can then be introduced into the oil chamber to gradually replace all the oil. Once the water oil interface reaches the aperture, another monolayer will form against the original one to make a bilayer.

Suspended model membranes provide an excellent system to study transport processes through bilayers. For example, α -hemolysine can be inserted to a patch of suspended membrane and DNA translocation through the protein can be studied by monitoring the reduction in conduction through the protein pore (Mathe et al. 2005). The lifetime of this type of artificial membrane is on the order of hours, and is sufficiently long for most purposes. This type of model membrane does not have particular imaging advantage though.

Supported lipid bilayer

Another kind of model system that is becoming more popular is called supported lipid bilayers (SLBs), shown schematically in Fig. 4.12. It is basically a two-dimensional lipid bilayer sitting on top of a flat and hydrophilic solid substrate such as glass, mica and oxidized silicon wafers.

SLBs are typically formed through vesicle fusion and rupture. Lipid molecules first self assemble into vesicles. When a droplet of this vesicle solution is put on a flat hydrophilic substrate, the vesicles will stick to the substrate and form a two-dimensional lipid bilayer sheet (detailed experimental methods in Chapter 5). This transition process was studied carefully by the Boxer group at Stanford (Johnson et al. 2002). When a

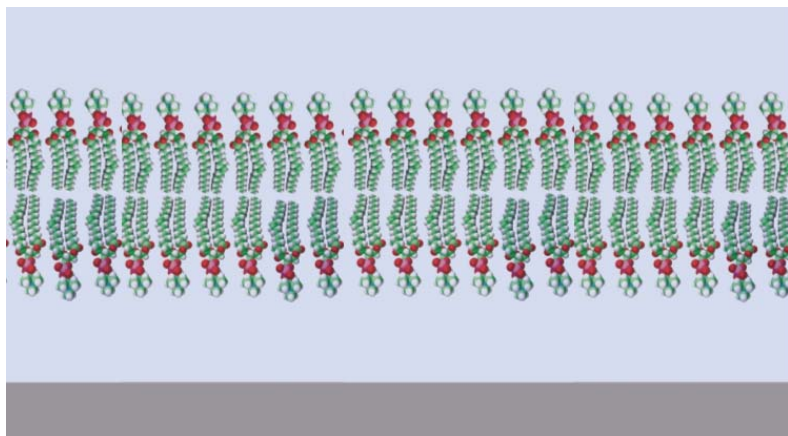


Figure 4.12: Side view of a patch of support lipid bilayer.

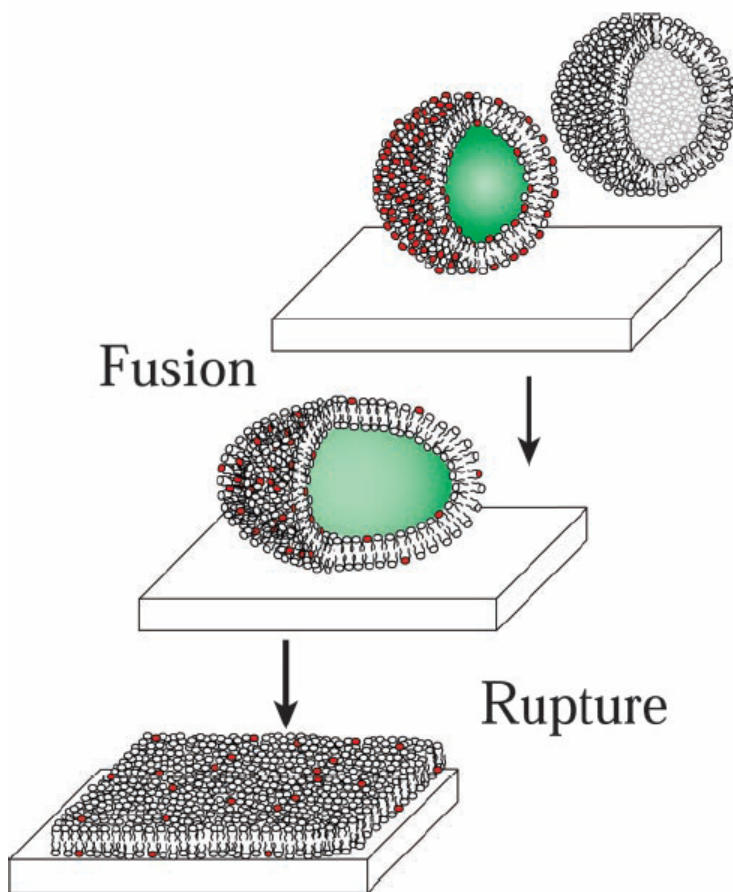


Figure 4.13: Forming SLBs via vesicle fusion and rupture (Johnson et al. 2002).

vesicle is attracted to a substrate due to interfacial forces (this is why it only works on hydrophilic substrates), another vesicle floating in the solution can fuse with the one stuck on the substrate to form an American-football shaped cylindrical vesicle. The membrane curvature is reduced in the fusion process. And eventually these bigger vesicles rupture to form planar membranes. Figure 4.13 shows this process in a pictorial way. There are other mechanisms for this transition process, but the one shown in Fig. 4.13 is the main route. This implies that the transition from vesicles into SLBs is easier with high concentration vesicle solutions since it requires interactions and fusion between multiple vesicles.

Advantages of SLBs

One of the biggest advantages of SLBs' is that they serve as a versatile imaging platform because the membrane is flat and sitting on microscope compatible substrates. For example, it is used as a model system to study membrane interactions between two cells. This is hard to do in other systems since they require sophisticated manipulation of cells and elimination of unwanted background light. The Groves group (Mossman et al. 2005) used a flat SLB and a vesicle to simulate this process. The membrane-membrane junction is easy to form in this case. Total internal reflection technique, which relies on the evanescent light waves that can only penetrate a small depth (~100 nm) into samples of interest when total internal reflections happen, is used to illuminate only a thin layer of space around the membrane junction to get rid of background noise. Another microscopy that can be used with SLBs is fluorescence interference contrast microscopy, which can be used to acquire nanometer scale height variation information. The Groves group (Parthasarathy et al. 2006) made SLBs on top of SiO₂/Si wafers. Both the excitation and fluorescence emission from the membrane interfere with the reflections from the nearby silicon surface. Therefore the intensity of the fluorescence signal is a sensitive function of

the membrane height, and is used to resolve sub-nanometer information in the direction perpendicular to the membrane.

Another advantage is that SLBs' are much more stable. Compared with suspended bilayers, the head groups of lipids in SLBs can interact with the substrates beneath. And the sealed water cushion layer between the SLB and the substrate can potentially have different ionic strength than the bulk solution. Both factors can modify the packing parameter, which, as mentioned in Section 4.1, is a function of molecule structures and environment. Effectively there should be little tension in (at least the bottom leaflet) SLBs and they are mechanically more stable.

Lastly, SLBs can be patterned. Since SLBs do not form on most metal surfaces, evaporated metal lines can serve as fences to confine SLBs. Photoresist can also be used to cut the continuity of SLBs. One example is shown in Fig. 4.14. There are other ways to do the job without putting any other material around the SLBs. The key is to make

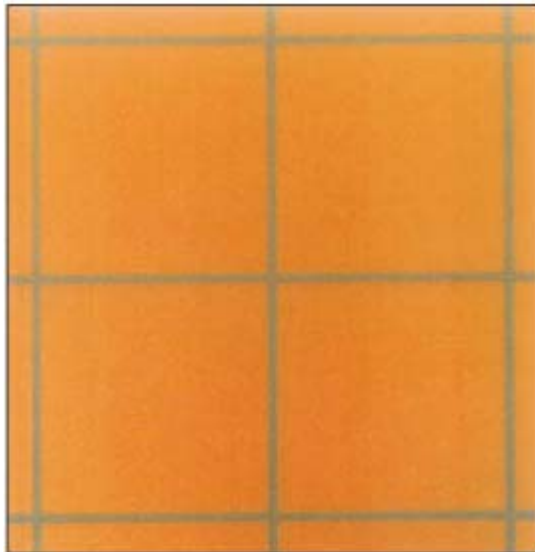


Figure 4.14: Patterned SLBs using photoresist barriers (showing as dark lines). Each box is $200\ \mu\text{m}$ by $200\ \mu\text{m}$ (Groves et al. 1997).

different regions of the substrate surface with different properties. One method (Moran-Mirabal et al. 2005) involves covering regions where SLBs are not needed with thin parylene film before the substrate is exposed to vesicle solutions. After a SLB is formed on the substrate, parylene film can be peeled off to leave SLB patches at regions of interest. With both techniques, the SLB patterns can be defined down to micrometer scale.

Lipid mobility in SLBs

One may worry that the lipid mobility in SLBs is degraded due to the presence the nearby solid substrates. But since the attractive force is small, the lipids are still diffusive in SLBs. The diffusion coefficient can be measured accurately with Fluorescence Correlation Spectroscopy (FCS) (Moran-Mirabal et al. 2005) or Fluorescence Recovery After Photobleaching (FRAP). Detailed discussions can be found in Section 5.2. It is hard to compare the lipid mobility in SLBs to that in real cells since cell membranes are made of complicated mixtures of lipid varieties and membrane proteins. However the diffusion coefficient is on the same order.

The lipids in SLBs can be manipulated with external forces. In one experiment, a charged lipid species is mixed with another neutral type in an SLB (Groves et al. 1996). They do not phase separate under normal conditions. When an in-plane electrical field is applied, however, the negatively charged lipids start to move under the influence. The distribution function is a result of the competition between the electrical potential and thermodynamic equilibration. As Fig. 4.15 shows, the negatively-charged fluorescence lipids, red in color, build up at the edges of SLB corrals opposite to the direction of the electrical field lines. In Chapter 5, we will show another example where proteins attached a SLB are manipulated by fluid flow.

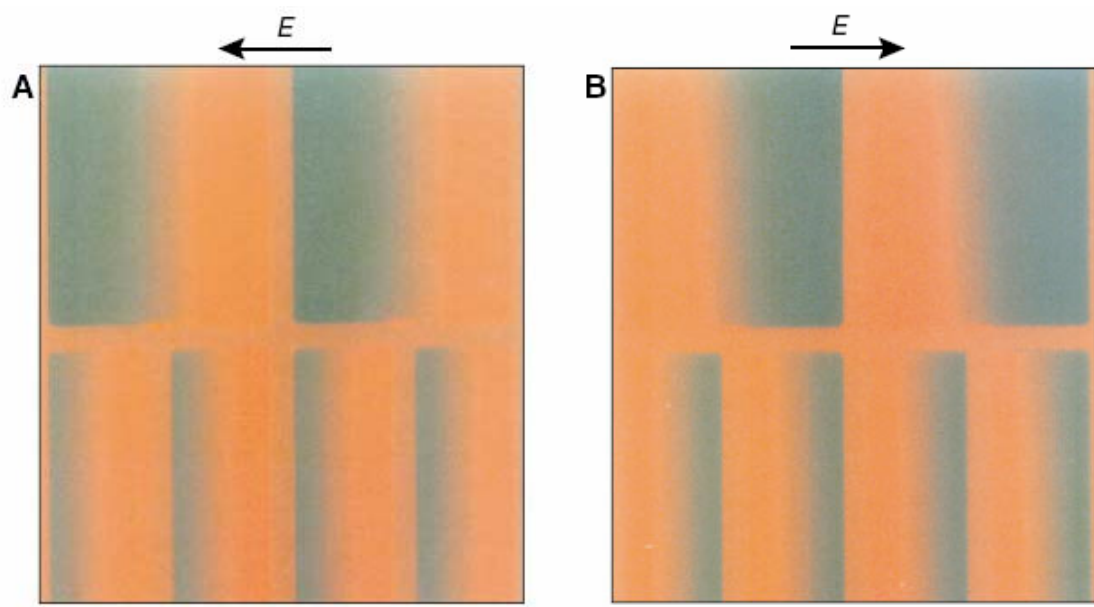


Figure 4.15: Driving charged lipid molecules in SLBs with electrical field (Groves et al. 1996).

Protein mobility and polymer supported lipid bilayer

As mentioned before, membrane proteins can be integrated into SLBs in order to study their properties. But the mobility of membrane proteins can be degraded due to their interaction with the substrates. This is because proteins are large. When part of the proteins extruding from the SLBs strongly interacts with the substrate, they will be pinned. On top of that, the protein may denature, or change their conformations in other words, to lose their normal functionalities. There are a few methods to solve this difficulty (Sackmann 1996). First, when the extruding parts are not essential to protein functions, they can be chopped off. For example, if a protein only serves as receptors to other molecules, there are only two parts needed to remain intact: the group in charge of recognition and binding and the group that anchors the protein to lipid bilayers.

In the case of other more complicated transmembrane proteins like ion channels, however, the structure cannot be altered. Then the solution to the mobility and

denaturation problems can be solved by adding a hydrated polymer cushion layer (Sackmann 1996) between the lipid bilayer and the substrate as shown in Fig. 4.16. This is actually a better mimic of cell membranes. Cells in multi-cellular organisms are surrounded by an extracellular matrix, which is essentially made of biopolymer meshes. Because of that, proteins are expected to perform their functions in polymer supported bilayers.

Experimentally it may be a little more difficult to functionalize the substrates with a flat polymer layer and then form bilayers on top. Another possible solution is to use small percentage of lipids with very large head groups when constructing the bilayer. The hope is that these lipids will act as pillars to push the bilayer further away from the substrate to prevent proteins from interacting with the substrate. As far as the author knows, this idea has not been tried or has not been successful enough to be reported.

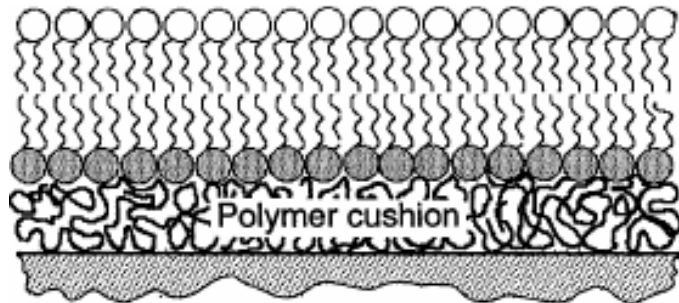


Figure 4.16: Schematic of polymer supported lipid bilayers (Sackmann 1996).

In summary, a brief introduction to amphiphilic molecules, cell membranes and lipid bilayers are given in this chapter. Artificial membranes, including SLBs, are shown to be flexible platforms to study membrane properties. This knowledge is indispensable for the experiments in the next chapter.

CHAPTER 5

SUPPORTED LIPID BILAYER/CARBON NANOTUBE HYBRID

Single-walled carbon nanotubes (McEuen 2000) (SWNTs) offer unique opportunities for chemical (Kong et al. 2000) and biological sensing (Besteman et al. 2003; Star et al. 2003). In this chapter, we will present our research on integrating SWNTs with artificial cell membranes for sensing protein binding events and studying the interaction between nanotubes and lipids/proteins.

In Sections 5.2-5.5, we show the integration of supported lipid bilayers (SLBs) (Brian and McConnell 1984; Sackmann 1996; Richard et al. 2003) with SWNT field effect transistors (FETs). We first demonstrate membrane continuity and lipid diffusion over the tube. We show that, however, the NT acts as a diffusion barrier for a membrane-bound tetanus toxin protein, and that the strength of the diffusion barrier depends on the diameter of the NT. Finally, we present results on the electrical detection of specific binding of streptavidin to biotinylated lipids.

The formation of fluidic SLBs on SWNTs will allow the study of lipid-SWNT interactions and sensing of analytes binding to specific receptors imbedded in the SLBs. These studies should have an impact on our understanding of model and biological membranes (Zhou et al. 2007).

But before the main content of the chapter, as a prelude, Section 5.1 is used to discuss why people are interested in nanotube sensors, what people have accomplished and why we chose to study cell membranes.

5.1 Prelude

Why is a nanotube an interesting component to interact with biomolecules?

In order for nanotubes to be used in any experiments with biomolecules, which require water solutions to retain their normal functions, it is critical to show that nanotubes can work in aqueous environment. This was demonstrated a few years ago (Kruger et al. 2001; Rosenblatt et al. 2002).

Figure 5.1 plots the conductance of a nanotube FET in 0.1 M NaCl solution as a function of solution potential. The detailed experimental method is explained in Section 5.2. When compared to similar curves where the Fermi level is controlled by a back gate as in Chapter 3, Fig. 5.1 shows the nanotube can be turned on much faster in solution, demonstrating the large capacitance between water and nanotubes (Rosenblatt et al. 2002).

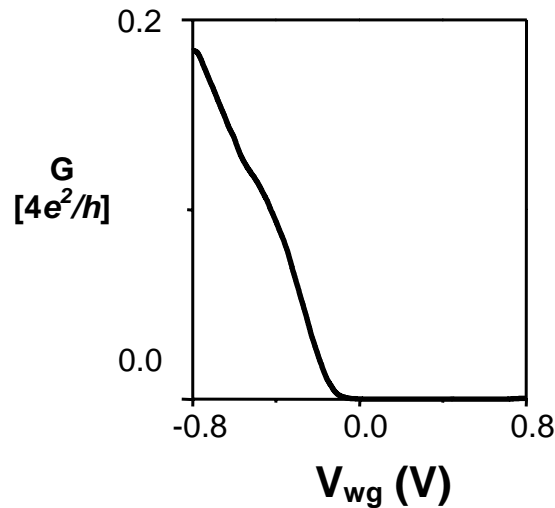


Figure 5.1: The performance of a nanotube FET in 0.1M NaCl solution.

After these studies proved the possibility of nanotubes working in salty water solutions, the first idea of integrating nanotubes with biology was the use of nanotube FETs as sensors. Since most biological molecules are charged, when they bind to a nanotube, the local electrostatic environment is altered, which may generate a conductance change in the FET. In other words, the threshold voltage of the FET is shifted. This is a general approach valid for all FETs, but using nanotubes FETs as the key element has quite a few advantages that can be summarized in four s-words:

Small. First of all, SWNTs are small, even when compared with micro biomolecules. The nominal diameter of a DNA double helix is 2 nm. SWNTs can be even smaller than that in diameter. This advantage can lead to high (even single molecule) sensitivity, high spatial resolutions and parallel operations. The high sensitivity can be very important. The concentration of macro molecules of interest is amazingly low in many cases. It would be great to have a small sensor that does not require too much analyte to get the test done.

Surface. For an electrical charge based sensing scheme, it is desirable to put the conducting channels close to the analyte in order to increase the electrostatic coupling. A nanotube is perfect in the sense that all the atoms are on the surface. Another advantage is there is only one conduction channel in nanotubes. In a typical traditional FET sensor, there are conduction channels underneath the surface that give rise to a large background noise. Having only one conduction channel on a nanotube surface can raise the sensitivity even higher.

Stable. In traditional semiconductor FETs, it is not possible to expose the electron conduction channels directly to the aqueous environment because the ions can penetrate into the FETs and ruin them. A dielectric layer is needed to isolate FETs physically from ions in the solution. That would inevitably reduce the electrostatic coupling. Since carbon nanotubes are in such a chemically inert form, they will not react with ions even when there is reasonable (less than 0.7 V) electrical potential between them, as shown in Fig.

5.1. In other words, ions and electrons in nanotubes are separated by a fence that is impenetrable at low voltage. This maximizes the electrostatic coupling and leads to high sensitivity.

Superior mobility. Besides coupling efficiency, another factor influencing the sensitivity is transconductance. It describes the amount of conductance change as a response to a doping level modulation, and is linearly proportional to the FET mobility. Under the same Fermi level modulation, signals from FETs with higher mobility are large in magnitude and more easily detected. The mobility of nanotubes, as mentioned in Chapter 3, can reach more than $15,000 \text{ cm}^2\text{V}^{-1}\text{s}^{-1}$ at room temperature (Zhou et al. 2005). This value is more than a few times larger than that of crystalline silicon. However, it could be a double-edged sword in some cases. When there is a significant contact resistance, the signal on FETs with high mobility and low resistance may be overwhelmed by noise imposed by contacts. However it is always possible to operate nanotube FETs at low doping level with the right gate voltage to make the signal coming from the sensing region stand out.

These properties of nanotube FETs result in an extraordinary sensitivity. The sensitivity is given by signal to noise ratio. In our experiments, it is possible to distinguish a threshold change as small as 2 mV at 1 KHz bandwidth (This value cannot be improved much by decreasing the bandwidth because the dominating form of noise is 1/f noise.). The capacitance between liquid solution and a nanotube is estimated and measured to be around $4 \times 10^{-10} \text{ F/m}$ (Rosenblatt et al. 2002). That means a doping change of as few as 5 electrons in a $1 \mu\text{m}$ nanotube FET can be sensed. This does not necessarily mean that a detectable signal can be generated when 5 extra ions are put close to a micrometer long nanotube FET though due to charge screening: the mobile ions in electrolyte solutions can efficiently decrease the magnitude of electrostatic interactions.

Single electron sensitivity is possible when the nanotube conduction channel length is further reduced. This unprecedented sensitivity will enable electronic-based

molecule detections to complement optical techniques currently used for the purpose. It will make huge impact in research and applications if it can be made to work effectively and reliably.

Previous biosensors made of nanotubes

The first studies using nanotubes as biosensors focused on DNA or protein detection (Besteman et al. 2003; Star et al. 2003), based on the idea discussed above. These works are important because DNA and proteins are the two most essential components of life, and have been in the spotlight of modern biology. As the central dogma of molecular biology says (Alberts et al. 2002), DNA carries the genetic information from one generation to the next while proteins, made from the blue print encoded in DNAs, perform all the functions to keep cells alive. (RNA is also needed in the transcription and translation process to produce protein molecules.) The ability to detect specific DNA sequences and proteins can generate huge clinical improvements, *e.g.* faster diagnosis and potential disease prevention.

On the other hand, in these previous studies the biomolecules were almost treated identically to any charged particles, making these projects less appealing to biologists.

Why do we choose to study cell membranes

There would be no life on Earth if there were only DNAs and proteins in the world. Without compartmentalization, entropy would put everything into thermal equilibrium and make the world featureless. It is membrane that forms playgrounds for DNA and protein to function properly. Figure 5.2 is a schematic of a cell. First of all, the cell is separated from its surroundings by its cell membrane. Even on the inside, different organelles are isolated as individual units by membranes. These membranes control the traffic of all kinds of molecules, including food, waste and signaling molecules, into and

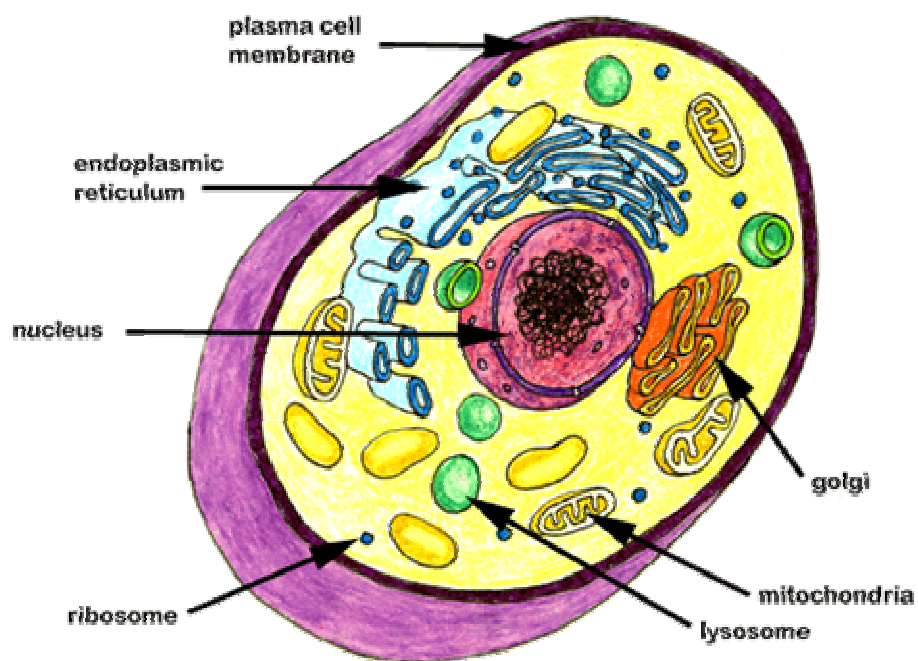


Figure 5.2: Schematic of a cell (web.jjay.cuny.edu/~acarp/NSC).

out of the cell. A cross membrane potential is also used in the photosynthesis process to store solar energy into chemical bonds, and in the metabolism to release energy from chemical bonds (Alberts et al. 2002; Nelson 2004). Membranes are indispensable units of life. That is why this part of the thesis will study membrane properties using nanotubes as a tool.

Specifically, we will work with SLBs. SLBs self-assemble from phospholipids on flat, hydrophilic substrates like glass, and mimic many properties of cell membranes. The lipids in a SLB are laterally mobile and many reconstituted membrane proteins embedded in them remain functional (Salafsky et al. 1996; Mossman et al. 2005). Although it has been shown that lipid bilayers can form on top of multi-walled carbon nanotubes (Ye et al. 2005) or SWNTs coated with polyelectrolytes (Artyukhin et al. 2005), the nanotubes

in these experiments were not used as detection elements and the bilayers were not supported on flat substrates. Another group has placed membrane patches on SWNT field effect transistors (FETs) (Bradley et al. 2005), but no continuous SLBs were formed and the measurements were carried out in dry condition. As will be shown in following sections, our research, for the first time, integrated high quality SLBs with nanotube FETs.

5.2 Forming SLBs on nanotube chips

Methods of forming and imaging SLBs

The phospholipid used for SLB formation was the zwitterionic 1,2-dioleoyl-sn-glycero-3-phosphocholine (DOPC, Avanti Polar Lipids). Small unilamellar vesicles (SUVs) were prepared as previously reported (Groves et al. 1996; Moran-Mirabal et al. 2005). Lipids were dissolved in chloroform at the appropriate molar ratios for a final concentration of 1mM, and allowed to mix. The solvent was evaporated under a dry nitrogen stream, forming a uniform lipid film. The lipids were then resuspended in either 10 mM or 1 μ M (working solution for electrical detection) PBS buffer (pH 7.4), and allowed to rehydrate. Finally, SUVs were produced by point-probe sonication at 100 Watt for about 10 minutes, yielding vesicles 50-100 nm in size. When vesicles were incubated on hydrophilic substrates above the transition temperature of the mixture, SLBs formed spontaneously via vesicle rupture and fusion.

In experiments with chips containing SWNT FETs, polydimethyl-siloxane (Ng et al. 2002) (PDMS) microfluidic channels with a typical cross section of 10 \times 50 μ m were laid on top of SWNT FETs to confine liquid solution to the area proximal to the SWNTs (Fig. 5.3a). The alignment was done manually on a home-built probe station. A low-magnification long-working distance microscope was used to keep track of the features on nanotube chips and PDMS stamps. The edges of PDMS stamps were attached to a

holder, made from two glass slides with spacing in between that were glued to another slide. The PDMS staples can be moved in three dimensions by a micromanipulator, and were laid down on facing nanotube chips once alignment was achieved.

Once the PDMS sealing was visually checked under microscopes, the holder was removed and the channel was filled with vesicle solutions. This was done by putting a droplet of vesicle solution in one of the open reservoirs, holes punched in the PDMS stamps and connected to the ends of the channels. After an incubation of about 15 minutes to allow SLBs formation, the channels were flushed many times with working buffer to remove excess vesicles. Putting chips with vesicle solutions into a hot moisture oven can help the SLBs formation if the transition temperature of the lipids is above room temperature.

To image SLBs, Lissamine-Rhodamine Red 1,2-dihexadecanoyl-sn-glycero-3-phosphoethanolamine (LR-DHPE) (Molecular Probes) fluorophores were mixed with phospholipids at 0.1% molar ratio. Images were obtained by using an upright Olympus fluorescence microscope with a thermo-electrically cooled 12 bit CCD camera (Cooke).

Nanotube device fabrication and cleaning

The SWNT FET devices (shown schematically in Fig. 5.3a) were fabricated as previously reported (Rosenblatt et al. 2002). Carbon nanotubes were grown by chemical vapor deposition on silicon wafers with 500 nm oxide capping layer³. Using photolithography, gold electrodes were defined on top of the SWNTs with 2-10 μm gaps between source and drain electrodes. The nanotube growth yield was controlled so that most transistors had one nanotube bridging the electrodes. To do better optical imaging, devices were made on 170 μm cover slips as well.

³ The oxide thickness was intentional chosen, although not precisely tuned due to vendor limitations, to make the interference between lights reflected from the oxide surface and silicon surface constructive (Parthasarathy, R. and J. T. Groves (2004). Optical techniques for imaging membrane topography. *Cell Biochemistry and Biophysics* **41**(3): 391-414.). In this way, the illumination and fluorescence intensity from fluorophores in the SLBs are maximized. We can use lower fluorophore concentration to do imaging.

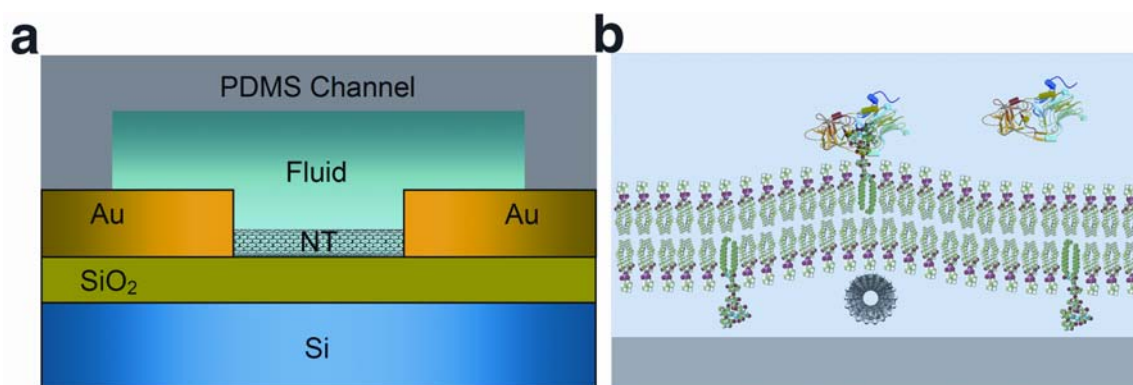


Figure 5.3: Representation of the supported lipid bilayer/carbon nanotube hybrids. **(a)** Schematic of the side view of a SWNT FET inside PDMS microfluidic channel. **(b)** Scaled schematic of a carbon nanotube under DOPC bilayer. DOPC lipid molecules are shown with two light green fatty acid chains. A toxin protein, represented in a ribbon model, binds to a membrane-embedded ganglioside molecule that is shown with two dark green chains. There is a thin water layer between SLB and substrate.

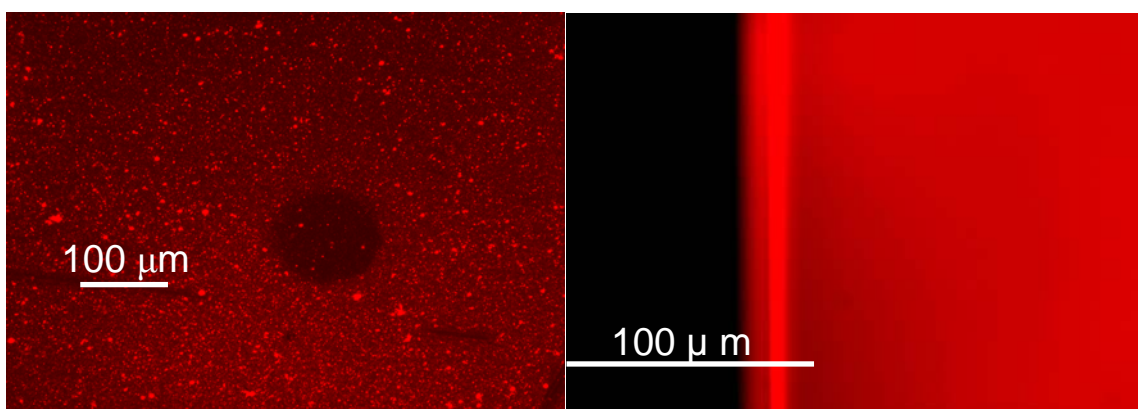


Figure 5.4: SLBs cannot form on as-made nanotube chips (**left**). Fluorescence image of high quality SLBs is shown on the right as comparison. The SLB is confined inside a microfluidic channel on the right half of this image.

In the beginning, vesicles would not fuse on chips with nanotube devices. A fluorescent image of typical initial results of attempting to form SLBs is shown on the left side of Fig. 5.4. This can be compared to the right side of Fig.5.4 that shows a fluorescence image of a continuous SLB film on a clean SiO₂/Si wafer. The only things left on nanotube chips in the left image were unfused vesicles and small patches of SLBs. Long dose of light was used to bleach fluorophores inside a small region, the result of which is the dark circle region on the left side of Fig.5.4. The fluorescence from this region stayed low for very long time, proving that there are no SLBs on large scale and the lipids are not mobile. This failure of SLBs formation is because the surface is contaminated with organic photoresists and amorphous carbon during photolithography and tube growth processes.

Wafers containing SWNT FETs were cleaned with room temperature piranha solution (volume ratio 3:1 concentrated sulfuric acid/30% hydrogen peroxide) without sonication for 3-5 minutes⁴ or in a UV-ozone cleaner for 90 seconds at 70°C to remove residual contamination from processing and render the surface hydrophilic. The cleaning procedures were developed to allow the formation of uniform, fluid SLBs, and were tested to insure that they did not degrade the SWNT FET device performance. Most devices survived the cleaning procedures and their electrical conductance did not change by more than 20%.

Confirming SLBs quality by measuring lipids diffusion coefficients

To verify the quality of SLBs on nanotube chips after cleaning, two standards were used. First, the SLBs should spread on the whole surface uniformly. This is confirmed by a uniform fluorescence as shown on the right side of Fig. 5.4 where a SLB

⁴ It has been noted that washing the chips with organic solvents, e.g. acetone and methanol, immediately before piranha cleaning can result in the lifting-off of electrodes and destroying the FETs.

was formed inside a PDMS channel⁵. Another standard is that lipids should be able to diffuse laterally within the SLBs. To test this, diffusion coefficients were measured and compared to reported values from other groups.

This can be done with two methods. One method uses fluorescence recovery after photobleaching (FRAP) technique. In these experiments fluorophores inside a circular region with radius R are photo bleached at time $t = 0$, as shown in the left panel of Fig. 5.5. The fluorescence intensity I at the center recovers as the bleached fluorophores diffuse away. The right panel of Fig. 5.5 shows a typical fluorescence recovery curve. Since we use high intensity light to bleach all the fluorophores in the circle over a small period of time, we assume all the fluorophores inside it are dead⁶ and consider the non-zero intensity as background noise. Then we can define normalized fluorescence intensity F as $F = (I - I_0)/I_\infty$, where I_0 and I_∞ are the fluorescence intensities at time 0 and at infinite time.

In the case of two-dimensional isotropic diffusion, the probability for a particle with diffusion coefficient D leaving the origin at time zero to be at distance r away from the origin at time t is

$$P(r, t) = \frac{\exp\left(-\frac{r^2}{4Dt}\right)}{4\pi Dt}. \quad (5.1)$$

The fluorescence intensity inside the circle after bleaching should grow back when the dead fluorophores diffuse away and fresh ones come in. The normalized intensity of the center should be one minus the probability of any of the dead fluorophores occupying that location

⁵ SLBs form on the channel walls of the PDMS stamps. When the fluorescence intensity was studied quantitatively as in this section and some other parts, the images were taken once the PDMS stamps were removed inside a beaker with buffer solution, leaving the SLBs on the substrates intact. Images in these cases were collected with a water immersion lens. Future experiments can use transparent substrate and total internal reflection microscopy to solve the background fluorescence issue if PDMS channels are indispensable.

⁶ This is an approximation as fluorophores are constantly diffusing in and out of the circle.

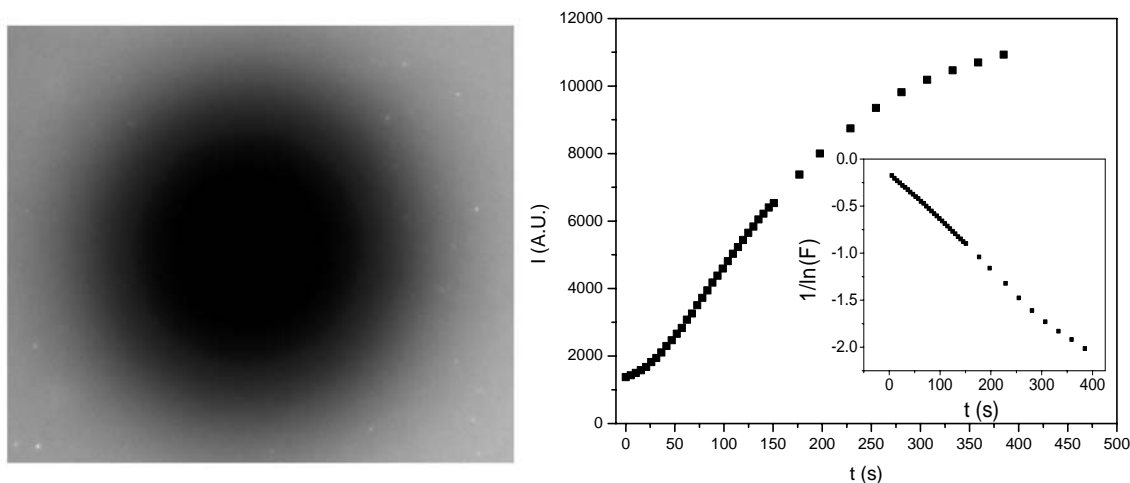


Figure 5.5: Estimation of lipid diffusion coefficient using FRAP. **Left panel:** Fluorescence image around the bleached region (dark circle in the center) at time 0. **Right panel:** Fluorescence intensity at the center of the circle recovers over time. Inset: Inverse log of the normalized fluorescence intensity plotted versus time.

$$F = 1 - \int_0^R \frac{\exp\left(-\frac{r^2}{4Dt}\right)}{4\pi Dt} 2\pi r dr = \exp\left(-\frac{R^2}{4Dt}\right). \quad (5.2)$$

By fitting the curve in the right panel of Fig. 5.5, we get $\tau \sim 2 \times 10^2$ s. Since $R \sim 50 \mu\text{m}$ in the test, the diffusion coefficient of DOPC is $D \approx 3 \times 10^{-8} \text{ cm}^2/\text{s}$. This value compares favorably with previous reports (Orth et al. 2003). This method is simple in practice because it does not require complicated apparatus and can be applied to SLBs on opaque substrates.

Another method is called fluorescence correlation microscopy (FCS). It records the fluorescence intensity of a small volume and analyzes the fluctuations due to molecule diffusion to reveal the dynamical information. In these experiments a diffraction-limited illumination volume was obtained by filling the back aperture of the objective. The illumination volume was calibrated by obtaining autocorrelation curves

from a freely diffusing molecule (Alexa488-dUTP) with known diffusion constant ($2.1 \times 10^{-6} \text{ cm}^2/\text{s}$) (Foquet et al. 2004). The calibration yielded a Gaussian excitation profile with a $1/e^2$ decay radius of 280 nm.

The curves obtained from the supported lipid bilayers were fit to the autocorrelation function (Magde et al. 1972; Magde et al. 1974; Webb 2001):

$$G(\tau) = \frac{1}{N} \left[1 + \frac{\tau}{\tau_d} \right]^{-1} \quad (5.2)$$

which models the autocorrelation of the fluctuation in fluorescence arising from the diffusion of molecules in a two dimensional plane in and out of a Gaussian illumination volume.

The detailed experimental method is as follows. FCS autocorrelation curves were acquired using a confocal fluorescence microscope in epi-illumination mode. Fluorescence was induced using a Coherent Sapphire laser (Model 488 – 02 CDRH) at 488 nm. The laser was passed through an excitation filter (Chroma Z488/10X) and a 10X beam expander (Newport Corp) to completely fill the back aperture of the objective and achieve a diffraction limited illumination profile. Fluorescence was collected through a dichroic mirror (Chroma Z488RDC) and an emission filter (Chroma AF 535/45). A coverslip corrected 60x, 1.2 NA water immersion objective was used on an Olympus IX71 microscope. Fluorescence was then coupled to an avalanche photodiode (SPCM-AQR-14-FC) via a 50 μm core fiber optic patch cord. A flex02-12D correlator card (Correlator.com) was used to calculate FCS autocorrelation curves, and a PC was then used to acquire and record the intensity trace and correlation function. A power meter was used to monitor laser power and a set of neutral density filters (Chroma) was used to maintain an incident beam power of $\sim 100 \mu\text{W}$ to minimize photo-physical effects related to non-radiative states and photo-bleaching. The nanotube devices used for FCS measurements were fabricated on 170 μm thick quartz wafers.

To obtain the diffusion coefficient of the SLB as a reference, FCS autocorrelation curves were obtained in regions where there should not be any nanotubes. Ten autocorrelation curves were obtained and averaged. The averaged curve (blue curve) along with the standard deviation from the measurements is shown in the left panel in Fig. 5.6. A fit of this curve to the model autocorrelation function (black line) yielded a diffusion coefficient $D = (5.44 \pm 0.02) \times 10^{-8} \text{ cm}^2/\text{s}$. It is easier to remember as $D = (5.44 \pm 0.02) \mu\text{m}^2/\text{s}$. And it agrees with the value measured with FRAP.

To probe the effect of the SWNT on lipid diffusion, FCS curves were obtained from lipids spanning a SWNT in an interelectrode gap (as shown the right panel of Fig. 5.6). The curves were then compared to FCS data taken from interelectrode gaps where no SWNT was present. No significant shift in the diffusion coefficient or autocorrelation curve functional form was observed between these two sets of data (Fig. 5.6, red and green curves). It is important to note that the FCS curves taken from the interelectrode gap show a longer mean residence time and a slightly different functional form than the curves taken from the reservoir. This can be attributed to the presence of reflective boundaries (electrodes) which restrict the diffusion of lipids and increase the probability that the lipids will reenter the illumination profile.

In short, the DOPC diffusion coefficient in the SLBs was measured with two different methods: one at millimeter scale and one at micrometer scale. The values from these two methods match, and agree with previously reported value. These measurements confirm the quality of the SLBs on cleaned nanotube chips.

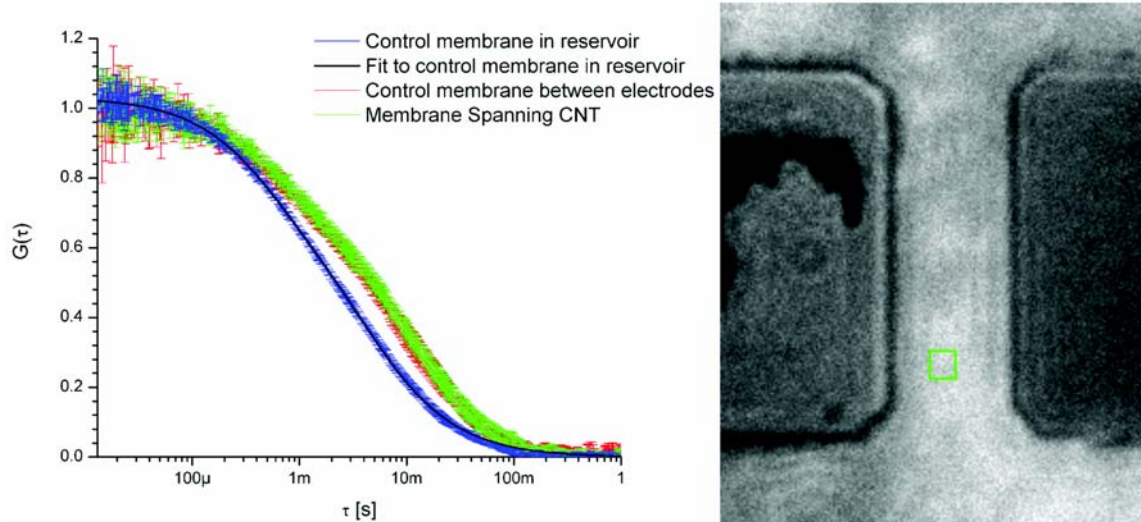


Figure 5.6: Left panel: Average normalized autocorrelation curves SLBs formed on chips containing SWNTs. Error bars represent standard deviations of at least 10 measurements. **Right panel:** Bright field image of an interelectrode gap (5 μm wide). The green box represents the area where FCS autocorrelation curves were taken from interelectrode gaps devoid of (red curve in left panel) or containing SWNTs (green curve in left panel). The location of SWNTs was measured by AFM images prior to SLB.

5.3 Probing SLBs near nanotubes

The experiments in the previous section prove the SLBs quality on large scale, but it is important to study the SLBs in the vicinity of nanotubes, which may act as perturbations in many forms.

To test the continuity and fluidity of the formed SLB over a NT, we used FRAP on devices with the geometry shown in Fig. 5.7a. We created two square SLB patches (Groves et al. 1997) connected by a 2 μm wide, 12 μm long channel. Nanotubes emerging from the black catalyst islands (visible in the optical micrograph) cross the channel. We photobleached the fluorophores in the right square and observed if the fluorescence could recover by the diffusion of fluorophores from the left box across the NT to the right box. Figures 5.7b-d show fluorescence images of the recovery process. It is shown that fluorescent lipids can diffuse across the NT. No discernible differences were observed between the FRAP recovery over a NT and control experiments with the same geometry but without NTs. A second experiment was performed to confirm that the lower leaflet of the SLB was also continuous. In this experiment, 100mM CoCl_2 was added to the buffer solution in the channel to quench the fluorescence coming from the fluorophores on the upper membrane leaflet (Ajo-Franklin et al. 2005). The FRAP experiment described above was then repeated to probe the fluorescence recovery of the lower leaflet only. The recovery speed remained the same within a 10% error. These experiments show that lipid bilayers are continuous and that lipids freely diffuse over NTs.

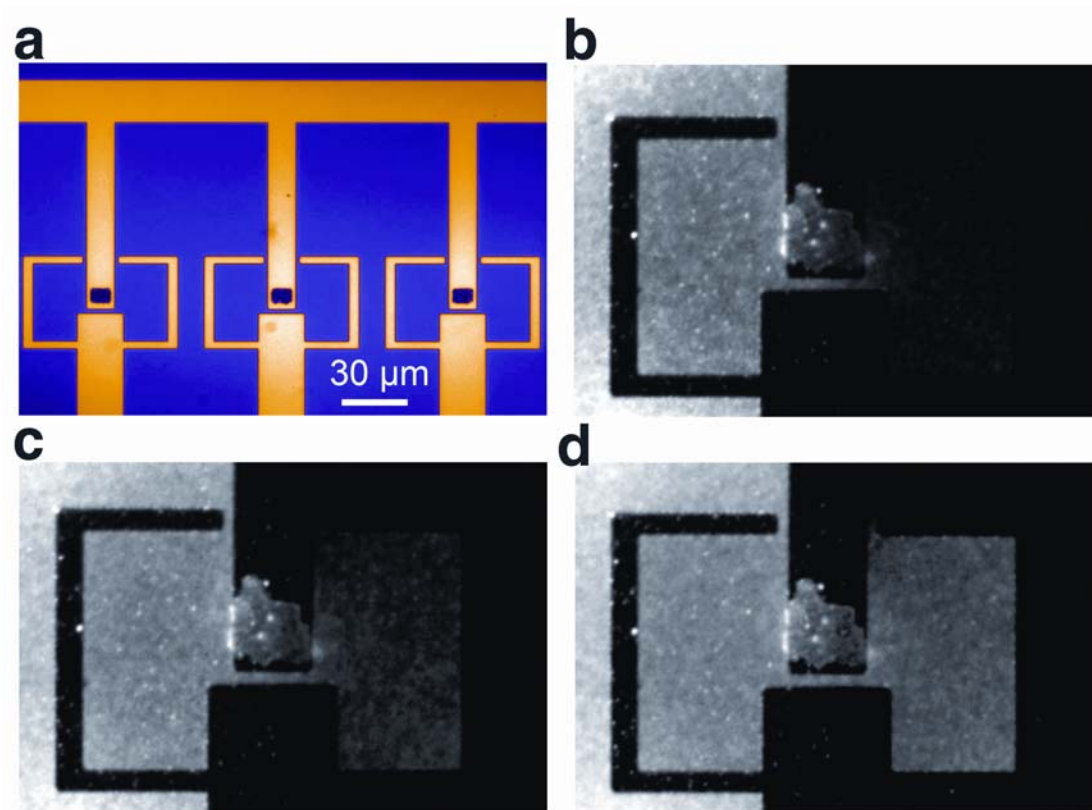


Figure 5.7: Test of lipid diffusion near SWNTs. **(a)** Optical micrograph of SWNT FET array used for diffusion tests. Two isolated regions of SLB are defined by gold electrodes and connected by a narrow channel crossed by NTs. **b-d**, Fluorescence images taken 2.5 minutes **(c)** and 10 minutes **(d)** after fluorophores on the right side were bleached **(b)**. The lipids diffuse freely across the NT.

A surprising result was seen when we examined the SLB fluorescence in the vicinity of the nanotubes. Linear features corresponding to a slight reduction ($\sim 2-7\%$) in the fluorescence intensity were observed, as shown in Fig. 5.8a. Figure 5.8b is an atomic force microscope (AFM) image showing the same region displayed in Fig. 5.8a. It is evident that the dark lines in the fluorescence image correspond to the positions of the carbon nanotubes. The results were unaffected when a polarizer was added to the light path in both parallel and perpendicular orientations with respect to the long axis of the nanotubes. For the eight tubes studied, there was no obvious correlation between the tube diameter and the magnitude of the suppression. The width of the fluorescence suppression features are approximately $0.5\ \mu\text{m}$, set by the resolution of the imaging system. If we use the simplest possible scenario and assume that the fluorophores closest to the nanotube are completely dark, the observed reduction in fluorescence would correspond to a band approximately $10-35\ \text{nm}$ wide.

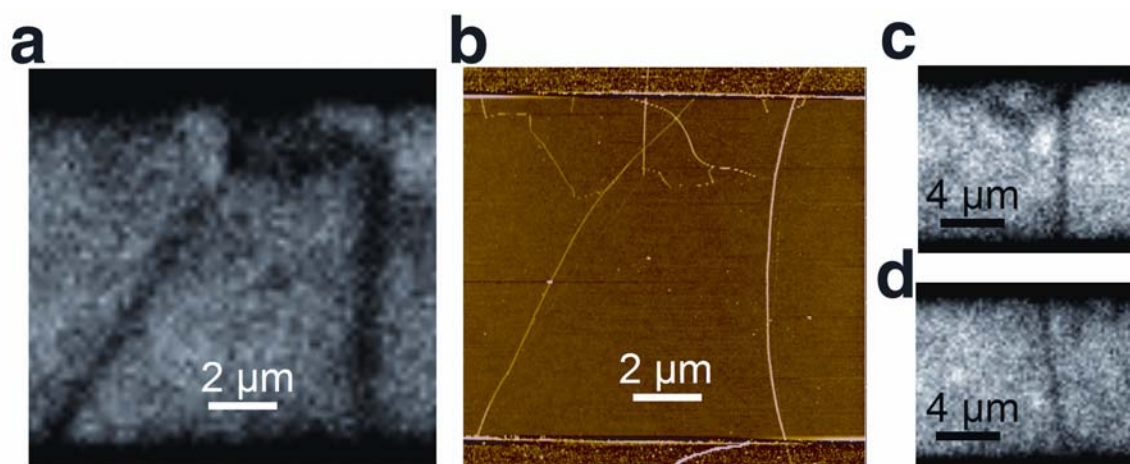


Figure 5.8: The fluorescence intensity distribution around SWNTs. (a) Fluorescence image of the gap region between electrodes of a SWNT FET. Several dark linear features were observed. (b) AFM image of the same region after SLB was removed. It is shown that the dark lines correspond to the position of the nanotubes. (c),(d) Two more fluorescence images of SWNT showing up as dark lines.

The observed fluorescence suppression at the NTs could result from many causes. An obvious explanation is that the SLB is interrupted by the NT, but this possibility is ruled out by the FRAP experiments described above. Another possibility is that the NTs quench the fluorescence of any fluorophores in their vicinity. We expect the range of quenching to be approximately $d + 2R_o$, where d is the diameter of the NT and R_o is the Förster radius (Stryer 1978). Although R_o is unknown here, typical values are ~ 5 nm, which predicts a quenched width of ~ 10 - 15 nm. This is in reasonable agreement with the magnitude of the measured signal. It is also conceivable that the local curvature induced in the SLB by the NT excludes the fluorescently labeled lipids. Such curvature-induced segregation of lipid species has been seen in previous experiments (Roux et al. 2005; van Meer 2005; Parthasarathy et al. 2006) .

5.4 Nanotubes as barriers to protein diffusion

Having established that the SLB is continuous over the NT, we address the influence of the NT on SLB-bound macromolecules. To test the diffusion of membrane-bound proteins over the NTs, we chose a simple and well-studied toxin-ganglioside couple (Angstrom et al. 1994; Moran-Mirabal et al. 2005) as model system (Fig. 5.3b). Tetanus and cholera toxins are part of a family of bacterial toxins that bind to glycolipid moieties present on the host cell's membrane as a path for infection. Tetanus toxin fragment C (TTC) binds to tri-sialoganglioside G_{T1b} , while cholera toxin subunit B (CTB) binds strongly to mono-sialoganglioside G_{M1} . The lipid mixtures used for toxin binding consisted of 99:1 DOPC: G_{M1} -BODIPY (Molecular Probes) for the cholera system, or 98.9:1:0.1 DOPC: G_{T1b} :DHPE-LR for the tetanus system. We first formed SLBs with these lipid mixtures on wafers containing NTs and performed FRAP studies of the ganglioside diffusion properties across NTs before protein binding. Using the BODIPY

fluorophore attached to G_{M1} , experiments analogous to those presented in Fig. 5.7 demonstrated that the gangliosides can diffuse across NTs with no measurable hindrance.

Strikingly different results were obtained after the gangliosides were incubated with toxin fragments using either G_{M1} -CTB or G_{T1b} -TTC systems. FRAP experiments on ganglioside-bound toxins showed marked diffusion hindrance across NTs. To quantitatively measure this diffusion barrier, we used fluid flow to apply a lateral driving force to the ganglioside-bound toxins (Graneli et al. 2006). The flow within the channel was generated by applying a pressure gradient across the channel using gravity feeding. It basically involved adjusting the water levels of the two reservoirs at the ends of the channel. The maximum flow was achieved when one reservoir was made almost dry. The maximum flow speed in the center of the channel was measured to be up to 1.5 mm/s. The flow speed measurement was done by taking 0.1s snapshots of fluorescently-labeled lambda-DNAs flowing in the channel. The moving DNAs appeared to be bright straight lines in these snapshots. The length of these trajectories divided by the time gave their speed. The largest value observed in many snapshots was assumed to be the maximum speed of water flow in the center of the channel.

We used the G_{T1b} -TTC pair in which TTCs were labeled with Alexa 488 fluorophores (Molecular Probes) to study diffusion of these units near nanotubes. The water flow created a hydrodynamic drag force and drove the toxin-ganglioside units in the direction of the flow. This drag force generated a gradient in the TTC profile, as shown in Fig. 5.9. In each of the three devices shown, the SLB is much brighter on the right side of the electrode than on the left because the drag force drives the TTCs toward the left, where they build up against the electrode.

The most important features in Fig. 5.9 are in the channel connecting the left and right sides of the SLB. At the location where a NT crosses the channel, there is often a dramatic step in the fluorescence intensity profile. Figure 5.9d shows the TTC fluorescence intensity as a function of distance along the channel crossed by a 2.1 nm

diameter NT; the buildup of toxin upstream and the dramatic drop-off at the nanotube are clearly visible. Note the uniform background fluorescence from the SLBs on the walls of the PDMS channels has been subtracted. AFM imaging verified that the discontinuity happened exactly where the NT crossed the channel. The upstream build-up and the sudden drop-off at the NT mean that the NT acts as a significant barrier to the transport of the membrane-bound TTCs. Similar results are displayed for two other devices; the size of the barrier depends strongly on the NT diameter.

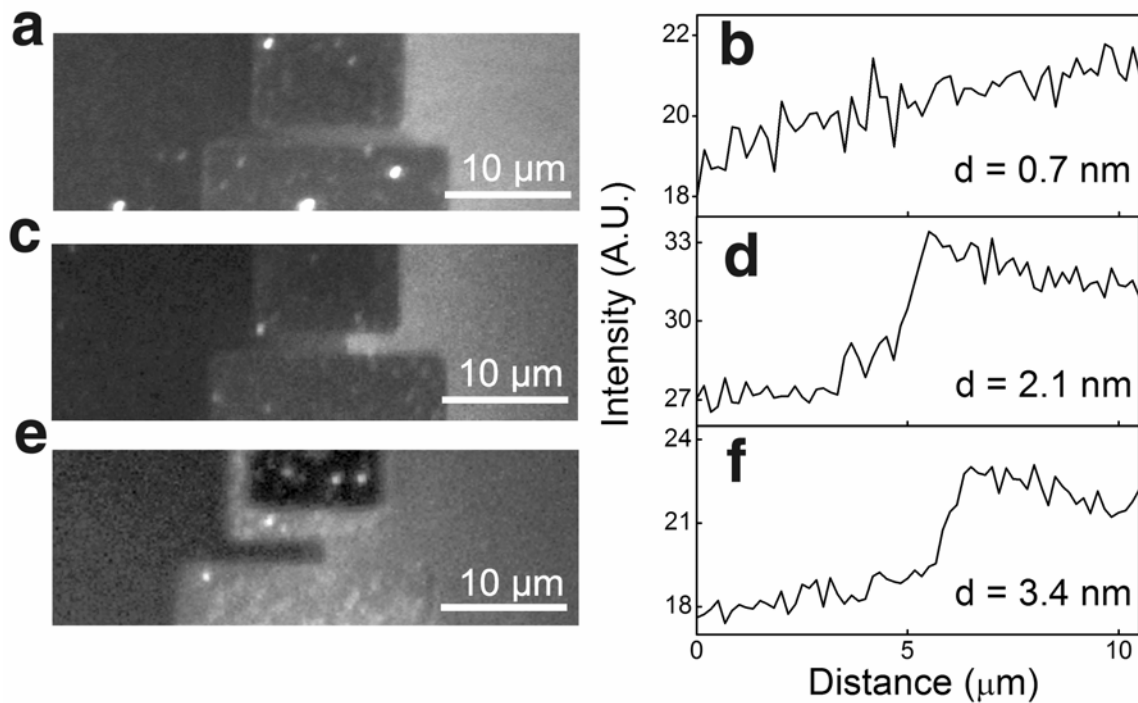


Figure 5.9: Driving ganglioside-bound toxins near SWNTs with flow. (a) Fluorescence image of ganglioside-bound toxin distribution around a 0.7 nm diameter SWNT. The fluid flow was driving the tetanus toxin toward the left side in all images. (b) Fluorescence intensity along the gap. (c),(d) and (e),(f) The same kind of images except the SWNTs crossing the channel are 2.1 nm and 3.4 nm in diameter. The sharp steps in fluorescence intensity happen at the position of the NTs.

We can use the fluorescence intensity profiles to quantitatively determine the magnitude of the barrier presented by the NT to the TTC transport. We first assume the fluorescence intensity is directly proportional to the toxin density, which is valid at low fluorophore concentration. Define n_L and n_R to be the TTC density on the left and right side of the nanotube respectively, and $\Delta n = n_R - n_L$ as the sudden jump of TTC density at the NT. In steady state, the flux density $J = \mu F n + D dn/dx$ should be equal on both sides of the NT. Here F is the hydrodynamic drag force on the toxin, and μ and D are the mobility and diffusion coefficient of the TTC, connected by the Einstein relation $D = \mu k_B T$. By considering the flux on both sides of the NT, we can deduce J and F :

$$J = \frac{D}{\Delta n} \left[\left| \frac{\partial n_L}{\partial x} \right| n_R + \left| \frac{\partial n_R}{\partial x} \right| n_L \right] \quad (5.3)$$

$$F = \frac{K_B T}{\Delta n} \left[\left| \frac{\partial n_L}{\partial x} \right| + \left| \frac{\partial n_R}{\partial x} \right| \right] \quad (5.4)$$

The validity of this calculation can be tested from the extracted drag force on the proteins. For example, for the 2.1 nm tube in Fig. 5.9c-d, the force is calculated from Eq. 5.4 to be around 6×10^{-16} N on each individual toxin protein. This force can be roughly estimated from Stoke's law $F = 3\pi\mu v d$, where μ is the viscosity of water, v is the water flow speed near the protein and d is the hydrodynamic-effective diameter of the protein. The speed of water flow at the center of the channel is measured to be around 1.6 mm/s. The water speed near the proteins is then estimated by assuming non-slip boundary condition and a parabolic velocity profile, which depends on the distance away from the surface. This value is about 0.2 $\mu\text{m/s}$, 1/1000 of the maximum water velocity at the center of the channel. The geometrical size of the protein is used for the hydrodynamic diameter. With these crude estimates, the force is on the order of 10^{-16} N, agreeing with the value

calculated from the toxin profiles in Fig. 5.9 using Eq. 5.4. This indicates that the model is reasonable.

The permeability P of a barrier is defined as: $J = P\Delta n$. Denoting $P_o = D/d$ as the permeability of a patch of lipid with the width of the NT diameter, the ratio P/P_o is:

$$\frac{P}{P_o} = \frac{d}{(\Delta n)^2} \left[\left| \frac{\partial n_L}{\partial x} \right| n_R + \left| \frac{\partial n_R}{\partial x} \right| n_L \right] \quad (5.5)$$

This normalized permeability represents the additional barrier caused by the NT, and can be determined from the fluorescence profile and the diameter of the NT. For the NT in Fig. 5.9c and d, $P/P_o \sim 1.2 \times 10^{-3}$. Normalized permeabilities for other tubes are shown in Table 1. We see that P/P_o is a sensitive function of tube diameter, with the barrier immeasurably small for $d < 1$ nm and immeasurably large for $d > 4$ nm. If we associate this reduction in permeability with thermal activation over a barrier using $P/P_o = \exp(U/k_B T)$, we obtain barrier heights of 0-8 $k_B T$ for NTs with diameter between 0.7 nm to 3.4 nm.

Table 5.1 Summary of normalized permeabilities of 4 nanotube barriers

	Device 1	Device 2	Device 3	Device 4
Diameter (nm)	3.4	2.1	1.8	0.7
P/P_o	5.1×10^{-4}	1.2×10^{-3}	5.6×10^{-3}	~ 1
U ($k_B T$)	7.6	6.7	5.2	~ 0

The suppression of lateral transport of membrane proteins by the nanotubes is reminiscent of similar behavior in cellular membranes where proteins are typically confined in microdomains. A hypothesis consistent with the appearance of functional microdomains is diffusion hindrance by the underlying protein scaffold. Cells have a cortex (Pesen and Hoh 2005), a network of linear proteins (*e.g.* actin or spectrin (Bonetta 2005)) located adjacent to the plasma membrane. This is shown in a schematic of cell membranes in Fig. 5.10, which is more complicated and closer to reality than the Mosaic Model mentioned in Section 4.1. Some studies indicate the cortex provides structural support to the membrane and is involved in the dynamic remodeling of the plasma membrane (Tank et al. 1982; Kusumi et al. 2005).

Currently the correlation between membrane functionalities with their complex diffusion properties is under investigation. However, people previously have not been able to make diffusion barriers in SLBs systems. A mesh of nanotubes (Fig. A.3) can be used as a platform to probe this interesting phenomenon. In principle, the magnitude of nanotube barriers can be tuned with electrical potential since the proteins are charged. Initial trials did not reveal this effect. If that turns out to be feasible, nanotube meshes can match the cell's ability to dynamically change protein distributions.

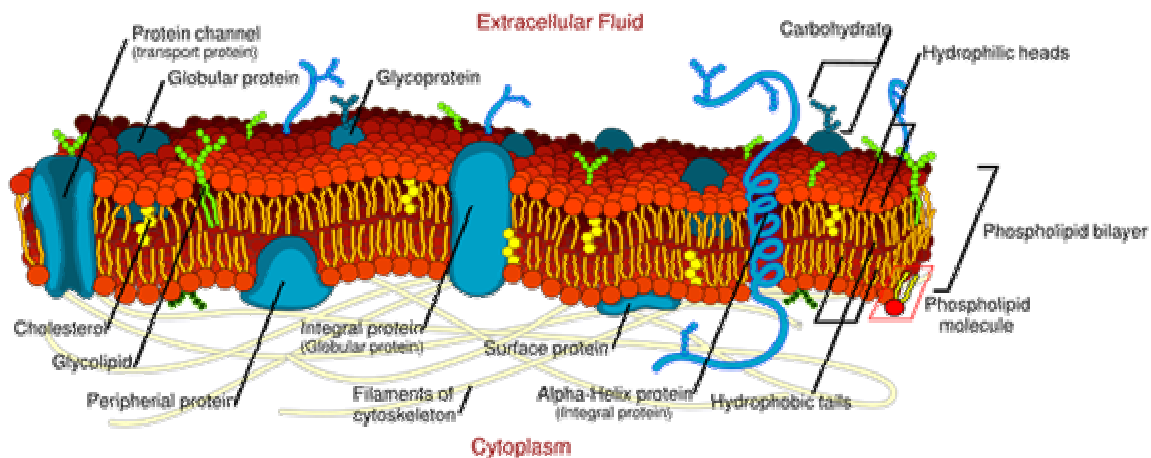


Figure 5.10: A schematic model of cell membrane. This is closer to reality than Fig. 4.1.

5.5 Electrical detection of protein binding

With the physical properties of SLB/SWNT hybrid established, we used the transistor properties of the NT to detect the specific binding of proteins to membrane-embedded targets. The streptavidin/biotin system (Chaiet and Wolf 1964) was chosen for its high binding affinity. A mixed lipid composition, 93.9:4:2:0.1 DOPC:1,2-Dioleoyl-3-Trimethylammonium-Propane (DOTAP):1,2-Dioleoyl-sn-Glycero-3-Phosphoethanolamine-N-(Cap Biotinyl):DHPE-LR, was used to form SLBs functionalized with biotin, as shown in the upper right inset to Fig. 5.11. All lipids were from Avanti Polar Lipids. To minimize ionic screening, 1 μ M PBS buffer with 10 μ M NaCl was used.

Note the positive charge on DOTAP and negative charge on the biotinylated lipid. The purpose of DOTAP is to facilitate the SLB formations. When only biotinylated lipids are mixed into DOPC vesicles, they do not form SLBs in the low ionic strength buffer. It is speculated that the electrostatic repulsion between biotinylated lipids and silicon oxide surfaces, which have negative surface charges in this condition, prevents vesicle fusions on the substrates. The addition of DOTAP solved this problem.

To isolate the electrodes from the electrolyte, the device was covered with a 30 nm thick Al_2O_3 layer except in the regions between the source and drain electrodes containing the nanotubes, as shown in the lower left inset. When the Al_2O_3 layer is used in combination with microfluidic channels, the leakage current between the electrodes and the water solution is minimized. To reduce noise, a 10 mV AC source-drain bias at 155 Hz was applied across the SWNT FETs and the conductance G was measured with a lock-in amplifier. A gold electrode immersed in the buffer solution controlled the potential V_e of the solution (Rosenblatt et al. 2002; Larrimore et al. 2006). All measurements were done in the same buffer after unfused vesicles and unbound proteins had been flushed out of the channel. SLBs formed only in regions not covered with Al_2O_3 .

Fluorescence microscopy revealed that the SLBs formed were uniform and laterally mobile, and that the streptavidin/ biotin binding was stable even after washing.

Figure 5.11 shows how the conduction of SWNT FETs was affected by SLBs formation and streptavidin binding to the biotins imbedded in the SLBs. The solid black curve in the main panel of Fig. 5.11 shows G vs. V_e before the lipids were added, while the red dashed curve was taken after the formation of SLB. The positively-charged SLB significantly shifted the threshold voltage V_t of the NT FET. However, this cannot be attributed entirely to charges on the SLBs. As shown in Fig. 5.12, similar shifts are observed when neutral DOPC lipids are formed on SWNT-FETs in 1X PBS buffer. The average shift is 240 ± 70 mV. The threshold voltage shifts backwards when the SLB is removed with detergent. The mechanism of this phenomenon is under investigation. It is suspected to be related to the intrinsic dipole of DOPC (Fig. 4.3). But the silicon oxide surface and the water cushion layer between the SLBs and the substrate can also be the cause. The magnitude of the shift was larger with this positively charged lipid mixture in low ionic strength buffer in Fig. 5.11.

After the formation of SLBs with embedded biotins, the device was then incubated with $5\mu\text{M}$ streptavidin for 10 minutes and rinsed. The bound streptavidins shifted V_t back toward positive voltages, as shown by the green dotted curve in Fig. 5.11. No shift was observed in control experiments where proteins that do not bind to biotin were added (*e.g.* tetanus toxin), demonstrating the specificity of the detection.

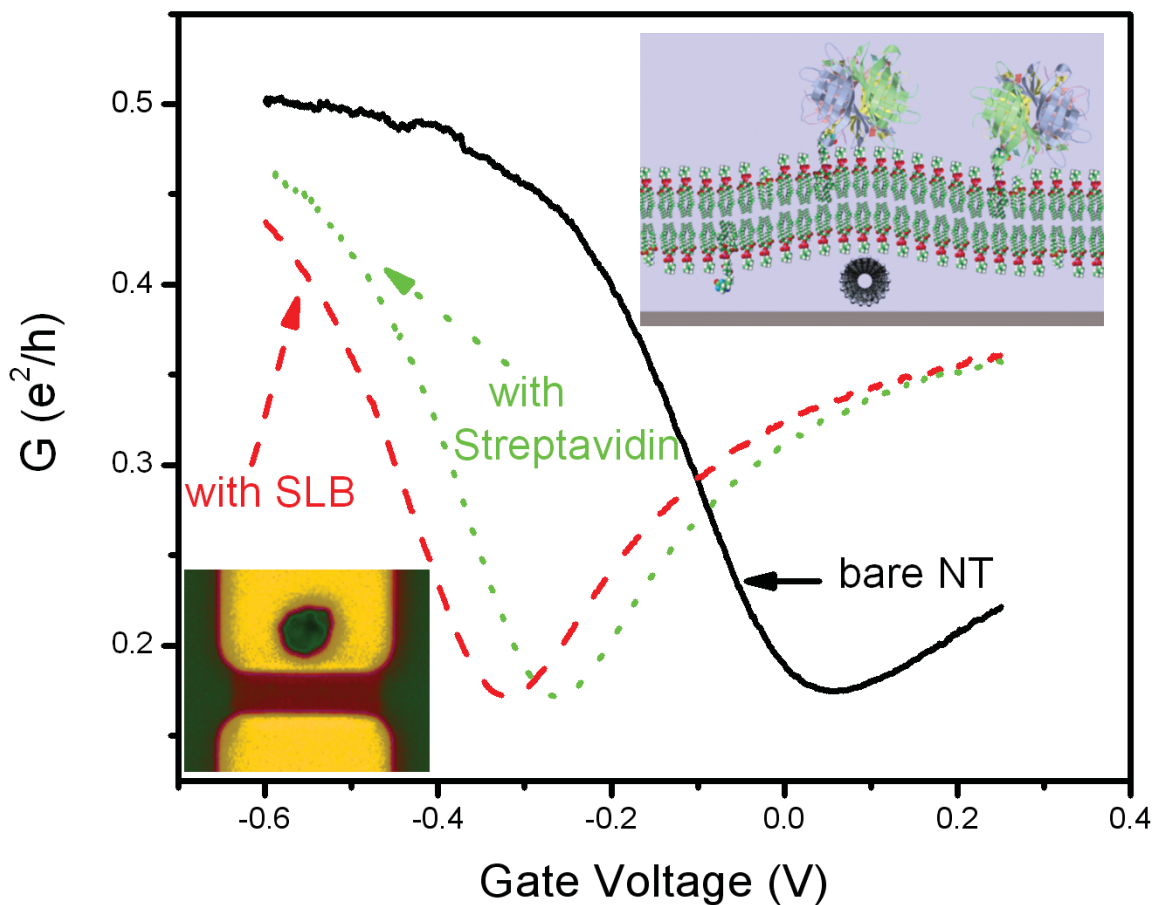


Figure 5.11: Detection of biotin-streptavidin binding with SWNT FETs. Conductance versus electrolyte potential of a small-bandgap NT FET before (solid black) and after (dashed red) biotinylated SLB was formed on the surface. The dotted green curve was taken after streptavidins bound to membrane-imbedded biotins. **Lower inset:** Optical micrograph of devices used for sensing. The pink rectangular region between two yellow electrodes is the only opening in the Al_2O_3 insulation layer. **Upper inset:** Schematic of a carbon nanotube under biotin-functionalized lipid bilayer.

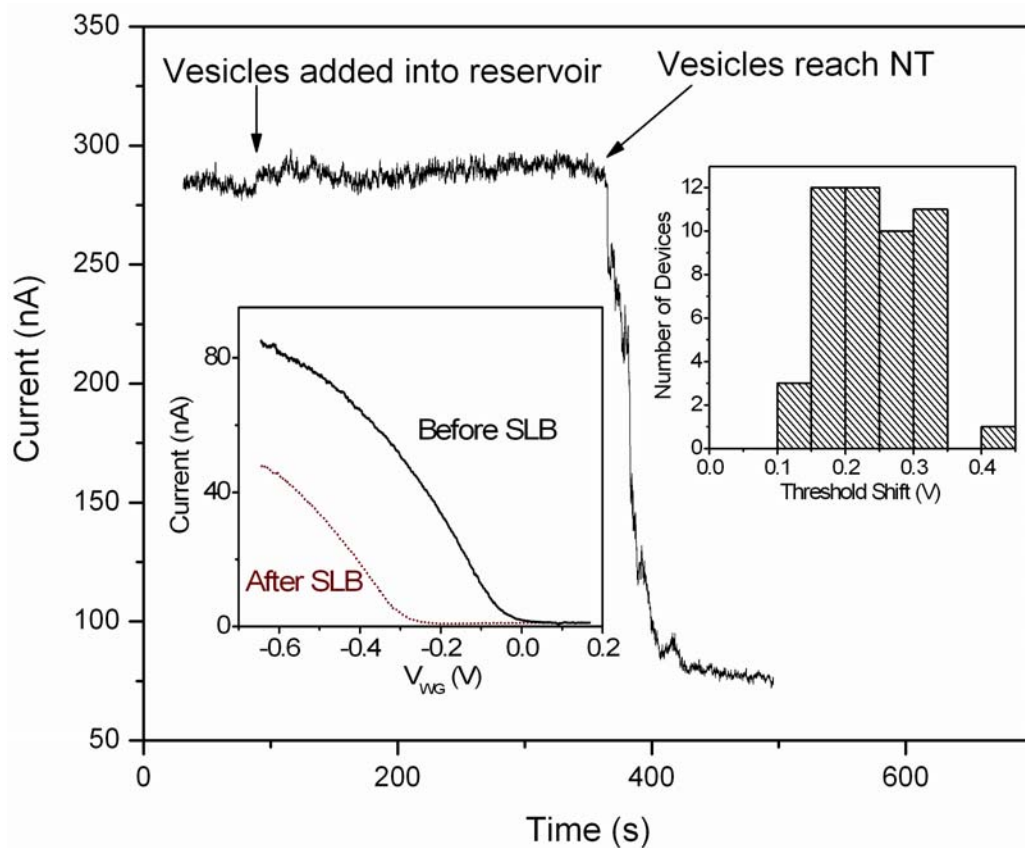


Figure 5.12: Detection of DOPC SLB formation with SWNT FETs. Current under constant 10 mV bias versus time for a SWNT FET during formation of a DOPC SLB in 1X PBS buffer. The drop in conductance happened when vesicles fused on the SWNT. **Lower inset:** Current versus V_g for a semiconducting SWNT FET before (black solid curve) and after (red dotted curve) SLB was formed on top. **Upper inset:** Histogram of the threshold voltage shifts induced by DOPC SLB formation in 1X PBS buffer.

For the six devices studied, the shift of threshold voltage ΔV_e caused by streptavidin binding was $\Delta V_e = 80 \pm 20$ mV. Using the model in reference (Artyukhin et al. 2006) that relates voltage shift induced by a layer of charge to its charge density: $\sigma = 2\Delta V_e \epsilon_w \epsilon_0 / \lambda_d$, where ϵ_w is the dielectric constant of water and λ_d is the Debye length, we estimate that the observed ΔV_e corresponds to an additional charge layer with $\sigma = -7 \times 10^3$ e/ μm^2 . The sign of σ agrees with streptavidins being negatively charged at the buffer pH and the charge density is comparable to the biotin density in the SLB of 3×10^4 e/ μm^2 . The correlation can also be viewed from a surface potential point of view. Refer to Appendix D for discussions.

The system studied is only one example of specific binding detection, any other charged protein that binds to a target located within the SLB should cause a similar effect on the SWNT FETs. The bilayers can be readily functionalized with many molecules. It is feasible to use the SLB/nanotube hybrids to study other binding systems. Another advantage of the structure is it eliminates the influence of chemically-active silicon oxide surface, whose surface chemistry and charge density are easily modifiable to complicate experimental observations. The lipid surface is relatively inert compared to silicon oxide, and helps to isolate the events of interest.

In conclusion, we have used electrical and fluorescence measurements to probe supported lipid bilayers formed over carbon nanotube transistors. We show that the lipid molecules in a SLB can diffuse freely across nanotubes while ganglioside-bound toxins see a NT-diameter-dependent diffusion barrier. We further demonstrate electrical detection of protein binding on the lipid bilayers with NT transistors. This new lipid/NT model system has many potential applications to the study of both electrical and mechanical perturbations at cell membranes. This system can also serve as a generic platform for bringing mobile lipid-bound molecules and NTs in close proximity for studies of the physical, electrical, and optical interaction of single molecules with NTs.

CHAPTER 6

CONCLUSIONS

6.1 Summary

We have studied electron transport in carbon nanotubes in the electron-phonon scattering limited regime and found out the performance limits of nanotube transistors as well as the dependence of their resistance and mobility on tube diameter and temperature. We have also integrated nanotubes with supported lipid bilayers (SLBs) and used this structure to detect protein binding events on the bilayers.

To learn the intrinsic electrical properties of nanotubes, we performed systematic studies of nanotube transistors using moderately long and high quality nanotube samples in Chapter 3. Their electrical conductance and mobility were measured at various temperatures and correlated to their diameters. It was found out that, after the influence of the contact resistance was eliminated, the conductance grows linearly with tube diameter while mobility grows quadratically with tube diameter. They both scale inversely with temperature, indicating the important role of phonons. A theory model was established, based on electron-phonon scatterings, to explain how the electrical transport is modulated by gating and temperature. It predicts the same scaling behaviors as observed in the experiments and agrees favorably with the measured conductance and mobility values. In conclusion, this study shows the electron-phonon scattering is the dominating source of resistance in long nanotubes, and gives performance limits of nanotube transistors working in this regime.

We integrated carbon nanotubes with supported lipid bilayers in Chapter 5. Experiments were carried out to confirm the quality of SLBs by measuring the lipid diffusion coefficients. Lipid diffusions near nanotubes were also tested to show that lipids can diffuse over the nanotubes without much hindrance and the bilayer is continuous over

the nanotubes. However, nanotubes act as barriers for a protein bound to a membrane-embedded receptor. This hybrid structure was used to detect biotin-streptavidin binding events on the bilayer in low ionic buffer. The observed signal can be related to the protein charges. In conclusion, besides being sensitive electrical detectors, the SLB/nanotube hybrids can be used to probe the correlation between protein diffusion properties and their functions.

6.2 Future directions

We have presented the current status of our research on lipid bilayers with nanotubes in Chapter 5. However, it should not be view as an end, but rather as just a beginning. We have not yet really touched the biological function of membrane proteins, which are important cell constituents. Some of them control the transport of various molecules/signals (Doyle et al. 1998) into and out cells while some others are responsible for generating energy inside cells (Salafsky et al. 1996). A few examples of the properties that could be studied with lipid bilayer/nanotube hybrids are: diffusion coefficients of membrane proteins, transport properties of ion channel proteins/photosynthetic centers, association/dissociation rates of reversible protein/receptor bindings, and charge detection of single proteins. The high sensitivity of nanotube FETs combined with micro-fabricated structures allows most of the studies to be done at single protein level with high speed to reveal properties that are otherwise concealed due to averaging. Another direction of the proposed future research will be to integrate carbon nanotubes with real cells. The conduction channel of the nanotube FET can be placed either close to a cell membrane or even inside the cell and used as a sensor or electrical probe.

Applying nanoelectronic science and technology into biology is a new field and has a promising future. The proposed projects are examples of using nanoscale structures

as electronic interfaces to study biology at single-molecule level in an unconventional way.

Probing membrane protein dynamics

Although we have been able to specifically detect protein bindings to membrane-embedded receptors in Section 5.5, more information can be obtained from this experiment. The induced threshold voltage shift fluctuates when proteins diffuse around nanotubes. In principle one could study the noise spectrum of lipid bilayer/nanotube FET hybrids, distinguish the part of noise that is induced by membrane proteins in the lipid bilayers and extract their properties such as diffusion coefficients and charge densities. The experimental scheme is inspired by optical FCS, mentioned in Section 5.2. But in this proposed experiment, the current change induced by the presence of membrane proteins plays the role of fluorescence intensity in FCS. The merits of this experiment over FCS are it does not require labeling molecules with fluorophores and offers higher spatial resolution.

In this experiment, neutral SLBs with membrane proteins would be first formed on top of nanotubes in the same geometry as Fig. 5.3 shows, and the noise spectrum or current fluctuations of nanotube FETs under constant bias should be recorded before and after introducing molecules to bind with the membrane proteins. With careful modeling and calibration using proteins of known diffusion coefficients and charge densities, a correct fitting to the data should provide these two parameters of other proteins.

The characteristic time scale in this experiment is set by the Debye screening length l_d of the buffer solution, and the diffusion coefficient (D) of membrane proteins. To minimize charge screening, the experiment should be carried out in buffers with $l_d \sim 100$ nm. The typical value of D is around $1 \mu\text{m}^2/\text{s}$, and the time scale for membrane proteins to diffuse through the nanotube FET detection area is about 10^{-3} s. This is well

within the ability of most spectrum analyzers or current pre-amplifiers. One benefit of looking at these high-frequency signals is that nanotube becomes a quieter sensor at higher frequency because $1/f$ noise is the dominating noise source in SWNT-FETs (Collins et al. 2000).

Study of protein binding dynamics at single molecule level

The experiment proposed in last part deals with the statistical behavior of multiple proteins. Another ambitious experiment scheme is to reach higher charge sensitivity by reducing the length of nanotube conduction channel. In the experiment illustrated in Fig. 5.11, the detection limit is about 2 mV in gate voltage at 1 KHz bandwidth. It means that when the gate voltage is shifted by 2 mV, the induced current change can barely stand out of the noise. Using the known capacitance of nanotube in solution (Rosenblatt et al. 2002) $C = 4 \times 10^{-10}$ F/m, this corresponds to bringing $5|e|$ into a 1 μ m long nanotube FET. If the conduction channel is further reduced to 100 nm, this system can reach single charge sensitivity regime. Then it is possible to see the on-off signatures of a single reversible binding event or the lateral diffusion of a single protein.

To study the association/dissociation dynamics, it is better to have static proteins near nanotube FETs, since the membrane proteins are diffusing in the bilayer all the time. This part of study may be done with chemically functionalized nanotubes, to which proteins are directly attached (Besteman et al. 2003). This opens up possibility of studying even more types of molecules besides membrane proteins.

Probing the transport properties of transmembrane proteins

One advantage of the lipid bilayer/nanotube hybrid structure is that there is a continuous membrane separating the bulk solution from the water layer underneath the SLB, where nanotube sits. Therefore a new kind of interesting experiment can be based

on using nanotubes as electrodes to probe the potential difference between the two water regions on each side of the membrane.

Membrane proteins can produce an ion concentration difference across a membrane, which generates an electrical potential according to Nernst equation $\Delta E = \ln(C_2/C_1) \times k_B T / ne$, where C_2 and C_1 are the ion concentration inside and outside the membrane, and $k_B T / ne$ is about 59 mV at room temperature for $n = 1$. Two examples of proteins that can generate cross-membrane potentials are: (1) Bacteriorhodopsin, which absorbs light and uses this energy to pump protons across the membrane (Khorana 1988), and (2) potassium ion channels, which selectively transport potassium ions across the membranes while blocking other ions (Doyle et al. 1998).

In this experiment, the lipid bilayer/nanotube hybrid structure should be slightly modified to probe this membrane potential. As shown in Fig. 6.1, the nanotube chip surface would be covered with dielectric layer except the regions around nanotube conduction channels. A patch of SLB would form at these openings where the nanotubes sit. Effectively, the nanotubes are contained inside a tiny aqueous chamber. Because lipid membranes have extremely low permeability to charged ions, the only pathway for ions to exchange between this chamber and the bulk solution would be through the membrane proteins.

Ion transport through the membrane proteins would be triggered by external stimuli. In the case of Bacteriorhodopsin, light can be shone onto the structure. In the case of an ion channel, the bulk solution could be flushed with a buffer of different concentrations or ions. The potential associated with these events would be monitored using nanotubes as electrostatic potential sensors (Larrimore et al. 2006).

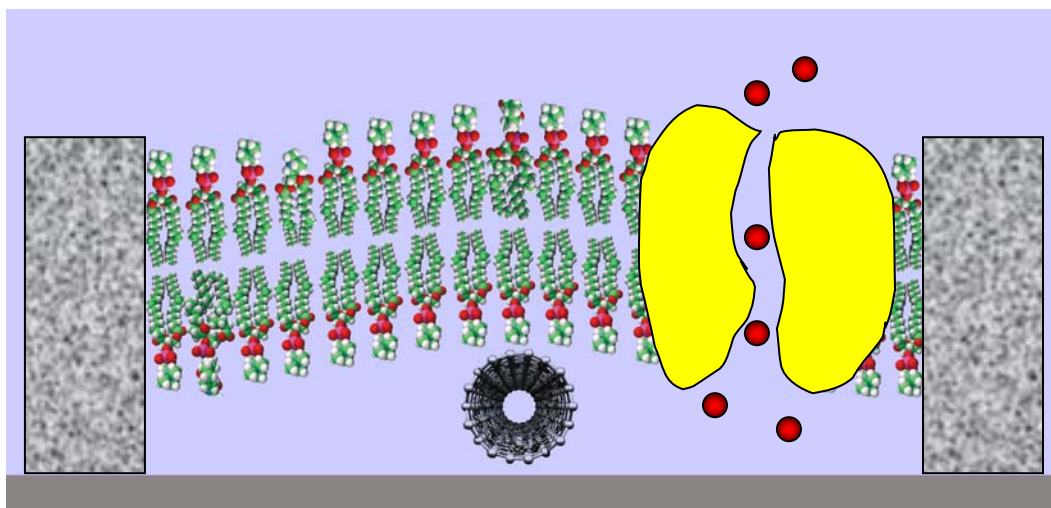


Figure 6.1: Schematic of the proposed structure to use nanotube as cross-membrane potential sensor. Nanotube is sealed by a patch of membrane and the surrounding dielectric (shown as rectangles in granite) layer that defines the well. Membrane protein bridges the two water regions on either side of the membrane and selectively allows ions to pass through.

Some membrane proteins lose their function inside SLBs because part of the protein protrudes out and denatures on the substrate surface as mentioned in Section 4.1. In that case, lipids with very large head groups, such as polyethylene glycol as a spacer in the head group, can be used to increase the spacing between SLBs and substrates to a few nanometers. Another solution is to lay a polymer cushion layer under SLBs (Sackmann 1996).

One needs to get a sense of how small the chambers around nanotubes are. Regions with $\sim 10 \mu\text{m}^2$ cross section can be easily fabricated with photolithography, and ones with $\sim 0.1 \mu\text{m}^2$ cross section can be made with electron beam lithography. The height of these chambers is the thickness of the water cushion layer between SLBs and

substrates, which can be as small as 1-2 nm. The volumes of these chambers are therefore around 10 aL to 0.1 aL.

With such a small volume underneath a SLB, even a single protein can generate a detectable cross-membrane potential on a short time scale. Let us consider potassium ion channels as an example. Suppose the chamber volume is 10 aL and the initial buffer is 100 mM potassium chloride. When the bulk solution is replaced with 1mM potassium chloride and the potassium channel is opened, a single protein can decrease the concentration of potassium ions underneath the membrane down to 1mM within 6 ms (using the reported transport rate of $\sim 10^8$ ions/sec (Saparov and Pohl 2004).) The concentration difference of Cl^- ions across the membrane will produce a potential difference of about 120mV, which can be easily detected by nanotube FETs. However, it would be interesting to see how the transport rate slows down with increasing cross-membrane potential and at what potential the ion transport stops. This technique allows study of the functioning of single membrane protein in real time.

If the chamber volume is reduced to 0.1 aL and the potassium ion concentration is 10 mM to start with, the outflow of a few hundred potassium ions from the chamber can be detected. This is a sensitivity no other technique can reach. Another advantage of this powerful tool is that multiple studies can be done in parallel on a single chip. Nanotube/SLB hybrids can become an important new platform for studying the function of single membrane proteins.

Integrating nanotube FETs with cells

Naturally, the next stage of this series of experiments is to study real cells. This can be done in two schemes: (1) place nanotubes directly against the external side of the cell membrane, or (2) place them inside cells. These experiments may lead to the

invention of electrical sensors that can directly monitor single cell activities and measure properties inside cells that cannot be done with current methods.

In the first scheme, the patch of SLB in Fig. 6.1 can be replaced with a real cell membrane. Recently Prof. Lieber's group at Harvard University demonstrated that neuron activities can be detected with nanowire array (Patolsky et al. 2006) in a similar fashion. Since nanotubes have higher mobility and transconductance (Rosenblatt et al. 2002; Zhou et al. 2005), integrating cell membranes with nanotube FETs will offer higher sensitivity compared to nanowires. The well formed by dielectric layers around nanotubes in the proposed structure in Fig. 6.1 not only helps to minimize the sensing region to a small area, but also helps to confine the product molecules of cell activities around nanotubes. It will further improve the signal strength.

In the second scheme, a special property of SWNTs will be applied: their ultimately-small sizes. SWNT diameters are comparable to that of a DNA molecule. Therefore it may be possible to put the conduction channels of nanotube FETs inside cells without drastically disturbing them. A structure is proposed as shown in Fig. 6.2. The substrate underneath nanotubes is etched away so that nanotubes are suspended in solution. A cell will be brought in with a micromanipulator and put on top of a suspended nanotube FET. The suspended part of nanotube has a chance of penetrating the cell membrane and entering into the cell body. It will be interesting to see how this is going to affect cells and if cell skeletons and membrane cortexes will stop this intrusion.

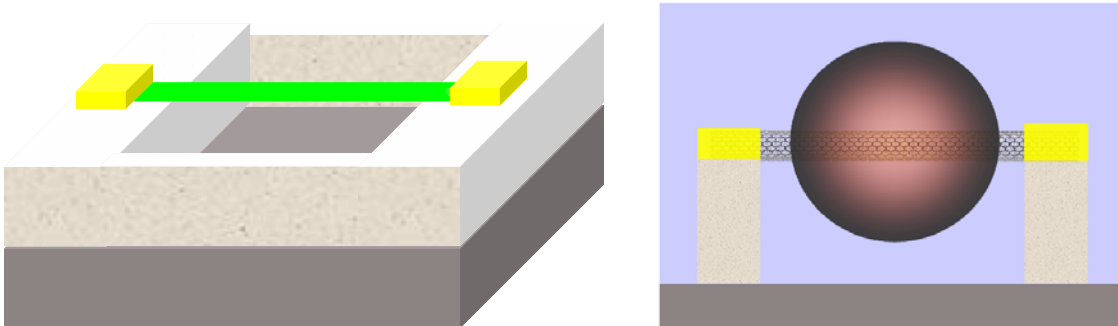


Figure 6.2: **Left**, schematic of a nanotube (green cylinder) suspended over a trench. **Right**, when a cell (magenta sphere) is placed on top of a suspended nanotube, the nanotube may be able to penetrate inside the cell.

If suspended part of nanotube FETs do indeed go inside cells, it could act as a detector to sense the ongoing electrical activities inside the cell or an electrical probe to control those processes! There are many fascinating experiments to perform. For example, carbon nanotubes have been functionalized to detect glucose concentration in solution (Sotiropoulou and Chaniotakis 2003). Nanotubes can be modified with the same chemistry and do sensing inside cells with this method. Besides molecule sensing, nanotubes can also serve as electrodes to probe the electrical potential inside cells, or to stimulate cells with electrical pulses. A wilder idea is to break nanotubes inside cells by running relatively high current ($\sim 20 \mu A$) through them, which turns a single nanotube into two adjacent electrodes. They could be used as dielectrophoresis tweezers (Zheng et al. 2004) to manipulate molecules. Currently micropipette can be inserted into cells. This proposed nanotube probe, however, is less intrusive due to its much smaller size, and has higher spatial resolutions to map out different regions of cell bodies.

In conclusion, carbon nanotube transistors are novel systems that offer promises in diverse areas ranging from real-time observation of protein dynamics to the study of

cell activities. They can solve fundamental scientific questions as well as generating new tools for biophysics. Using nanotubes to electronically 'see' single molecules has the potential for the same kind of scientific impact as single molecule fluorescence techniques have demonstrated. However the ideas offered here are not guaranteed to work, some of which may not be even theoretically correct. They are provided to stimulate people's wildest imaginations to discover the potential of the new nanometer tools.

APPENDIX A

NANOTUBE GROWTH

The Japanese has a proverb: those who control materials will control technologies. This is certainly true in some sense. Material growers are highly appreciated in Japan. It has enabled them to have some of the best material samples in the world. Carbon nanotube was discovered in Japan in 1991 (Iijima 1991), which may or may not have been accidental.

Although our lab is in Physics, but the current situation forces us to grow nanotubes ourselves. Therefore it is important for Physics students to master nanotube growth. I recommend new students spend their first few weeks in the furnace room. This is the hardest part of making devices. Compared to the cleanroom part, which is very standardized and highly repeatable, nanotube growth still remains in the dark magic phase and one needs to get some kind of feeling. When the device fabrication fails, more than often it is due to something in the furnace. To emphasize the importance of materials, a story about graphene must be told. Many years ago our beloved adviser, if not the first person, had foreseen the unique physics and potential impacts in graphene. But no one could make a high quality single layer graphene until a group in University of Manchester was lucky enough to find an effective way to do so (Novoselov et al. 2004). It is indeed a gold mine.

The situation in the case of nanotubes is better. It is very easy to grow nanotubes using chemical vapor deposition (CVD) in our lab. But it is somewhat hard to get exactly the kind of nanotubes needed. The properties need to be controlled include tube diameter, length, orientation, yield and cleanness. Chirality control would be great, but it is impossible as of today. Here, I will share some experience and techniques from me and

other people in the lab. Not everything is guaranteed to be correct. Possible improvements that have been demonstrated by other groups will also be presented.

Diameter control

It can be seen in almost every chapter of the thesis that diameter is one the most important parameters of nanotubes. The bandgap of a semiconducting nanotube is inversely proportional to tube diameter and the mean free path goes linearly proportional to diameter (Chapter 2, 3). It is widely accepted that, in CVD growth, the tube diameter is controlled by the size of the catalyst nanoparticles (Cheung et al. 2002). Personally, I think it is not entirely true in at least one respect: it is hard to imagine growing large nanotubes from much smaller particles; but it is possible to grow tubes smaller than the particle size, especially if the catalyst particles are not in liquid phase (Kodambaka et al. 2007).

Since there is typically a broad diameter distribution with any kind of growth recipes, we can select the nanotubes with the targeted diameters. The standard recipe, 900 °C Methane growth, normally gives large diameter tubes (Kong et al. 1998). In their original paper, Dai group claims that the tubes are between 1-3 nm. However, the tube diameters were measured using AFM at scan range of 10 μm . This dramatically underestimated the tube diameters. The good thing is that the authors have done extensive TEM studies to show their fat tubes are still single-walled. The other recipes, using very thin evaporated iron film as catalyst or soaking chips in iron nitride/methanol solution and growing at 700°C with Ethylene, tend to give thinner tubes in my experience.

If one wants to do better than that, efforts need to be put into making near identical catalyst particles and preventing them from aggregation at high temperature. A few recipes with better diameter control involve using Ferritin protein (whose iron content can be controlled) (Li et al. 2001), block copolymers (size of iron containing

segment can be controlled as well) (Lu et al. 2005) and identical metal containing nanoclusters (An et al. 2002). But complicated catalyst preparations go beyond the ability of Physics students. Collaborations may be needed.

Long and aligned nanotubes

Having longer tubes is never a disadvantage. They enable ones to study the intrinsic properties of nanotubes in electrical transport and optical applications. The first method that can get individual nanotube longer than one centimeter was discovered by Jie Liu's group at Duke University (Huang et al. 2003). The key to this recipe is to get catalyst particles off the substrate, by the turbulence as a result of fast heating, so that the growth is happening in the gas (Huang et al. 2004). Liu argues that the strong Van der Waals interactions between substrates and tubes/catalyst make them difficult to slide on the surface, and stop the growth prematurely.

We were lucky to learn their fast heating technique. Although our tubes are not as long as theirs and the yield is not very high, but it still can help us in many cases. The less satisfactory results in our lab may be due to the different carboneous gas we use (Methan/Ethylene) as compared to theirs (Carbon monoxide).

There are other recipes to grow long tubes without the fast heating step. Liu group also used an alcohol CVD to grow centimeter long tubes without any special measures to lift up the catalyst (Zheng et al. 2004). But this does not rule out the possibility that the tubes are flying in gas during growth. Another amazing result from a UIUC group, however, shows that their long tubes are actually grown on the substrates (Kocabas et al. 2006). Figure A.2 is taken from their publication. The substrate is [2,1,10] single-crystal quartz wafer. The nanotubes have a preferred orientation and can grow more than 100 μm . Similar effects have been seen on more expensive Sapphire substrates as well (Han et al. 2005). Since people in our groups are growing tubes on transparent quartz substrates to

either eliminate the backgate or to allow better optical imaging, it should be natural to try these single-crystal quartz substrates with special cuts, if they are not too expensive.

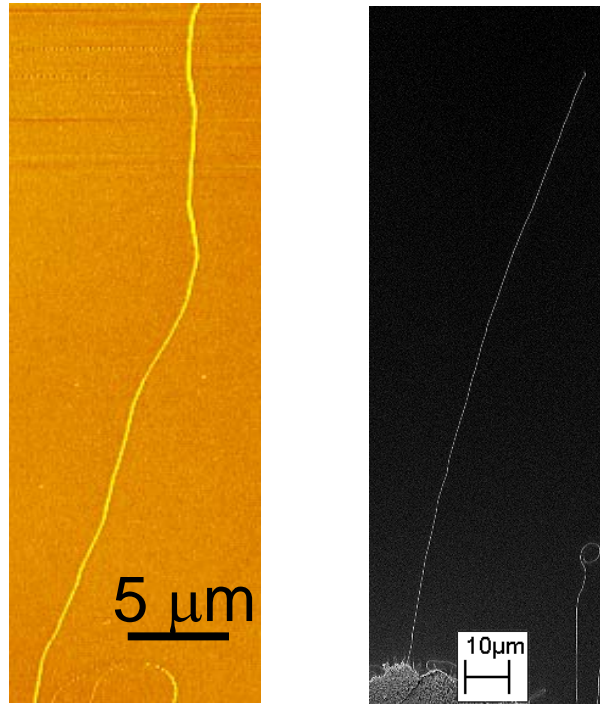


Figure A.1: Two long (~100 μm) nanotubes grown with the Duke recipe in our group.

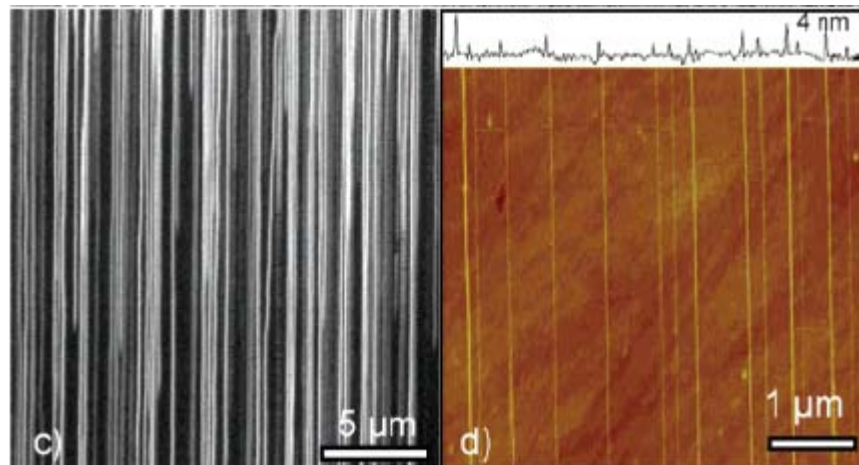


Figure A.2: Long and highly aligned nanotubes grown on quartz substrates (Kocabas et al. 2006).

Yield

Normally the yield is not a problem in our lab. One can adjust catalyst concentration, catalyst pad size and other parameters to control the yield to a preferred level. There are two cases where yield needs to be significantly increased. First in some experiments, it would be great to have really densely packed nanotube meshes. One example is Jose and I wanted to suspend lipid bilayers with nanotube meshes as support. Second, the fast-heating long tube growth recipe generally gives sparse nanotubes. One problem with that recipe is the nanoparticle catalyst easily gets off the wafer during the lift-off process that is used to define catalyst pads. In both cases, a better lift-off process can help.

Currently catalyst pads are defined using photoresist or electron beam resist. The lift off is done in a solvent, either organic or water, to dissolve the resist, during which catalyst can get off the substrates. A dry lift process can solve this issue. The key is a polymer called parylene (Zhang et al. 2003; Moran-Mirabal et al. 2005) . A few properties make it an ideal material. First, a thin layer ($\sim \mu\text{m}$) can be deposited on substrates from gas phase. CNF recently bought a machine to do that. Second, parylene does not dissolve in common solvents, and is compatible with photo lithography processing. A layer of normal photoresist can be spun on top of parylene film to define micrometer size features, which can then be transferred into parylene layer by oxygen plasma etching. Third, the parylene layer, although extremely thin, can be mechanically peeled off from the substrates using tweezers.

Figure A.3 shows a SEM image of nanotube meshes made for the lipid bilayer suspension purpose. The rectangular, where nanotubes are densely packed, was initially defined using parylene film. Nanoparticle catalyst solution was dried on the surface, followed by peeling off the parylene film. The end result is a nice nanotube mesh without too much catalyst residue.

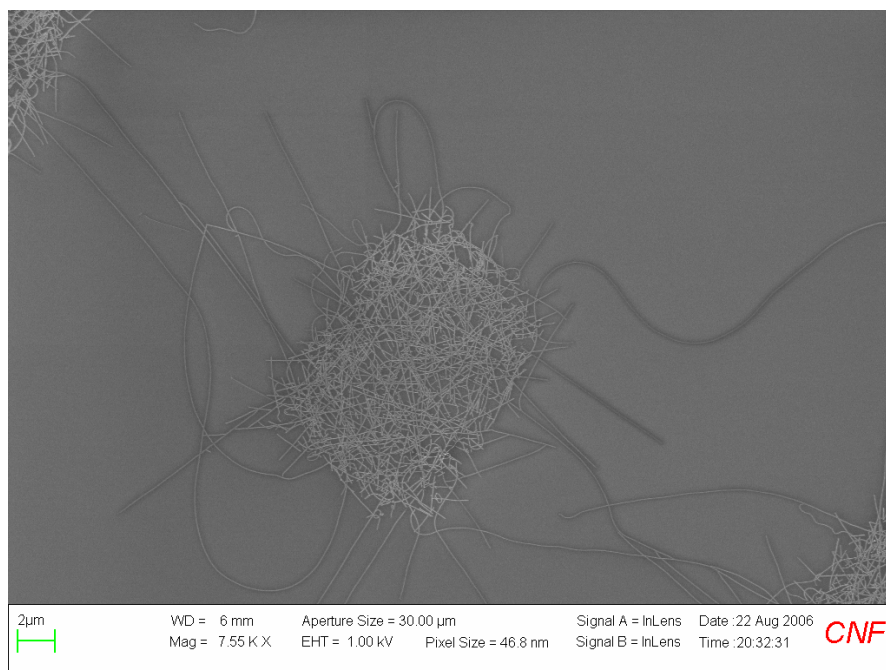


Figure A.3: A dense mesh of nanotubes grown in a region defined by parylene.

I have not tried to increase the fast-heating growth yield with this trick yet. The parylene technique should also be useful for other purposes where the dry lift-off is desired.

Vertical nanotube forest

Another different type of CVD nanotubes is called vertical nanotube forest. Basically, when the nanotubes are densely grown (one per 20 nm x 20 nm), the Van der Waals interaction will facilitate them to stand up and form a forest-like structure.

Typically people in our lab are not interested in this type of nanotubes since we study individual ones. However this could be useful for our collaborators and we can exchange the nanotube forest for their help. The key to nanotube forest is density. First, the catalyst particles need to be densely packed. Second, most of the nanoparticles need

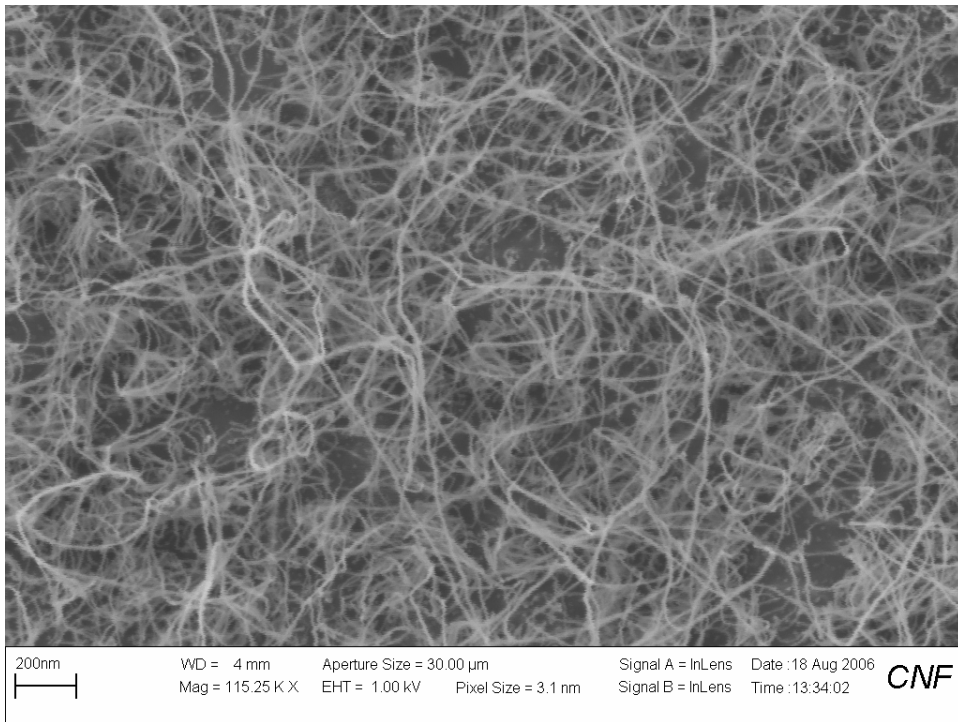


Figure A.4: Nanotube mesh grown without water vapor in the CVD chamber.

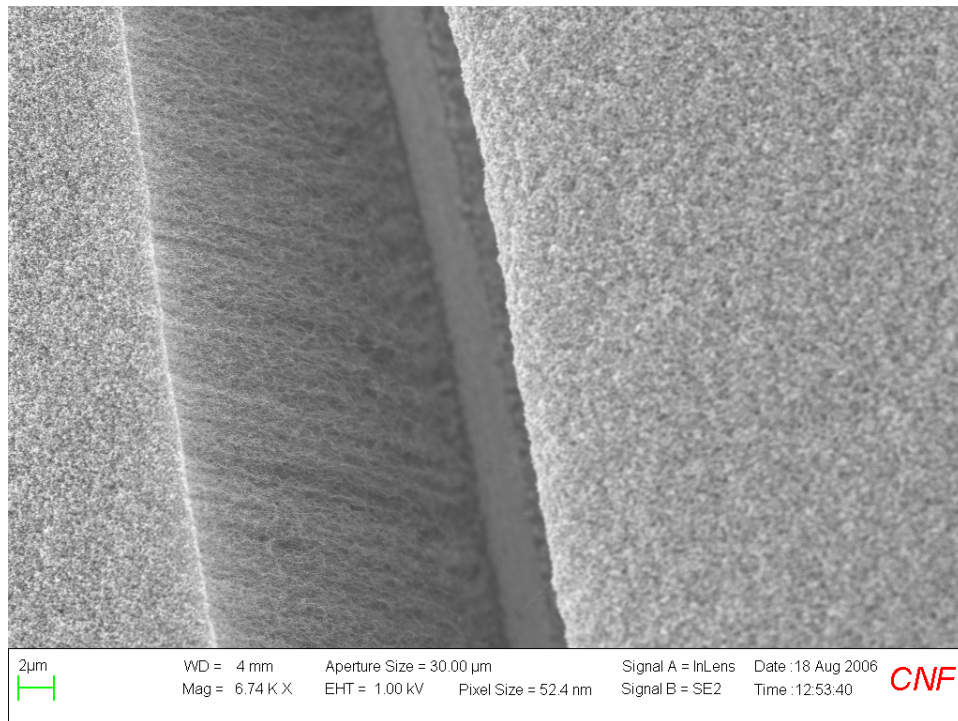


Figure A.5: Aligned nanotube forest grown with water vapor in the CVD chamber.

to be active during growth. These two conditions would prevent nanotubes from falling onto substrates during growth.

A thin layer of iron is typically used as catalyst particle precursor. The iron film breaks into individual particles at elevated temperature. Even a 0.5 nm iron films (this value should be consider as nominal) can lead to large particles and thus multi-walled nanotubes. Many groups use underlayers such as alumina oxide or molybdenum beneath the iron layer. It is not necessary. The key to make catalyst active and remain active for a long time is introducing small amount of water vapor into CVD chambers (Hata et al. 2004). Figure A.4 is a SEM of nanotubes grown using thin film iron as catalyst. The growth condition is tuned to extremely high yield, but no water vapor is added. The nanotube density is high, but it is not high enough for nanotubes to stand up. The vertical nanotube forest shown in Fig. A.5 is grown under the same condition except a small amount of water vapor is added. It seems to indicate, besides etching way amorphous carbon coating on catalyst particles to prevent them from being poisoned, water also helps to make every catalyst particle work from the very beginning. The water content is not carefully controlled in this case. Mine record is 5 mm tall forests. And the world record is a few centimeters.

In conclusion, there are many tricks to grow nanotube for one's special needs. We should not be constrained by the kind of tubes we can make. Better tubes can lead to new functionality.

APPENDIX B

VALIDATION OF THE THEORY MODEL IN CHAPTER 3

When the experimental data and theory calculations on electron-phonon limited transport are presented in Chapter 3, it seems the theory in Sections 3.2-3.4 is able to explain most of the experimental observations. But it does not include many subtleties. Here are two examples of some major concerns: 1. Does conduction depend upon the chirality of nanotubes? 2. What if more than one subband participates in transport? These questions will be addressed in this appendix.

Chirality

Up to today, people do not have the ability to control growth conditions to get tubes with specific chirality. In many cases, it is almost impossible to determine the chirality of a nanotube sample. It can be done with STM or a few optical spectroscopy techniques as mentioned in Chapter 1. But the processes are difficult to carry out on the device geometries that are typically used to study transports. In our experiments, the chirality of a nanotube device is not known. And there is no reason not to believe that the chiralities of an ensemble of nanotube devices are widely distributed over all possible values.

Not surprisingly, in many cases chirality comes into the horizon. In Minot's study of nanotube band structure modulations from mechanical deformations (Minot et al. 2003), the degree to which the band structure is modified strongly depends on the nanotube chirality. Similarly, it turns out the electron-phonon coupling is chirality-dependent. But as the following discussion shows, this dependence in semiconducting nanotubes is relatively weak.

In Section 3.3, the deformation potential D is assumed to be a constant value disregarding nanotube chirality. Let's see if that is valid. T. Ando (Suzuura and Ando 2002; Ando 2005) theoretically studied the electron couplings to different modes of phonons and gave the interaction Hamiltonian as

$$\begin{pmatrix} V_1 & V_2 \\ V_2^* & V_1 \end{pmatrix} \quad (\text{B.1})$$

where $V_1 = g_1 (\partial u_x / \partial x + \partial u_y / \partial y)$ and $V_2 = g_2 \exp(3i\eta) (\partial u_x / \partial x - \partial u_y / \partial y + \partial u_x / \partial y + i \partial u_y / \partial x)$ with u being the displacement and η as the chiral angle. The x direction is along the circumference and the y direction is along tube axis. The coupling constant g_1 and g_2 is estimated to be on the order of ~ 30 eV and ~ 2 eV. The off-diagonal terms are much smaller in magnitude.

The normalized electron wavefunction in nanotubes can be written as

$$F(\mathbf{r}) = \frac{1}{\sqrt{L\pi d}} F_{snk} \exp[ik_v(n)x +iky] \quad (\text{B.2})$$

$$F_{snk} = \frac{1}{\sqrt{2}} \begin{pmatrix} sb_v(n,k) \\ 1 \end{pmatrix} \quad (\text{B.3})$$

$$b_v(n,k) = \frac{k_v(n) - ik}{\sqrt{k_v(n)^2 + k^2}}. \quad (\text{B.4})$$

Here s equals +1 for the conduction band and -1 for the valence band. n is the subband index and $k_v(n) = 2(n-v/3)/d$ is the wavevectors long tube circumference. In metallic tubes, $k_v(n) = 0$ for the first subband. In semiconducting tubes, $k_v(n)$ is the bandgap divided by $2\hbar v_F$.

The wavefunction looks complicated, but it is actually simple. It is a plane Bloch wave. The variable $b_v(n,k)$ gives the phase difference between the electron wavefunctions at the two carbon atoms in a unit cell. For the first subband in a metallic tube, $k_v(n) = 0$, the wave function is

$$F(\mathbf{r}) = \frac{1}{\sqrt{L\pi d}} \exp[iky] \frac{1}{\sqrt{2}} \begin{pmatrix} -is(k/|k|) \\ 1 \end{pmatrix}. \quad (\text{B.5})$$

Then the matrix element of the phonon-electron scattering is proportional to

$$\begin{pmatrix} is \\ 1 \end{pmatrix}^+ \begin{pmatrix} V_1 & V_2 \\ V_2^* & V_1 \end{pmatrix} \begin{pmatrix} -is \\ 1 \end{pmatrix} = -i \text{Re} V_2 \quad (\text{B.6})$$

This shows that the diagonal terms do not induce scattering in metallic tubes. Only the much smaller off-diagonal terms generate resistance. This effect is due to the Berry phase, or pseudospin, that the electrons carry in nanotubes (Ando et al. 1998; McEuen et al. 1999). In short, the wavefunctions of the left moving and right moving electrons are made of bonding orbital and anti-bonding orbital respectively. Because the long wavelength acoustic phonons cannot change the electronic states at the atomic scale, the transition between left and right moving electrons cannot be induced by them.

The off-diagonal term

$$\text{Re} V_2 = g_2 \left[\left(\frac{\partial u_x}{\partial x} - \frac{\partial u_y}{\partial y} \right) \cos 3\eta - \left(\frac{\partial u_x}{\partial y} + \frac{\partial u_y}{\partial x} \right) \sin 3\eta \right] \quad (\text{B.7})$$

depends on chiral angle η . Indeed the relaxation time of a metallic nanotube is

$$\frac{1}{\tau_\eta} = \frac{1}{\tau_A} \sin^2 3\eta + \frac{1}{\tau_Z} \cos^2 3\eta, \quad (\text{B.8})$$

where τ_A and τ_Z are the relaxation time of an armchair and a metallic zigzag tube of the same diameter.

T. Ando (Suzuura and Ando 2002) pointed out that τ_A and τ_Z are equal when temperature is much higher than the radial breathing mode (RBM) temperature $T_B = \hbar\omega_B / k_B$. In that case, the conductance of a metallic tube does not depend on chiral angle. Figure B.1 shows calculated resistivity as a function of temperature for three nanotubes of different chirality but the same diameter (Suzuura and Ando 2002). At high temperature, the three curves are on top of each other. That means near room temperature, the resistivity of nanotubes is chirality-independent.

In Fig. B.1, the overall decrease of the resistivity with lower temperature is caused by acoustic phonon occupation effect. For low energy long wavelength acoustic phonons, the phonon population is proportional to temperature. But the radial breathing mode phonons, which contribute to scattering in all tubes except armchair tubes, disappear

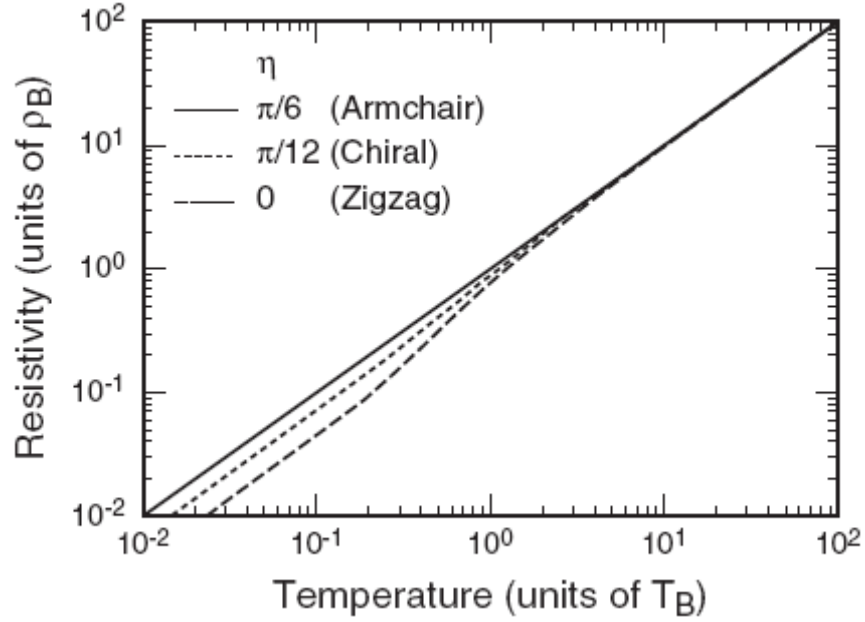


Figure B.1: Calculated resistivity as a function of temperature for three nanotubes with different chiralities (Suzuura and Ando 2002).

rapidly at lower temperature. This is because the dispersion of RBM phonons is not linear. As Fig. B.1 shows, zigzag tubes become slightly better conductors at lower temperature. The difference between the resistivity of armchair tubes and zigzag tubes could reach a factor of two at very low temperature.

For semiconducting nanotubes, the situation is quite different. The matrix element is calculated as

$$\langle s, n, -k | \begin{pmatrix} V_1 & V_2 \\ V_2^* & V_1 \end{pmatrix} | s, n, +k \rangle = \frac{k_v(n)[k_v(n) - ik]}{k_v(n)^2 + k^2} V_1 + \frac{s[k_v(n) - ik]}{\sqrt{k_v(n)^2 + k^2}} \text{Re} V_2. \quad (\text{B.9})$$

Obviously, the much larger diagonal V_1 term dominates at the bottom of the subbands where k is small. Since V_1 is chirality-independent, the matrix element is the same for all nanotubes in that situation. However, as the subband is filled more and more, the importance of V_1 decreases as the factor $k_v(n)/\sqrt{k_v(n)^2 + k^2}$ goes small with

increasing k . That means the chirality dependent off-diagonal term V_2 becomes influential at higher Fermi energies. But as has been shown before, even in metallic tubes, where V_2 term is the only mechanism for back scattering, the resistivity does not depend on chirality at high temperature and only varies by not too much at low temperature. So this can be considered as second order effect.

In conclusion, one can assume, to a certain extent, the resistivity is the same for nanotubes of the same diameter independent of their chirality. The maximum field effect mobility, which is present at intermediate Fermi energy, should depend even less on chirality.

Subbands

In Chapter 3, all calculations are based on electron transport in the lowest subband. However the higher subbands can be filled when more and more electrons are put into nanotubes by electrostatic doping from the nearby gates. It is easy to estimate how quickly the second subband can be reached, disregarding thermal smearing effects.

Using the simplified band structure in which the energy of the second subband bottom is E_g ,

$$\left(\frac{E_g}{2}\right)^2 + (\hbar v_F k)^2 = E_g^2, \quad (\text{B.10})$$

we can get the wavevector at which the second subband is reached,

$$k = \frac{\sqrt{3}E_g}{2\hbar v_F} = \frac{2}{\sqrt{3}d}. \quad (\text{B.11})$$

Assuming the gate capacitance to be 2×10^{-11} F/m, the same value as in our FET devices with 200 nm silicon oxide layer, the second subband is reached at gate voltage

$$V_g - V_t = \frac{12\text{V}}{d[\text{nm}]}. \quad (\text{B.12})$$

For a 3 nm diameter tube, the second subband is reached when gate voltage is 4 V above the threshold. In typical measurements, the gate voltage is swept from -10 V to +10 V. That means there is normally more than one subband filled at high gate voltage.

It is naïve, however, to think that the conductance scales with the number of populated subbands. Figure B.2 plots calculated conductance as a function of carrier density for two tubes (Pennington et al. 2007). It shows that, at small gate voltage, the conductance is slightly lower when multiple subbands are taken into consideration. This is because inter-subband scatterings reduce the electron relaxation time. The differences between the cyan curves (single subband) and red/black curves (multiple subbands) in Fig. B.2 are merely a scaling factor close to 1, demonstrating that it is not a bad approximation to consider only one subband. On top of that, the current theories on multiple subbands conductance do not include the contact effects. In principle, because of the higher energy of the higher subbands, there could be strong Schottky barriers between the contact metal and the higher subbands, generating large contact resistances and restricting the conductance through them. Therefore, the higher bands are ignored in Chapter 3.

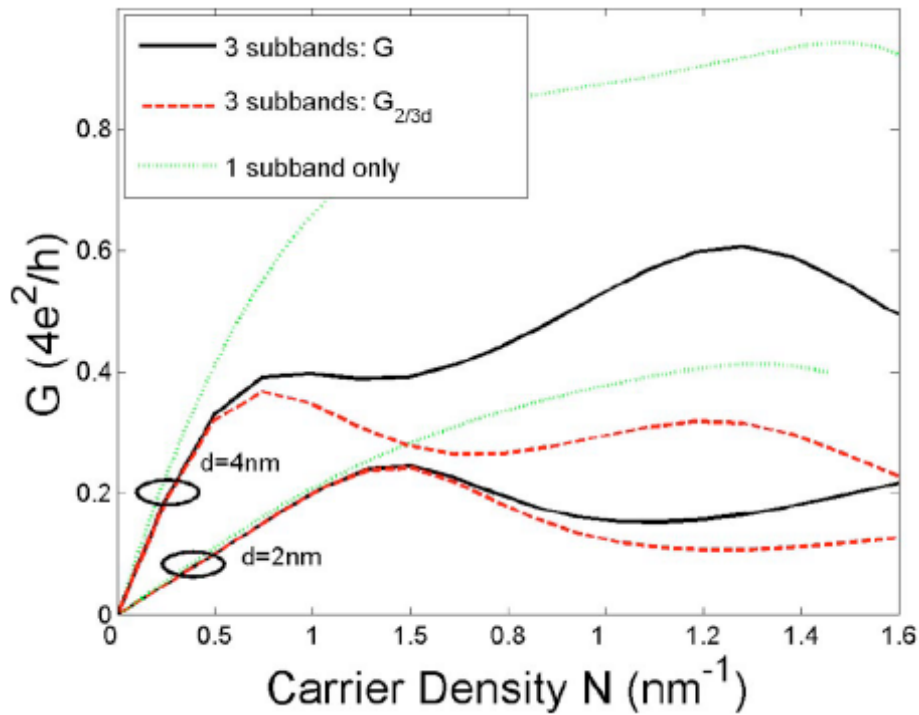


Figure B.2: Theory predicted conductance through 1 (cyan) and 3 (red/black) subbands as a function of carrier density/gate voltage (Pennington et al. 2007).

Another noticeable feature in Fig. B. 2 is that when there are more than one conducting subbands, the conductance is not monotonic when gate voltage is swept. The differential conductance is negative in certain gate voltage range. This is caused by the sudden appearance of many states from a higher subband when the Fermi level is moved close to its bottom. The electrons in the first subband, which initially have high mobility due to a small DOS at the Fermi level, can be scattered into the states in the higher subband. The result is, although the number of electrons is increasing, conductance drops. The tube in Fig 3.2 shows similar behavior at lower temperature and the wiggle happens around the expected gate value where Fermi level reaches the second subband. However there is no other evidence to prove this wiggle is caused by the presence of the second

subband. Further experiments are needed to definitely establish effects of the second and higher subbands.

In short, the approximations taken during the calculations in Sections 3.2-3.4 do not affect the grand picture. They are valid to certain extent as discussed in this appendix.

APPENDIX C

FUNCTIONALIZATION OF NANOTUBES WITH DNA

The discussion in Section 5.1 shows why nanotubes are an interesting candidate as biological sensors. This idea led to the demonstration of nanotube DNA and protein sensors based on charge sensing in the early stage of this field. Here in this appendix, I will show the motivation and our initial results on functionalizing nanotubes with DNA, in route to use them as biosensors. We believe our scheme has a few unique advantages.

Motivation

Here are a few examples of why electronic based DNA and protein sensors are highly desired. Many diseases are genetic. In other words, they are encoded in a person's DNAs from the very moment this person is conceived. One possible way to prevent a person from genetic disease is to find out the potential threats early and prevent them long before the person becomes a patient. This requires DNA sequencing or sensing to detect known segments of DNA sequence responsible for diseases. Currently this process is slow and requires labeling DNAs with fluorescence tags. The proposed charge-based sensing can lead to easier, faster and parallel detection for high throughput.

In some sense the protein sensors are even more important. When a disease is developed in a patient, certain characteristic proteins are produced and can be utilized as diagnoses indicators. However, the amount of proteins is tiny at the early stages and, unlike DNA, proteins can not be amplified. This requires protein sensors to have very high sensitivities. In principle, the proposed nanotube sensors can reach these goals.

Specificity is required in electronic biosensors

In order to achieve any practical significance, the electronic biosensors need to have specificity. But electrostatic interaction, which electronic biosensors base on, is quite generic. Any charged molecules bound to the nanotubes in these sensors due to certain reason would perturb the local environment and may generate false signals. The specificity needs to come from the molecular reorganization developed by Mother Nature during billions of years of evolution. That requires functionalizing nanotubes with receptors that allows only the targets to bind to this complex. In the case of DNA, the receptor attached to nanotubes could be a single strand DNA complementary to the targeted DNA. For proteins, it can be a compound or another protein acting as the receptors.

The current status of nanotube biosensors and our proposal

One of the very best properties of nanotubes turns out to be a big obstacle for functionalization: the fact that a SWNT is just one layer of carbon atoms. Most functionalizations start with generating functional chemical group on the surface. That will introduce defects in nanotubes and degrade their electrical properties. The problem was solved by non-covalent functionalization with a linker molecule designed by Dai group at Stanford (Chen et al. 2001). The pyrene group on the linker molecule, 1-pyrenebutanoic acid, succinimidyl ester (Molecular Probes, Inc., USA) shown in the upper left corner of Fig. C.1, binds to the sidewall of nanotubes due to π - π stacking and hydrophobic interaction in aqueous solutions. The other side of the link, succinimidyl ester, readily reacts with primary amine group.

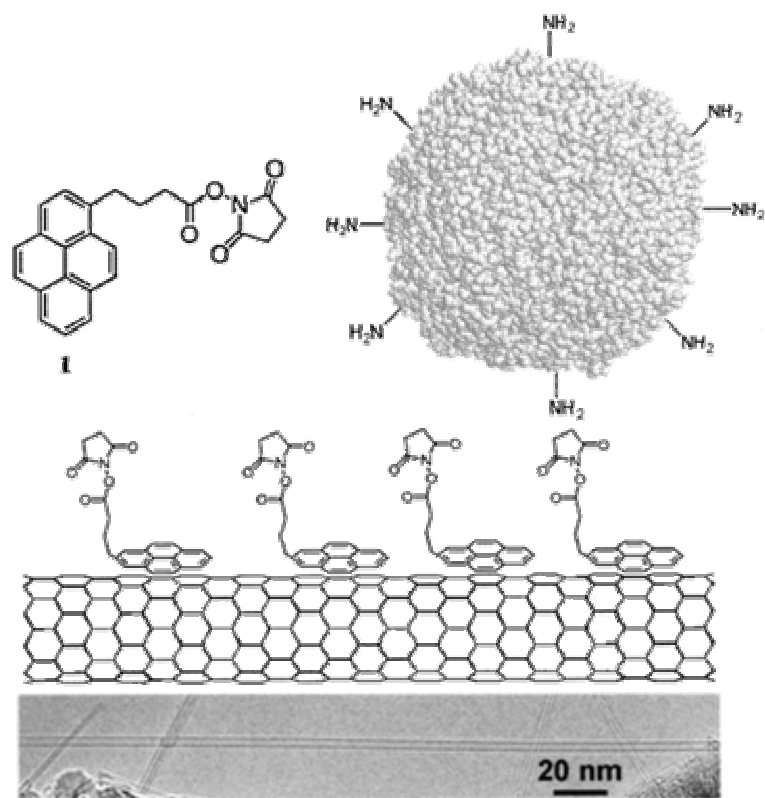


Figure C.1: Functionalization of nanotubes with PASE (Chen et al. 2001).

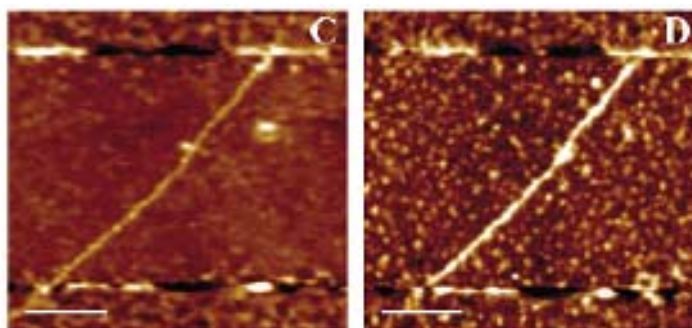


Figure C.2: AFM images taken before (**left**) and after (**right**) attaching glucose oxidase onto nanotubes (Besteman et al. 2003).

Since there are primary amine groups in the amino acid residues, *e.g.* lysine, proteins are naturally rich in amine groups and can form covalent bonds with the linker molecules. Several groups have successively absorbed proteins onto nanotubes using this technique and detected these events as a change in conductance. Dekker group at Delft (Besteman et al. 2003) attached an enzyme called glucose oxidase to nanotubes, with the PASE linker, and detected glucose using these complexes. Gr ner group at UCLA (Star et al. 2003) deposited a polymer layer on top of nanotubes and functionalized the polymer with biotins. The complex was then used to detect streptavidins, which strongly bind to biotins. The mechanism of the observed electrical signals is disputed over whether the signal comes from electrostatic gating, charge transfer or change of capacitance.

The bad thing about the above experiments is that proteins only show up as globular objects under atomic force microscope (AFM). Therefore it is hard to confirm these features are indeed proteins in stead of other contaminations. In Fig. C.2, it can be clearly seen that, after functionalizations, there are many blobs on the substrate far way from the nanotube. It makes one wonder if the coating on nanotubes is really specific. Another problem with the current experiment scheme is that it is hard to confirm the electrical signals, which are merely conduction changes.

Due to the above reasons we started to make our version of DNA sensors using similar technique but with a few unique advantages. First, we wanted to attach DNAs longer than 1000 base pairs to nanotubes. These DNAs are so long that they show up in AFM as linear features. Second, by attaching only the ends of DNAs to nanotubes, it is possible to drive them close to or away from nanotubes with electrical potentials. By doing these operations, the electrostatic coupling between nanotubes and DNAs are modified, which should generate well-controlled signals as a way to confirm the presence of linear charged molecules. Unfortunately the second part was never tried out due to

timing issues. But the functionalization part was successful, and that's going to be discussed here.

Fabricating DNAs with modified ends

The first task is to have DNAs with primary amine groups at the ends. Short strand DNAs that are terminated with all kinds of common chemical groups are commercially available. But the problem is they are short, typically only up to 50 base pairs. This is because the yield of making these DNA strands decreases exponentially with increasing length. In order to have DNAs easily identifiable in AFM, we want to have DNA longer than 200nm when fully stretched. In other words, the DNAs need to be more than 600 base pairs long.

This was solved by elongating the short strand DNAs using polymerase chain reaction (PCR) (Saiki et al. 1985). PCR is typically used to amplify DNAs (to make multiple copies of a certain part of DNAs). I will try to explain how it works in three shot paragraphs.

Naturally cells use a protein called DNA polymerase to duplicate DNAs. In PCR, a number of DNA polymerase proteins are put into the reaction chamber together with copious amount of nucleotide A,T,C,G. The DNA that is waiting to be amplified is called the template. The segment of DNA that is going to be copied is determined by two short strands of DNA called primers, which match the sequence of the ends of the DNA segment of interest. In short, the reaction chamber is filled with DNA polymerase, the template, the primers and a supply of A, T, C, G.

PCR is a cyclic process. Each cycle starts with heating the chamber to around 94 degree Celsius for the double strand DNAs to separate and for the polymerase proteins to terminate their work and get off the template. Then the temperature is lowered to a sweet spot where the primers can bind to single strand DNA templates. Then temperature is

raise to 72 degree Celsius for polymerases to work most efficiently to make copies of the templates. Polymerase works really fast and can make around 1000 base pairs in one minute. After a short period of time, determined by the template length, temperature is raised to 94 degree Celsius and a new cycle starts. The cycle is repeated many times to get huge numbers of the specific DNA sequence needed. The amount of product grows exponentially with numbers of cycles.

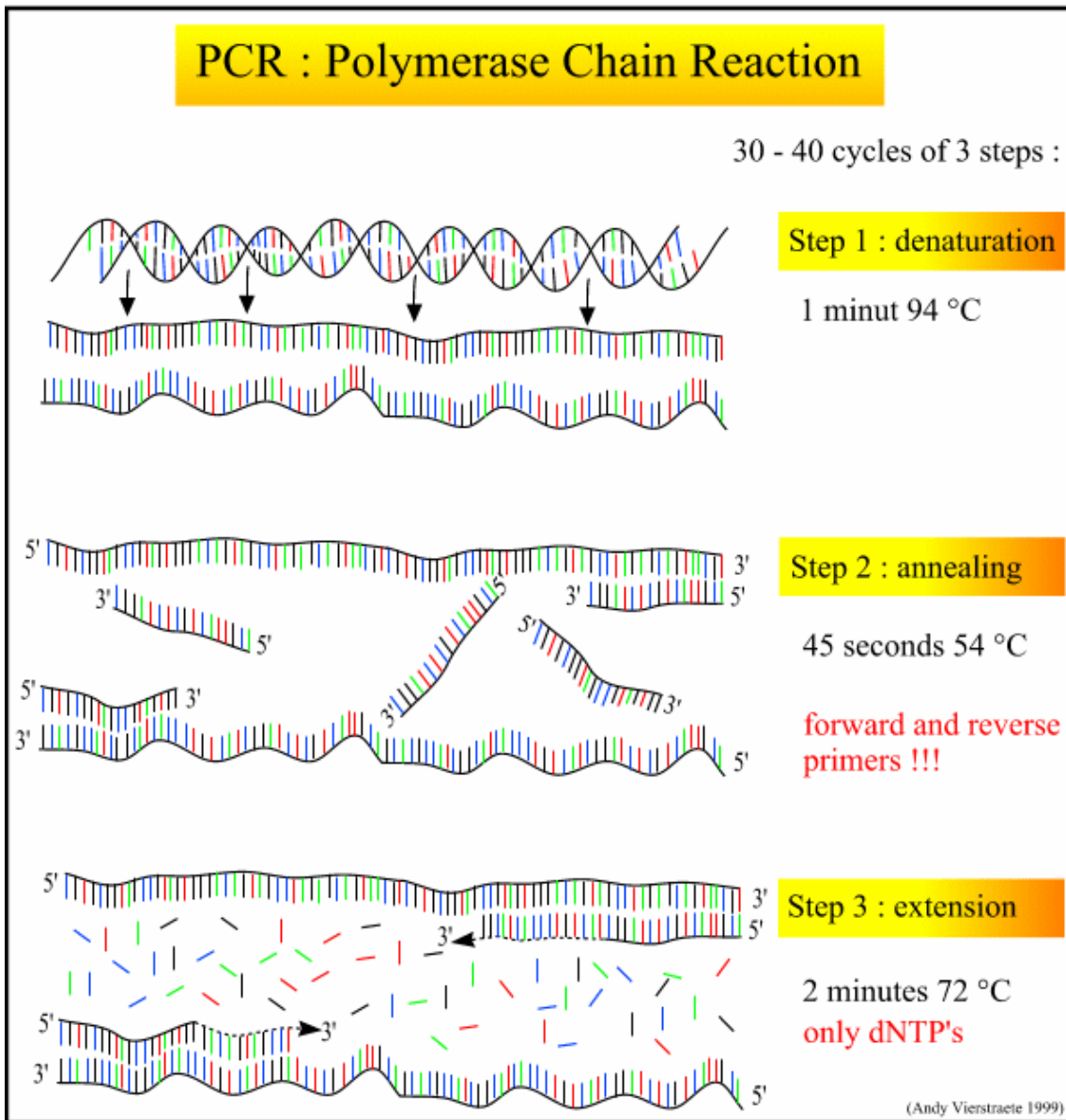


Figure C.3: Schematic of PCR cycles (users.ugent.be/~avierstr).

Since we do not care about the DNA sequence, we randomly chose lambda DNA as our template. Standardized computer programs helped to choose a segment of lambda DNA as our target and extracted the sequence of corresponding primers. The primer selection is crucial to ensure the amplified DNA strands would not form secondary structures like hairpins with themselves. We chose our final single stranded DNA to be around either 1000 or 2000 bases long. The primers of the right sequence for our purpose, with amine-modified ends, were bought from Integrated DNA Technologies (idtdna.com), and the lambda DNA was bought from New England Biolabs (neb.com). The PCR was carried out successfully. This was confirmed with gel electrophoresis to measure the length and purity of our final products.

Putting DNAs onto nanotubes

At this point, DNAs of sufficient length and modified with amine groups at the ends were made. There were four kinds of them: 1000 base pairs long or 2000 base pairs long, one end functionalized with amine or both ends. The next step would be to put them on the sidewalls of nanotubes using the PASE linker.

This can be done in two different methods. One method starts with putting PASE on nanotubes first. This is done by putting a droplet of PASE in dimethylformamide (DMF) on a silicon chip with nanotubes on top, and letting them incubate for 10 minutes. After DMF is blow dried, another droplet of DNA solution in water is put on the silicon chip and the complex is incubated for over night (this time scale can be significantly decreased). Another method starts with mixing a small amount of PASE in DMF with DNA water solution, and let nanotube chips incubate with this mixture solution. Because succinimidyl ester group is not very stable in water due to hydrolysis, the PASE-DNA water solution degrades quickly and should be discarded after each run.

The two methods both worked in the end. But all the initial trials failed. It turned out this was due to a tiny experimental detail: the buffer solution. The standard buffer for DNAs is TAE (Tris-acetate-EDTA). The name is an acronym of acronyms. The result is even biologists do not know what it is. As a physics student, I had the privilege of being totally ignorant, and had to learn everything from scratch. It turned out the full name of Tris is trishydroxymethylaminomethane and it has amino group in its formula. Although it is not primary amine, but we suspected that it still reacts with PASE. The PCR was carried out once again to make DNAs in PBS buffer solution. Then everything started to work out nicely.

Figure C.4 shows two AFM images of the result of successful functionalization. In the image on the left, a 2000 base pairs long DNA strand is doubly clamped onto a nanotube because both ends of this DNA were modified with amine groups. The length of DNA is around 700 nm, which agrees nicely with the number of base pairs. In the image on the right, 1000 base pairs long DNAs modified on one ends were attached onto two crossing nanotubes. This illustrates how densely the DNAs can pack together. The reason why all the DNAs are pointing the same direction is not known, and could be due to the way the solution was dried with a nitrogen stream.

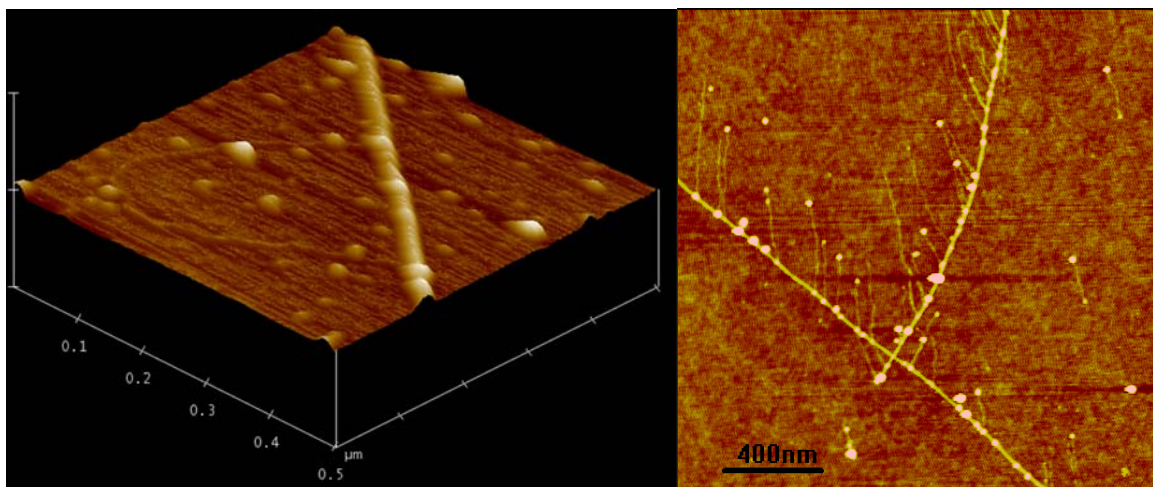


Figure C.4: AFM images of DNAs attached onto nanotubes.

If one argues whether the linear features in these images are really DNAs, it can be proven that they are at least insulating and thus cannot be nanotubes, the only other linear objects in the system. This was done using a scanned probe technique (Bockrath et al. 2002). The left side image of Fig. C.5 is a normal AFM topography image showing a DNA singly-clamped onto a nanotube. The right one is the phase image when a voltage potential is applied between the AFM cantilever and the conducting silicon substrate. Because the cantilever and the substrate form a capacitor, the voltage difference will create an electrostatic force on the cantilever, the magnitude of which depends on the capacitance. When the cantilever is on top of a conducting nanotube, the original capacitor is broken down into two capacitors in series. This inevitably changes the total capacitance, modifies the electrostatic force on the cantilever and generates a phase shift. That is why the nanotube produces a strong feature in the right figure. The other linear feature in the topography image, however, does not generate any changes in the phase image, thus confirming it is an insulator as DNAs should be.

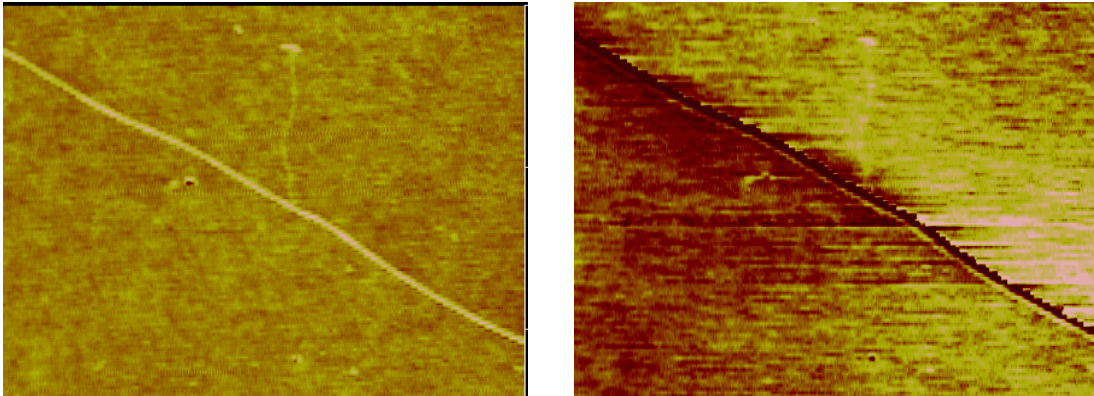


Figure C.5: Topography (**left**) and phase (**right**) image of a nanotube/DNA complex.

It has been reported that single-stranded DNA can wrap around nanotubes and make them water soluble (Zheng et al. 2003). My collaborator, Sonny Mark, successively repeated the experiments with nanotube powders. But clearly the DNAs were not warping the tubes in Fig. C.4. This could be due to that nanotubes are sitting on solid substrates in our experiments. And maybe the DNA wrapping requires strong sonications to work, as what is done in the original report (Zheng et al. 2003).

This functionalization did not work on nanotubes that had been integrated into FET geometry (all the images shown above were taken on nanotubes that were freshly grown without further processing). This is attributed to surface contaminations from photolithography. Later, the piranha cleaning method was found to be able to eat away the contaminations. But due to timing issue, the project had to stop prematurely. But the experience was not wasted. Dr. Jun Zhu attached gold nano particles onto nanotubes in FET geometry with similar techniques. And further DNA sensing experiments can continue based on the functionalization techniques. DNA sensors made from nanotubes have been demonstrated (Star et al. 2006). But the experiment was not quite convincing (Tang et al. 2006). Again, with DNAs attached to nanotubes like shown in Fig. C.4, one can do many manipulations to confirm the electrical signals and extract more information. This scheme can still be used to explore many new phenomena.

APPENDIX D

ELECTRODE KINETICS IN SOLUTION

The research in Chapter 5 involves nanotubes working in aqueous solution. The potential difference between nanotubes and solutions is used to control the doping of nanotubes. Electrical field distributes in solution are very different than in solid state conductors. A few new concepts need to be familiarized to get the correct picture.

Voltage distribution

The major difference between electrolytes and solid state conductors is there is no free electron in electrolytes. Instead the charges are carried by mobile anions and cations in solutions. Charges can transfer between electrodes, immersed in solutions, through chemical reactions only.

When electrodes are put into solutions, they can be categorized into two kinds: reactive electrodes and inert electrodes. The reactive electrodes can react with the solution to allow charge transfer in a circuit under a small voltage bias. On the other hand, there is no chemical reaction between solutions and inert electrodes. We will discuss inert electrodes only. Under a small bias, all charges stay on their own side of the fence. Electrons cannot jump out the inert electrodes! There is almost no DC current flowing through the electrodes. But there is capacitive coupling, which means ions can be attracted to the electrodes when a potential difference is applied. Under larger bias, there will be chemical reactions even if the electrodes are inertial. That is because at large voltage the H^+ , OH^- and other ions can be reduced or oxidized on the electrodes, in other words to exchange electrons with the electrodes. Although electrons go through the electrodes in these reactions, the electrodes themselves do not change their composition and the masses of them remain constant.

The above discussion means the resistance between two inert electrodes immersed into solutions with a normal ionic strength mostly comes from ‘contact’ resistance. This is why the resistivity of a solution can only be correctly measured with AC voltage. Of course this statement becomes wrong when the solution becomes really resistive (with very few ions in it). Other than that, most of the electrostatic potential drops at the two electrodes interfaces. How the whole potential is split between the two electrodes is determined by their capacitances with the solution since it is basically a circuit of two capacitors in series. In electrochemistry experiments, the cyclic voltammetry is carried out with three electrodes. One is called reference electrode, whose purpose is to control the potential of solution to a well defined value. Then the potential drop at the working electrode is controlled.

In our experiments, nanotubes are grounded with a small bias across. A potential is applied through a gold wire immersed solutions. We think most of the potential is dropped at the nanotube-solution interface because of the huge size difference between nanotube and macroscopic gold wire (the capacitance grows with surface area). In the next section, the capacitance between electrodes and solutions is calculated. It also explains why nanotube FETs can be gated so efficiently in solutions.

Capacitance

a. Helmholtz model

If a voltage difference is applied on a piece of metal, a DC current is induced. But if a voltage is applied to an electrolyte with inert electrodes, what will happen? The simplest model is Helmholtz model (Albery 1975): the ions attracted toward the electrodes are lined up in the solution at a fixed distance x_H away from the electrode as showed in Fig. D.1a. In this way a capacitor is formed. The potential between the electrode and bulk solution induces charges on both side. The excess electrons or

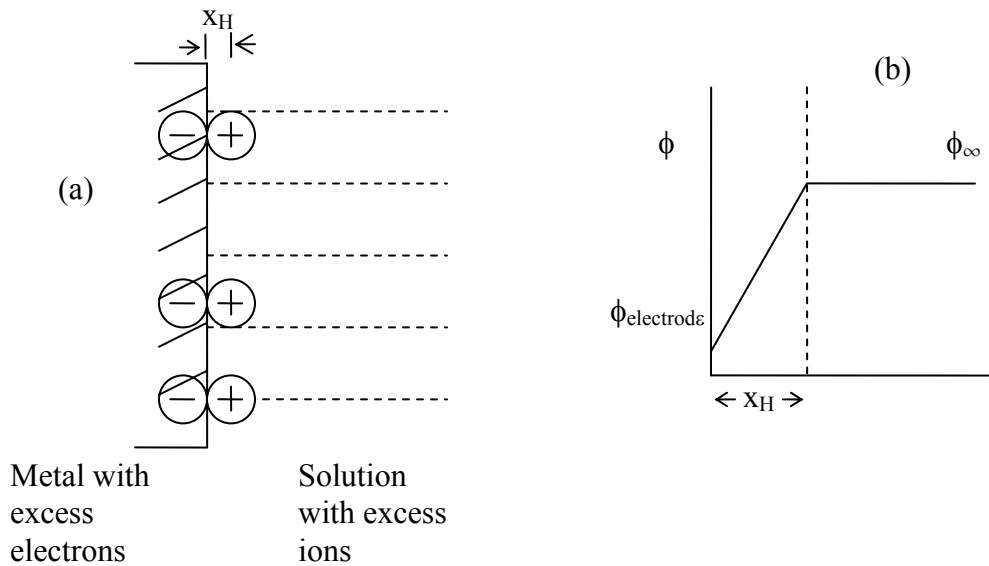


Figure D.1: (a) Helmholtz model of double layers. (b) The profile of potential ϕ perpendicular to the plane electrode.

vacancies near the surface of the electrode are balanced by an equal number of ions in the solution. In the region close to the electrode, the electro-neutrality breaks down. x_H is governed by the hydration spheres of the ions. If $x_H = 0.6 \text{ nm}$, $C_H = \epsilon \epsilon_0 / x_H = 10 \text{ } \mu\text{Fcm}^{-2}$. Because of the high electric field in this layer, ϵ used in the estimation is 7 as compared to the value of bulk water 80. The potential drops in this capacitor as shown in Fig. D.1b.

b. Debye-Huckel model

Helmholtz model completely neglects the thermal energy of the ions. The ions pay extra free energy to line up near electrodes because of entropy. The Debye-Huckel theory takes this effect into consideration and gives a different picture. For simplicity, suppose the electrode is planar. Then the variation of the potential, as well as the ion distribution, in the direction x perpendicular to the electrode can be calculated.

Let's define $\phi' = \phi - \phi_{\infty}$, where ϕ is the potential of the solution and ϕ_{∞} is the potential at infinite distance away from the electrode in the bulk solution. $\phi'(0)$ is the potential

difference between the electrode and the bulk solution right at the interface, and $\phi'(\infty)$ is zero. The Poisson equation describes the relation between the ion distribution and the potential drop as

$$\frac{\partial^2 \phi'}{\partial x^2} = \frac{-\rho(x)}{\varepsilon \varepsilon_0}. \quad (\text{D.1})$$

The total charge at distance x is a results of all the kinds of ions:

$$\rho(x) = \sum_i z_i |e| N_i(x) = \sum_i z_i e N_i(x) \quad (\text{D.2})$$

where the i th type of ions has charge of $z_i e$ and $N_i(x)$ is the distribution function of i th ions per unit volume. $N_i(x)$ is assumed to obey the Boltzmann distribution

$$N_i(x) = N_i(\infty) \exp\left(-\frac{z_i e \phi'(x)}{k_B T}\right). \quad (\text{D.3})$$

Then we get the so-called Poisson-Boltzmann equation

$$\frac{\partial^2 \phi'}{\partial x^2} = -\frac{1}{\varepsilon \varepsilon_0} \sum_i z_i e N_i(\infty) \exp\left(-\frac{z_i e \phi'(x)}{k_B T}\right). \quad (\text{D.4})$$

Assume the solution is a simple (z, z) electrolyte, which means both anions and cations have z charges. Then

$$\frac{\partial^2 \phi'}{\partial x^2} = -\frac{zeN(\infty)}{\varepsilon \varepsilon_0} \left(\exp\left(-\frac{ze\phi'(x)}{k_B T}\right) - \exp\left(\frac{ze\phi'(x)}{k_B T}\right) \right) = \frac{2zeN(\infty)}{\varepsilon \varepsilon_0} \sinh\left(\frac{ze\phi'(x)}{k_B T}\right). \quad (\text{D.5})$$

Let's define $\theta = \frac{ze\phi'(x)}{2k_B T}$ and $\chi = x / \frac{1}{ze} \sqrt{\frac{\varepsilon \varepsilon_0 k_B T}{2N(\infty)}} = x / x_{DL}$, where x_{DL} is called the Debye screening length. Large ionic strength gives very short x_{DL} . $x_{DL} = 0.3$ nm for a $1M$ (1,1) electrolyte at room temperature. Then the equation can be written as

$$\frac{d^2 \theta}{d\chi^2} = \frac{1}{2} \sinh(2\theta). \quad (\text{D.6})$$

The solution of Eq. D.6 is

$$\theta = 2 \tanh^{-1} \left(\tanh\left(\frac{1}{2}\theta_0\right) \exp(-\chi) \right). \quad (\text{D.7})$$

Since the Poisson-Boltzmann equation is a non-linear differential equation, in most cases there is no analytical solution. In the discussion below, I will use Eq. D.7 as the solution. It should at least quantitatively agree with reality.

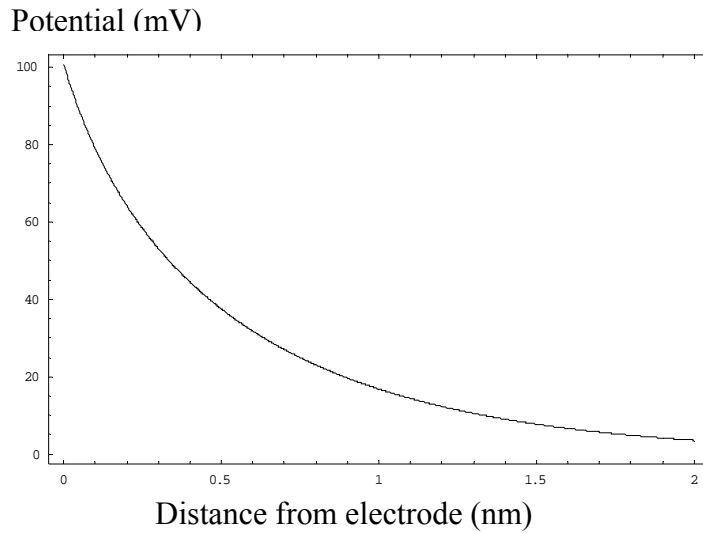


Figure D.2: The potential distribution outside an electrode according to the Debye-Huckel theory.

Suppose the ion concentration of the buffer solution is about 200 mM and the Debye screening length is about $x_{DL} = 0.67 \text{ nm}$. If the potential of the electrode is 100mV higher than the bulk solution, then the voltage near the electrode drops as plotted in Fig. D.2. It is almost an exponential decay.

If we calculate the ions distribution near the electrode, apparently there are excess cations near the cathode and excess anions near the anode. The total excess charges of the ions are equal to that on the electrodes. One interesting phenomenon is in nanometer-scale channels where the geometrical length is on the same order of the diffusive layer thickness, the solution in the channels loses neutrality when the walls are charged. If the surface is negatively charged, only positive ions can enter the channel. This effect has been observed and utilized to sort proteins (Karnik et al. 2006).

We can calculate the capacitance per unit area between electrode and solution. Following Eqs. D.2 and D.7

$$\rho = ze[N(\infty) \exp(-2\theta) - N(\infty) \exp(2\theta)] = -2zeN(\infty) \sinh(2\theta). \quad (\text{D.8})$$

The total charge per unit area is

$$\sigma = \int_0^{\infty} \rho dx = -2x_{DL} zeN(\infty) \int_0^{\infty} \sinh(2\theta) d\chi = -4x_{DL} zeN(\infty) \sinh(\theta_0). \quad (\text{D.9})$$

Then the capacitance per unit area is

$$C = -\frac{dq}{d\phi'} = zN_A e \sqrt{\frac{2\varepsilon\varepsilon_0 c_\infty}{RT}} \cosh\left(\frac{ze\phi'_0}{2k_B T}\right) \quad (\text{D.10})$$

where N_A is the Avogadro's constant and c_∞ is the ion concentration of bulk solution in the unit of mol m^{-3} or mM.

$$C = 0.072 c_\infty^{1/2} \cosh(19.8\phi'_0) \quad (\text{D.11})$$

The capacitance almost grows exponentially at high bias. Fig. D.3 plots the capacitance per unit area according to different models.

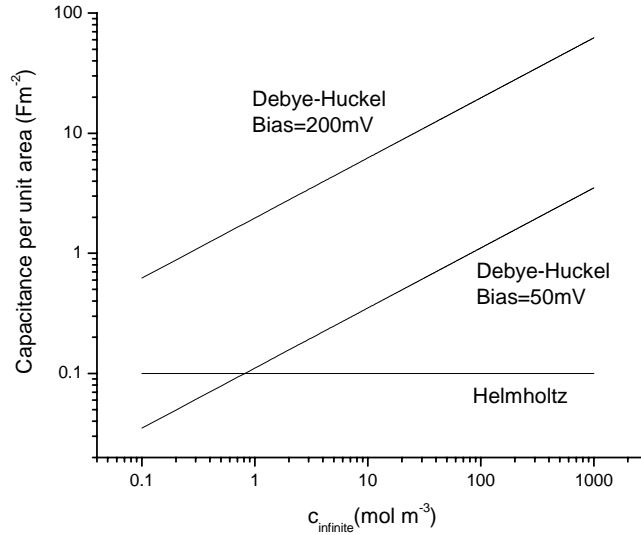


Figure D.3: The capacitance per unit area according to different models.

c. Combining the two model

The Debye-Huckel model can give unrealistic result because it does not take the size of the ions into consideration. For example, it may require huge amount of ions to stay within the hydration sphere radius away from the electrode. It is unrealistic. So the best way to describe the situation is to combine both the Helmholtz layer and the diffusive layer. Which one is more important is determined by their capacitance, and the one with less capacitance dominates since they can be considered as two capacitors in series. From Fig. D.3 we can see that Helmholtz capacitance is always smaller unless the ion concentration is very small and the bias is small too. So when the ion concentration is high, most of the voltage drops across the Helmholtz layer. When the ion concentration is extremely low and the bias is small, the diffusive layer is important. It makes sense since when there are very few ions in the solution, the entropy they pay to line up near the electrode is huge. So diffusion wins in this situation. Anyway, the capacitance per unit area cannot exceed 0.1 Fm^{-2} .

The research done in my group (Rosenblatt et al. 2002) shows nanotube FETs have almost the same response to solution potential at different ion concentrations, from 1 mM to 1 M. In other words, the gate coupling between the solution and the nanotubes does not depend on ion concentration at these levels. If only Debye-Huckel theory is considered, the capacitance should grow with ion concentration. So probably Helmholtz layer is dominating in these cases.

But another explanation, which does not acknowledge the Helmholtz layer, is that there is a constant quantum capacitance in series with the diffusive layer capacitance. Since the quantum capacitance is much smaller, the whole capacitance is fixed by it although the diffusive layer capacitance is changing.

From Helmholtz model, the unite length capacitance between 1nm diameter tube and water is about $0.1 \text{ Fm}^{-2} \times \pi \times 1 \text{ nm} = 3 \times 10^{-10} \text{ Fm}^{-1}$. The quantum capacitance is about $4 \times 10^{-10} \text{ Fm}^{-1}$ (Rosenblatt et al. 2002). They are on the same order. It's difficult to

distinguish whether the whole capacitance is fixed by quantum capacitance or by the Helmholtz layer capacitance. One experiment to test the existence of the quantum capacitance is to make really good coupling between tube and a solid state gate with a very thin insulating layer that has high dielectric constant to see if the coupling can be higher than the quantum capacitance.

Surface potential

The streptavidin detection experiment using nanotube/SLB hybrids in Chapter 5 can also be explained by surface potential change. When streptavidins bind to the biotins in the bilayer, they add a layer of surface charge and thus a potential change.

Since the experiment was carried in low ionic strength buffer, we will use Debye-Huckel model. Equation D.9 shows the relationship between a surface potential induced by a surface charge to its charged density. The data in Section 5.5 shows the binding events generate a threshold shift of about 80 mV. According to Eq. D.9, that corresponds to a charge density of about $5.2 \times 10^4 \text{ e}/\mu\text{m}^2$. This is slightly larger than the charge density estimated in Section 5.5. Actually the equation used in Section 5.5, $\sigma = 2\Delta V_e \epsilon_w \epsilon_0 / \lambda_d$, is an approximation version of Eq. D.9. When x is small, $\sinh(x)$ approaches x and the two equations become equivalent. This discussion here helps to capture the essence of the sensing mechanism.

In conclusion, the potential distribution in solution is discussed in this appendix. The capacitance between electrodes and solutions is calculated and showed that it behaves differently in solutions with different ion concentrations. The surface potential associated with surface charges is also presented. These discussions are helpful to understand the experiments involving nanotubes in solution.

APPENDIX E

DIMENSIONALITY OF NANOTUBES AND OUR UNIVERSE

Suppose when SWNTs are first discovered, people only have lousy SEMs. People see SWNTS as linear features in SEM images but cannot figure out whether they are one-dimensional lines or two-dimensional tubes/stripes because the features are as wide as their probing electron beam. People do not know the dimensionality of SWNTs.

When people first study the electrical properties of nanotubes (for now, suppose they only have one species of tubes), they discover a new fundamental particle. The particle carries one electron charge, but its mass is much smaller than electron rest mass. The momentum of these particles only can only be along the tube axial direction, either pointing one way or the other. Therefore, people conclude that SWNTs are one-dimensional.

However, the next day people build a high energy collider and discover a new particle in nanotubes. It has double the mass of the first particle, but the same electron charge. Theorists predicate there are heavier particles, and they are consequently discovered in the collider. But the masses of these high energy particles follow a unique pattern of 1,2,4,5,6,7... times the smallest mass unit (refer to Chapter 2). No one can explain this phenomenon, and it becomes known as “the God’s hatred of three”.

One day people obtain more powerful tools that can resolve nanometer details. Then it becomes apparent that SWNTs are not really one-dimensional. Instead they are two dimensional tubes with one of the dimensions much smaller than the other and rolled up to itself. People also figure out that the mass of the fundamental particles are determined by how real electrons circle the circumference. The pattern in particle masses is a result of atomic details along the circumference.

Just when people think all the mysteries have been solved, they discover other nanotubes that have fundamental particles of different unit masses. With the help of high resolution TEM, they find out this is due to the size of the rolled-up second dimension, or the tube diameter. In conclusion, with high resolution imaging tools and high energy colliders, people figure out the exact spatial nature of nanotubes, discover a new dimension and learn how the masses of the previously observed particles come from the property of the smaller dimension.

We, in reality, are living in a situation similar to the one described in the first few paragraphs. We know the fundamental particles of this universe and have a pretty theory to phenomenologically describe the interaction between them, but the theory cannot explain the origin of masses, charges and spins carried by these particles.

Then there comes string theory. Up to today it has not generated experimental-testable predictions. But the internal beauty and the astonishing insight of the universe it brings along make it an attractive, and almost the only, theory that are being studied by the best theoretical high energy physicists.

I read a popular string theory book targeted at general audience, “The Elegant Universe: Superstrings, Hidden Dimensions, and the Quest for the Ultimate Theory” by Brian Greene, as I was writing this thesis. I could not help but notice how nanotubes are similar to the space fabrics described in string theory. In string theory, the world has more than the normal 3(space) + 1(time) dimensions. The extra six or seven dimensions are very small and wrapped, just like the circumferential dimension of nanotubes but in much more complicated forms. The masses of the fundamental particles arise from how strings oscillate around these complicated wrapped dimensions. Basically, everything we see in the universe, particles and forces, comes from the detailed fabrics of the universe. Furthermore, there is no reason that the fabrics of our universe, or how the small dimensions twist and wrap, are unique just like nanotubes come in different diameters

and chiralities. We should not be surprised one day to see parallel universes where the physical phenomena are quite different from ours.

In conclusion, one should not ignore or refuse to accept string theory, although it may not be the ultimate theory or even correct. After all, it is beautiful and attractive to generations of physicists. I could not wait to see the real structure of our universe. The Large Hadron Collider (LHC) being build at CERN may shed some light on it (Randall 2007) very soon.

REFERENCES

- Ajo-Franklin, C. M., C. Yoshina-Ishii and S. G. Boxer (2005). Probing the structure of supported membranes and tethered oligonucleotides by fluorescence interference contrast microscopy. *Langmuir* **21**(11): 4976-4983.
- Akeson, M., D. Branton, J. J. Kasianowicz, E. Brandin and D. W. Deamer (1999). Microsecond time-scale discrimination among polycytidylic acid, polyadenylic acid, and polyuridylic acid as homopolymers or as segments within single RNA molecules. *Biophysical Journal* **77**(6): 3227-3233.
- Alberts, B., A. Johnson, J. Lewis, M. Raff, K. Roberts and P. Walter (2002). *Molecular biology of the cell* New York, Garland Science.
- Albery, W. J. (1975). *Electrode kinetics*. Oxford, Clarendon Press,.
- An, L., J. M. Owens, L. E. McNeil and J. Liu (2002). Synthesis of nearly uniform single-walled carbon nanotubes using identical metal-containing molecular nanoclusters as catalysts. *Journal of the American Chemical Society* **124**(46): 13688-13689.
- Ando, T. (2005). Theory of electronic states and transport in carbon nanotubes. *Journal of the Physical Society of Japan* **74**(3): 777-817.
- Ando, T., T. Nakanishi and R. Saito (1998). Berry's phase and absence of back scattering in carbon nanotubes. *Journal of the Physical Society of Japan* **67**(8): 2857-2862.
- Angstrom, J., S. Teneberg and K. A. Karlsson (1994). Delineation and Comparison of Ganglioside-Binding Epitopes for the Toxins of *Vibrio-Cholerae*, *Escherichia-Coli*, and *Clostridium-Tetani* - Evidence for Overlapping Epitopes. *Proceedings of the National Academy of Sciences of the United States of America* **91**(25): 11859-11863.

- Arnold, M. S., A. A. Green, J. F. Hulvat, S. I. Stupp and M. C. Hersam (2006). Sorting carbon nanotubes by electronic structure using density differentiation. *Nat Nano* **1**(1): 60-65.
- Artyukhin, A. B., A. Shestakov, J. Harper, O. Bakajin, P. Stroeve and A. Noy (2005). Functional one-dimensional lipid bilayers on carbon nanotube templates. *Journal of the American Chemical Society* **127**(20): 7538-7542.
- Artyukhin, A. B., M. Stadermann, R. W. Friddle, P. Stroeve, O. Bakajin and A. Noy (2006). Controlled electrostatic gating of carbon nanotube FET devices. *Nano Letters* **6**(9): 2080-2085.
- Ashcroft, N. W. and N. D. Mermin (1976). *Solid state physics*, New York, Holt, Rinehart and Winston
- Bachilo, S. M., M. S. Strano, C. Kittrell, R. H. Hauge, R. E. Smalley and R. B. Weisman (2002). Structure-Assigned Optical Spectra of Single-Walled Carbon Nanotubes. *Science* **298**(5602): 2361-2366.
- Bachtold, A., M. S. Fuhrer, S. Plyasunov, M. Forero, E. H. Anderson, A. Zettl and P. L. McEuen (2000). Scanned probe microscopy of electronic transport in carbon nanotubes. *Physical Review Letters* **84**(26): 6082-6085.
- Bachtold, A., P. Hadley, T. Nakanishi and C. Dekker (2001). Logic Circuits with Carbon Nanotube Transistors. *Science* **294**(5545): 1317-1320.
- Bardeen, J. and W. Shockley (1950). Deformation Potentials and Mobilities in Non-Polar Crystals. *Physical Review* **80**(1): 72.

- Bernards, D. A., G. G. Malliaras, G. E. S. Toombes and S. M. Gruner (2006). Gating of an organic transistor through a bilayer lipid membrane with ion channels. *Applied Physics Letters* **89**(5): 053505.
- Besteman, K., J. O. Lee, F. G. M. Wiertz, H. A. Heering and C. Dekker (2003). Enzyme-coated carbon nanotubes as single-molecule biosensors. *Nano Letters* **3**(6): 727-730.
- Bockrath, M., N. Markovic, A. Shepard, M. Tinkham, L. Gurevich, L. P. Kouwenhoven, M. S. W. Wu and L. L. Sohn (2002). Scanned conductance microscopy of carbon nanotubes and lambda-DNA. *Nano Letters* **2**(3): 187-190.
- Bonetta, L. (2005). Spectrin is peripheral. *J. Cell. Biol.* **170**(1): 12.
- Bradley, K., A. Davis, J. C. P. Gabriel and G. Gruner (2005). Integration of cell membranes and nanotube transistors. *Nano Letters* **5**(5): 841-845.
- Brian, A. A. and H. M. McConnell (1984). Allogeneic Stimulation of Cyto-Toxic T-Cells by Supported Planar Membranes. *Proceedings of the National Academy of Sciences of the United States of America-Biological Sciences* **81**(19): 6159-6163.
- Brown, D. A. and E. London (1998). Functions of lipid rafts in biological membranes. *Annual Review of Cell and Developmental Biology* **14**: 111-136.
- Chalet, L. and F. J. Wolf (1964). Properties of Streptavidin Biotin-Binding Protein Produced by Streptomycetes. *Archives of Biochemistry and Biophysics* **106**(1-3): 1-5.
- Chen, R. J., Y. G. Zhan, D. W. Wang and H. J. Dai (2001). Noncovalent sidewall functionalization of single-walled carbon nanotubes for protein immobilization. *Journal of the American Chemical Society* **123**(16): 3838-3839.
- Cheung, C. L., A. Kurtz, H. Park and C. M. Lieber (2002). Diameter-controlled synthesis of carbon nanotubes. *Journal of Physical Chemistry B* **106**(10): 2429-2433.

- Collins, P. G., M. S. Fuhrer and A. Zettl (2000). 1/f noise in carbon nanotubes. *Applied Physics Letters* **76**(7): 894-896.
- Datta, S. (1997). *Electronic Transport in Mesoscopic Systems*, Cambridge University Press.
- Dekker, C. (2007). Solid-state nanopores. *Nature Nanotechnology* **2**(4): 209-215.
- Dillon, A. C., K. M. Jones, T. A. Bekkedahl, C. H. Kiang, D. S. Bethune and M. J. Heben (1997). Storage of hydrogen in single-walled carbon nanotubes. *Nature* **386**(6623): 377-379.
- Doorn, S. K., M. J. O'Connell, L. X. Zheng, Y. T. Zhu, S. M. Huang and J. Liu (2005). Raman spectral imaging of a carbon nanotube intramolecular junction. *Physical Review Letters* **94**(1).
- Doyle, D. A., J. M. Cabral, R. A. Pfuetzner, A. L. Kuo, J. M. Gulbis, S. L. Cohen, B. T. Chait and R. MacKinnon (1998). The structure of the potassium channel: Molecular basis of K⁺ conduction and selectivity. *Science* **280**(5360): 69-77.
- Dresselhaus, M. S., G. Dresselhaus, A. Jorio, A. G. Souza Filho, M. A. Pimenta and R. Saito (2002). Single Nanotube Raman Spectroscopy. *Acc. Chem. Res.* **35**(12): 1070-1078.
- Durkop, T., S. A. Getty, E. Cobas and M. S. Fuhrer (2004). Extraordinary Mobility in Semiconducting Carbon Nanotubes. *Nano Lett.* **4**(1): 35-39.
- Edwards, B. C. (2000). DESIGN AND DEPLOYMENT OF A SPACE ELEVATOR. *Acta Astronautica* **47**(10): 735-744.

- Foquet, M., J. Korlach, W. R. Zipfel, W. W. Webb and H. G. Craighead (2004). Focal volume confinement by submicrometer-sized fluidic channels. *Analytical Chemistry* **76**(6): 1618-1626.
- Frye, L. D. and M. Edidin (1970). Rapid Intermixing of Cell Surface Antigens after Formation of Mouse-Human Heterokaryons. *Journal of Cell Science* **7**(2): 319-335.
- Geim, A. K. and K. S. Novoselov (2007). The rise of graphene. *Nature Materials* **6**(3): 183-191.
- Goupalov, S. V. (2005). Chirality dependence of the Raman cross section of carbon nanotubes. *Physical Review B (Condensed Matter and Materials Physics)* **71**(15): 153404.
- Graneli, A., C. C. Yeykal, R. B. Robertson and E. C. Greene (2006). Long-distance lateral diffusion of human Rad51 on double-stranded DNA. *Proceedings of the National Academy of Sciences of the United States of America* **103**(5): 1221-1226.
- Groves, J. T., N. Ulman and S. G. Boxer (1997). Micropatterning fluid lipid bilayers on solid supports. *Science* **275**(5300): 651-653.
- Groves, J. T., C. Wulfing and S. G. Boxer (1996). Electrical manipulation of glycan phosphatidyl inositol tethered proteins in planar supported bilayers. *Biophysical Journal* **71**(5): 2716-2723.
- Hamill, O. P., A. Marty, E. Neher, B. Sakmann and F. J. Sigworth (1981). Improved Patch-Clamp Techniques for High-Resolution Current Recording from Cells and Cell-Free Membrane Patches. *Pflügers Archiv-European Journal of Physiology* **391**(2): 85-100.

- Han, S., X. L. Liu and C. W. Zhou (2005). Template-free directional growth of single-walled carbon nanotubes on a- and r-plane sapphire. *Journal of the American Chemical Society* **127**(15): 5294-5295.
- Hata, K., D. N. Futaba, K. Mizuno, T. Namai, M. Yumura and S. Iijima (2004). Water-Assisted Highly Efficient Synthesis of Impurity-Free Single-Walled Carbon Nanotubes. *Science* **306**(5700): 1362-1364.
- Heinze, S., J. Tersoff, R. Martel, V. Derycke, J. Appenzeller and P. Avouris (2002). Carbon nanotubes as Schottky barrier transistors. *Physical Review Letters* **89**(10): -.
- Heller, I., J. Kong, K. A. Williams, C. Dekker and S. G. Lemay (2006). Electrochemistry at Single-Walled Carbon Nanotubes: The Role of Band Structure and Quantum Capacitance. *J. Am. Chem. Soc.* **128**(22): 7353-7359.
- Huang, S. M., X. Y. Cai and J. Liu (2003). Growth of millimeter-long and horizontally aligned single-walled carbon nanotubes on flat substrates. *Journal of the American Chemical Society* **125**(19): 5636-5637.
- Huang, S. M., M. Woodson, R. Smalley and J. Liu (2004). Growth mechanism of oriented long single walled carbon nanotubes using "fast-heating" chemical vapor deposition process. *Nano Letters* **4**(6): 1025-1028.
- Iijima, S. (1991). Helical Microtubules of Graphitic Carbon. *Nature* **354**(6348): 56-58.
- Israelachvili, J. (1991). *Intermolecular and Surface Forces*. London, Academic Press.
- Javey, A., J. Guo, Q. Wang, M. Lundstrom and H. J. Dai (2003). Ballistic carbon nanotube field-effect transistors. *Nature* **424**(6949): 654-657.

- Javey, A., H. Kim, M. Brink, Q. Wang, A. Ural, J. Guo, P. McIntyre, P. McEuen, M. Lundstrom and H. J. Dai (2002). High-k dielectrics for advanced carbon-nanotube transistors and logic gates. *Nature Materials* **1**(4): 241-246.
- Ji Ung, L. (2007). Band-gap renormalization in carbon nanotubes: Origin of the ideal diode behavior in carbon nanotube p-n structures. *Physical Review B (Condensed Matter and Materials Physics)* **75**(7): 075409.
- Johnson, J. M., T. Ha, S. Chu and S. G. Boxer (2002). Early steps of supported bilayer formation probed by single vesicle fluorescence assays. *Biophysical Journal* **83**(6): 3371-3379.
- Kane, C. L. and E. J. Mele (1997). Size, shape, and low energy electronic structure of carbon nanotubes. *Physical Review Letters* **78**(10): 1932-1935.
- Kane, C. L., E. J. Mele, R. S. Lee, J. E. Fischer, P. Petit, H. Dai, A. Thess, R. E. Smalley, A. R. M. Verschueren, S. J. Tans and C. Dekker (1998). Temperature-dependent resistivity of single-wall carbon nanotubes. *Europhysics Letters* **41**(6): 683-688.
- Karnik, R., K. Castelino and A. Majumdar (2006). Field-effect control of protein transport in a nanofluidic transistor circuit. *Applied Physics Letters* **88**(12): 123114.
- Keren, K., R. S. Berman, E. Buchstab, U. Sivan and E. Braun (2003). DNA-Templated Carbon Nanotube Field-Effect Transistor. *Science* **302**(5649): 1380-1382.
- Khorana, H. G. (1988). Bacteriorhodopsin, a Membrane-Protein That Uses Light to Translocate Protons. *Journal of Biological Chemistry* **263**(16): 7439-7442.
- Kim, H., J. Lee, S. J. Kahng, Y. W. Son, S. B. Lee, C. K. Lee, J. Ihm and Y. Kuk (2003). Direct Observation of Localized Defect States in Semiconductor Nanotube Junctions. *Physical Review Letters* **90**(21): 216107.

- Kim, W., A. Javey, O. Vermesh, O. Wang, Y. M. Li and H. J. Dai (2003). Hysteresis caused by water molecules in carbon nanotube field-effect transistors. *Nano Letters* **3**(2): 193-198.
- Kocabas, C., M. Shim and J. A. Rogers (2006). Spatially Selective Guided Growth of High-Coverage Arrays and Random Networks of Single-Walled Carbon Nanotubes and Their Integration into Electronic Devices. *J. Am. Chem. Soc.* **128**(14): 4540-4541.
- Kodambaka, S., J. Tersoff, M. C. Reuter and F. M. Ross (2007). Germanium Nanowire Growth Below the Eutectic Temperature. *Science* **316**(5825): 729-732.
- Kong, J., N. R. Franklin, C. W. Zhou, M. G. Chapline, S. Peng, K. J. Cho and H. J. Dai (2000). Nanotube molecular wires as chemical sensors. *Science* **287**(5453): 622-625.
- Kong, J., H. T. Soh, A. M. Cassell, C. F. Quate and H. J. Dai (1998). Synthesis of individual single-walled carbon nanotubes on patterned silicon wafers. *Nature* **395**(6705): 878-881.
- Kroto, H. W., J. R. Heath, S. C. O'Brien, R. F. Curl and R. E. Smalley (1985). C-60 - Buckminsterfullerene. *Nature* **318**(6042): 162-163.
- Kruger, M., M. R. Buitelaar, T. Nussbaumer, C. Schonenberger and L. Forro (2001). Electrochemical carbon nanotube field-effect transistor. *Applied Physics Letters* **78**(9): 1291-1293.
- Kusumi, A., H. Ike, C. Nakada, K. Murase and T. Fujiwara (2005). Single-molecule tracking of membrane molecules: plasma membrane compartmentalization and dynamic assembly of raft-philic signaling molecules. *Semin. Immunol.* **17**(1): 3-21.

- Larrimore, L., S. Nad, X. J. Zhou, H. Abruna and P. L. McEuen (2006). Probing electrostatic potentials in solution with carbon nanotube transistors. *Nano Letters* **6**(7): 1329-1333.
- Li, S., Z. Yu, C. Rutherglen and P. J. Burke (2004). Electrical Properties of 0.4 cm Long Single-Walled Carbon Nanotubes. *Nano Lett.* **4**(10): 2003-2007.
- Li, Y. G., Y. D. Tseng, S. Y. Kwon, L. D'Espaux, J. S. Bunch, P. L. McEuen and D. Luo (2004). Controlled assembly of dendrimer-like DNA. *Nature Materials* **3**(1): 38-42.
- Li, Y. M., W. Kim, Y. G. Zhang, M. Rolandi, D. W. Wang and H. J. Dai (2001). Growth of single-walled carbon nanotubes from discrete catalytic nanoparticles of various sizes. *Journal of Physical Chemistry B* **105**(46): 11424-11431.
- Liang, W. J., M. Bockrath, D. Bozovic, J. H. Hafner, M. Tinkham and H. Park (2001). Fabry-Perot interference in a nanotube electron waveguide. *Nature* **411**(6838): 665-669.
- Liu, Z., W. B. Cai, L. N. He, N. Nakayama, K. Chen, X. M. Sun, X. Y. Chen and H. J. Dai (2007). In vivo biodistribution and highly efficient tumour targeting of carbon nanotubes in mice. *Nature Nanotechnology* **2**(1): 47-52.
- Liu, Z. J., G. Yang, Y. Z. Lee, D. Bordelon, J. P. Lu and O. Zhou (2006). Carbon nanotube based microfocus field emission x-ray source for microcomputed tomography. *Applied Physics Letters* **89**(10).
- Lu, J. Q., T. E. Kopley, N. Moll, D. Roitman, D. Chamberlin, Q. Fu, J. Liu, T. P. Russell, D. A. Rider, I. Manners and M. A. Winnik (2005). High-quality single-walled carbon nanotubes with small diameter, controlled density, and ordered locations using a

- polyferrocenylsilane block copolymer catalyst precursor. *Chemistry of Materials* **17**(9): 2227-+.
- Magde, D., E. L. Elson and W. W. Webb (1974). Fluorescence Correlation Spectroscopy .2. Experimental Realization. *Biopolymers* **13**(1): 29-61.
- Magde, D., W. W. Webb and E. Elson (1972). Thermodynamic Fluctuations in a Reacting System - Measurement by Fluorescence Correlation Spectroscopy. *Physical Review Letters* **29**(11): 705-&.
- Mann, D., A. Javey, J. Kong, Q. Wang and H. Dai (2003). Ballistic Transport in Metallic Nanotubes with Reliable Pd Ohmic Contacts. *Nano Lett.* **3**(11): 1541-1544.
- Mathe, J., A. Aksimentiev, D. R. Nelson, K. Schulten and A. Meller (2005). Orientation discrimination of single-stranded DNA inside the alpha-hemolysin membrane channel. *Proceedings of the National Academy of Sciences of the United States of America* **102**(35): 12377-12382.
- McEuen, P. L. (2000). Single-wall carbon nanotubes. *Physics World* **13**(6): 31-36.
- McEuen, P. L., M. Bockrath, D. H. Cobden, Y. G. Yoon and S. G. Louie (1999). Disorder, pseudospins, and backscattering in carbon nanotubes. *Physical Review Letters* **83**(24): 5098-5101.
- Minot, E. D. (2004). Tuning the band structure of carbon nanotubes. Physics Department. Ithaca, Cornell University.
- Minot, E. D., Y. Yaish, V. Sazonova, J. Y. Park, M. Brink and P. L. McEuen (2003). Tuning carbon nanotube band gaps with strain. *Physical Review Letters* **90**(15): 156401.

- Misewich, J. A., R. Martel, P. Avouris, J. C. Tsang, S. Heinze and J. Tersoff (2003). Electrically Induced Optical Emission from a Carbon Nanotube FET. *Science* **300**(5620): 783-786.
- Moran-Mirabal, J. M., J. B. Edel, G. D. Meyer, D. Throckmorton, A. K. Singh and H. G. Craighead (2005). Micrometer-sized supported lipid bilayer arrays for bacterial toxin binding studies through total internal reflection fluorescence microscopy. *Biophysical Journal* **89**(1): 296-305.
- Mossman, K. D., G. Campi, J. T. Groves and M. L. Dustin (2005). Altered TCR signaling from geometrically repatterned immunological synapses. *Science* **310**(5751): 1191-1193.
- Nelson, P. (2004). *Biological Physics - Energy, Information, Life*. New York, W.H. Freeman and Company.
- Ng, J. M. K., I. Gitlin, A. D. Stroock and G. M. Whitesides (2002). Components for integrated poly(dimethylsiloxane) microfluidic systems. *Electrophoresis* **23**(20): 3461-3473.
- Novoselov, K. S., A. K. Geim, S. V. Morozov, D. Jiang, Y. Zhang, S. V. Dubonos, I. V. Grigorieva and A. A. Firsov (2004). Electric Field Effect in Atomically Thin Carbon Films. *Science* **306**(5696): 666-669.
- O'Connell, M. J., S. M. Bachilo, C. B. Huffman, V. C. Moore, M. S. Strano, E. H. Haroz, K. L. Rialon, P. J. Boul, W. H. Noon, C. Kittrell, J. Ma, R. H. Hauge, R. B. Weisman and R. E. Smalley (2002). Band Gap Fluorescence from Individual Single-Walled Carbon Nanotubes. *Science* **297**(5581): 593-596.

- Odom, T. W., J. L. Huang, P. Kim and C. M. Lieber (1998). Atomic structure and electronic properties of single-walled carbon nanotubes. *Nature* **391**(6662): 62-64.
- Orbach, E. and A. Finkelstein (1980). The Non-Electrolyte Permeability of Planar Lipid Bilayer-Membranes. *Journal of General Physiology* **75**(4): 427-436.
- Orth, R. N., J. Kameoka, W. R. Zipfel, B. Ilic, W. W. Webb, T. G. Clark and H. G. Craighead (2003). Creating biological membranes on the micron scale: Forming patterned lipid bilayers using a polymer lift-off technique. *Biophysical Journal* **85**(5): 3066-3073.
- Ouyang, M., J. L. Huang, C. L. Cheung and C. M. Lieber (2001). Energy gaps in "metallic" single-walled carbon nanotubes. *Science* **292**(5517): 702-705.
- Ouyang, M., J. L. Huang and C. M. Lieber (2002). Scanning tunneling microscopy studies of the one-dimensional electronic properties of single-walled carbon nanotubes. *Annual Review of Physical Chemistry* **53**: 201-220.
- Park, J. Y., S. Rosenblatt, Y. Yaish, V. Sazonova, H. Ustunel, S. Braig, T. A. Arias, P. W. Brouwer and P. L. McEuen (2004). Electron-phonon scattering in metallic single-walled carbon nanotubes. *Nano Letters* **4**(3): 517-520.
- Parthasarathy, R. and J. T. Groves (2004). Optical techniques for imaging membrane topography. *Cell Biochemistry and Biophysics* **41**(3): 391-414.
- Parthasarathy, R., C. H. Yu and J. T. Groves (2006). Curvature-modulated phase separation in lipid bilayer membranes. *Langmuir* **22**(11): 5095-5099.
- Patolsky, F., B. P. Timko, G. H. Yu, Y. Fang, A. B. Greytak, G. F. Zheng and C. M. Lieber (2006). Detection, stimulation, and inhibition of neuronal signals with high-density nanowire transistor arrays. *Science* **313**(5790): 1100-1104.

- Pennington, G. and N. Goldsman (2003). Semiclassical transport and phonon scattering of electrons in semiconducting carbon nanotubes. *Physical Review B* **68**(4): 045426.
- Pennington, G., N. Goldsman, A. Akturk and A. E. Wickenden (2007). Deformation potential carrier-phonon scattering in semiconducting carbon nanotube transistors. *Applied Physics Letters* **90**(6): 062110.
- Perebeinos, V., J. Tersoff and P. Avouris (2005). Electron-Phonon Interaction and Transport in Semiconducting Carbon Nanotubes. *Physical Review Letters* **94**(8): 086802-4.
- Pesen, D. and J. H. Hoh (2005). Micromechanical architecture of the endothelial cell cortex. *Biophys. J.* **88**(1): 670-9.
- Purewal, M. S., B. H. Hong, A. Ravi, B. Chandra, J. Hone and P. Kim (2007). Scaling of Resistance and Electron Mean Free Path of Single-Walled Carbon Nanotubes. *Physical Review Letters* **98**(18): 186808-4.
- Qin, L.-C., X. Zhao, K. Hirahara, Y. Miyamoto, Y. Ando and S. Iijima (2000). Materials science: The smallest carbon nanotube. *Nature* **408**(6808): 50-50.
- Quinn, B. M., C. Dekker and S. G. Lemay (2005). Electrodeposition of Noble Metal Nanoparticles on Carbon Nanotubes. *J. Am. Chem. Soc.* **127**(17): 6146-6147.
- Randall, L. (2007). The Case for Extra Dimensions. *Physics Today* **60**(7): 80-81.
- Richard, C., F. Balavoine, P. Schultz, T. W. Ebbesen and C. Mioskowski (2003). Supramolecular self-assembly of lipid derivatives on carbon nanotubes. *Science* **300**(5620): 775-778.
- Rosenblatt, S., H. Lin, V. Sazonova, S. Tiwari and P. McEuen (2005). Mixing at 50 GHz using a single-walled carbon nanotube. *Applied Physics Letters* **87**: 153111.

- Rosenblatt, S., Y. Yaish, J. Park, J. Gore, V. Sazonova and P. L. McEuen (2002). High performance electrolyte gated carbon nanotube transistors. *Nano Letters* **2**(8): 869-872.
- Roux, A., D. Cuvelier, P. Nassoy, J. Prost, P. Bassereau and B. Goud (2005). Role of curvature and phase transition in lipid sorting and fission of membrane tubules. *Embo Journal* **24**(8): 1537-1545.
- Sackmann, E. (1996). Supported membranes: Scientific and practical applications. *Science* **271**(5245): 43-48.
- Saiki, R. K., S. Scharf, F. Faloona, K. B. Mullis, G. T. Horn, H. A. Erlich and N. Arnheim (1985). Enzymatic Amplification of Beta-Globin Genomic Sequences and Restriction Site Analysis for Diagnosis of Sickle-Cell Anemia. *Science* **230**(4732): 1350-1354.
- Saito, R., G. Dresselhaus and M. S. Dresselhaus (1998). *Physical properties of Carbon Nanotubes*, Imperial College Press.
- Saito, R., M. Fujita, G. Dresselhaus and M. S. Dresselhaus (1992). Electronic-Structure of Chiral Graphene Tubules. *Applied Physics Letters* **60**(18): 2204-2206.
- Salafsky, J., J. T. Groves and S. G. Boxer (1996). Architecture and function of membrane proteins in planar supported bilayers: A study with photosynthetic reaction centers. *Biochemistry* **35**(47): 14773-14781.
- Saparov, S. M. and P. Pohl (2004). Beyond the diffusion limit: Water flow through the empty bacterial potassium channel. *Proceedings of the National Academy of Sciences of the United States of America* **101**(14): 4805-4809.

- Sazonova, V., Y. Yaish, H. Ustunel, D. Roundy, T. A. Arias and P. L. McEuen (2004). A tunable carbon nanotube electromechanical oscillator. *Nature* **431**(7006): 284-287.
- Shim, M., A. Javey, N. W. S. Kam and H. J. Dai (2001). Polymer functionalization for air-stable n-type carbon nanotube field-effect transistors. *Journal of the American Chemical Society* **123**(46): 11512-11513.
- Sotiropoulou, S. and N. A. Chaniotakis (2003). Carbon nanotube array-based biosensor. *Analytical and Bioanalytical Chemistry* **375**(1): 103-105.
- Star, A., J. C. P. Gabriel, K. Bradley and G. Gruner (2003). Electronic Detection of Specific Protein Binding Using Nanotube FET Devices. *Nano Lett.* **3**(4): 459-463.
- Star, A., E. Tu, J. Niemann, J.-C. P. Gabriel, C. S. Joiner and C. Valcke (2006). Label-free detection of DNA hybridization using carbon nanotube network field-effect transistors. *PNAS* **103**(4): 921-926.
- Stewart, D. A. and F. Leonard (2004). Photocurrents in Nanotube Junctions. *Physical Review Letters* **93**(10): 107401-4.
- Stryer, L. (1978). Fluorescence energy transfer as a spectroscopic ruler. *Annu. Rev. Biochem.* **47**: 819-46.
- Suzuura, H. and T. Ando (2002). Phonons and electron-phonon scattering in carbon nanotubes. *Physical Review B* **65**(23): 235412.
- Tang, X., S. Bansaruntip, N. Nakayama, E. Yenilmez, Y. I. Chang and Q. Wang (2006). Carbon Nanotube DNA Sensor and Sensing Mechanism. *Nano Lett.* **6**(8): 1632-1636.
- Tank, D. W., E. S. Wu and W. W. Webb (1982). Enhanced molecular diffusibility in muscle membrane blebs: release of lateral constraints. *J. Cell. Biol.* **92**(1): 207-12.

- Tans, S. J., A. R. M. Verschueren and C. Dekker (1998). Room-temperature transistor based on a single carbon nanotube. *Nature* **393**(6680): 49-52.
- Treacy, M. M. J., T. W. Ebbesen and J. M. Gibson (1996). Exceptionally high Young's modulus observed for individual carbon nanotubes. *Nature* **381**(6584): 678-680.
- van Meer, G. (2005). Membrane curvature sorts lipids - Stabilized lipid rafts in membrane transport. *Embo Reports* **6**(5): 418-419.
- Vijayaraghavan, A., S. Blatt, D. Weissenberger, M. Oron-Carl, F. Hennrich, D. Gerthsen, H. Hahn and R. Krupke (2007). Ultra-Large-Scale Directed Assembly of Single-Walled Carbon Nanotube Devices. *Nano Lett.*
- Wallace, P. R. (1947). The Band Theory of Graphite. *Physical Review* **71**(9): 622-634.
- Wang, F., G. Dukovic, L. E. Brus and T. F. Heinz (2005). The Optical Resonances in Carbon Nanotubes Arise from Excitons. *Science* **308**(5723): 838-841.
- Webb, W. W. (2001). Fluorescence correlation spectroscopy: inception, biophysical experimentations, and prospectus. *Applied Optics* **40**(24): 3969-3983.
- Wildoer, J. W. G., L. C. Venema, A. G. Rinzler, R. E. Smalley and C. Dekker (1998). Electronic structure of atomically resolved carbon nanotubes. *Nature* **391**(6662): 59-62.
- Wong, S. S., J. D. Harper, P. T. Lansbury and C. M. Lieber (1998). Carbon nanotube tips: High-resolution probes for imaging biological systems. *Journal of the American Chemical Society* **120**(3): 603-604.
- Wong, S. S., E. Joselevich, A. T. Woolley, C. L. Cheung and C. M. Lieber (1998). Covalently functionalized nanotubes as nanometre-sized probes in chemistry and biology. *Nature* **394**(6688): 52-55.

- Woodside, M. T. and P. L. McEuen (2002). Scanned probe imaging of single-electron charge states in nanotube quantum dots. *Science* **296**(5570): 1098-1101.
- Yaish, Y., J. Y. Park, S. Rosenblatt, V. Sazonova, M. Brink and P. L. McEuen (2004). Electrical nanoprobng of semiconducting carbon nanotubes using an atomic force microscope. *Physical Review Letters* **92**(4): 046401-(1-4).
- Yakobson, B. I. (1998). Mechanical relaxation and "intramolecular plasticity" in carbon nanotubes. *Applied Physics Letters* **72**(8): 918-920.
- Ye, J. S., H. F. Cui, Y. Wen, W. D. Zhang, A. Ottova, H. T. Tien, G. Q. Xu and F. S. Sheu (2005). Self-assembly of bilayer lipid membrane at multiwalled carbon nanotubes towards the development of photo-switched functional device. *Electrochemistry Communications* **7**(1): 81-86.
- Yu, M. F., O. Lourie, M. J. Dyer, K. Moloni, T. F. Kelly and R. S. Ruoff (2000). Strength and breaking mechanism of multiwalled carbon nanotubes under tensile load. *Science* **287**(5453): 637-640.
- Zhang, Y. J., J. R. Petta, S. Ambily, Y. L. Shen, D. C. Ralph and G. G. Malliaras (2003). 30 nm channel length pentacene transistors. *Advanced Materials* **15**(19): 1632-+.
- Zhen, Y., L. K. Charles and D. Cees (2000). High-Field Electrical Transport in Single-Wall Carbon Nanotubes. *Physical Review Letters* **84**(13): 2941-2944.
- Zheng, L. F., S. D. Li, J. P. Brody and P. J. Burke (2004). Manipulating nanoparticles in solution with electrically contacted nanotubes using dielectrophoresis. *Langmuir* **20**(20): 8612-8619.
- Zheng, L. X., M. J. O'Connell, S. K. Doorn, X. Z. Liao, Y. H. Zhao, E. A. Akhador, M. A. Hoffbauer, B. J. Roop, Q. X. Jia, R. C. Dye, D. E. Peterson, S. M. Huang, J. Liu

and Y. T. Zhu (2004). Ultralong single-wall carbon nanotubes. *Nature Materials* **3**(10): 673-676.

Zheng, M., A. Jagota, M. S. Strano, A. P. Santos, P. Barone, S. G. Chou, B. A. Diner, M. S. Dresselhaus, R. S. McLean, G. B. Onoa, G. G. Samsonidze, E. D. Semke, M. Usrey and D. J. Walls (2003). Structure-Based Carbon Nanotube Sorting by Sequence-Dependent DNA Assembly. *Science* **302**(5650): 1545-1548.

Zhou, X., J.-Y. Park, S. Huang, J. Liu and P. L. McEuen (2005). Band Structure, Phonon Scattering, and the Performance Limit of Single-Walled Carbon Nanotube Transistors. *Physical Review Letters* **95**(14): 146805-4.

Zhou, X. J., J. M. Moran-Mirabal, H. G. Craighead and P. L. McEuen (2007). Supported lipid bilayer/carbon nanotube hybrids. *Nature Nanotechnology* **2**(3): 185-190.